

PREFACE

This annual report reviews the research activities of the Laboratory of Advanced Science and Technology for Industry (LASTI) in the academic year of 2013 (April 2013 –March 2014) including activities using a 1.5GeV synchrotron radiation facility “NewSUBARU” and compact 15-MeV linac "LEENA" at the site of SPring-8. Other research activities of the micro and nanoscale carried out energetically at CAST building.

Topics of the NewSUBARU research activities of this year are as follows.

(1) Five beamlines were upgraded for advanced research and industrial application. Upgraded beamlines are BL05, BL07A & B, BL09, BL10 and BL11. For example, there have been improvements in the beamline control system and an upgrade of spectrometer in the industrial analysis beamline BL05. A large EUV mirror reflectivity meter was installed on BL10. One of the LIGA beamlines, BL11, was remodeled for advanced industrial manufacturing.

(2) A micro coherent scatterometry system was developed for phase defect inspection of the EUVL masks. A microprocessing using laser produced plasma was demonstrated. Nano-micro group developed a dihedral corner reflector array for floating image system.

All NewSUBARU beamlines are open for industry use. Promotion of both use and technical assistances industrial users is supported by MEXT's "Project for Creation of Research Platforms and Sharing of Advanced Research Infrastructure. "



Shuji Miyamoto

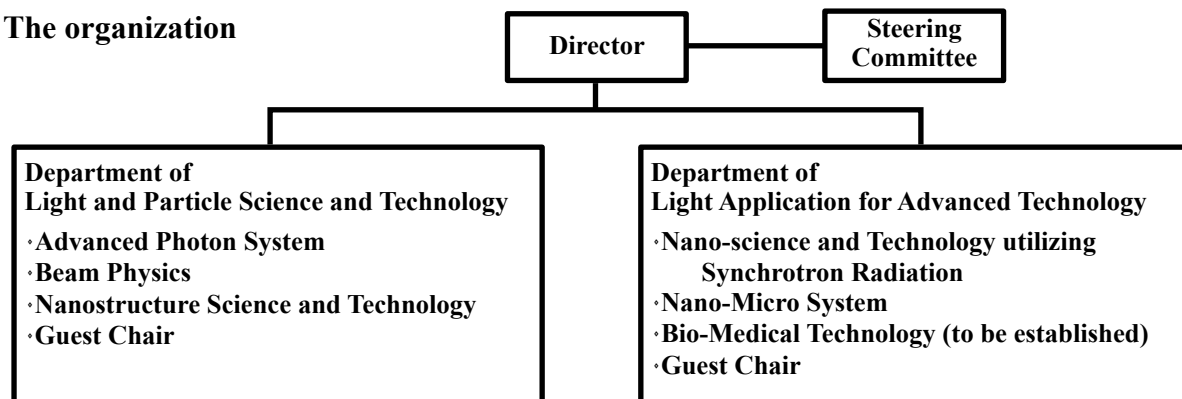
Director of LASTI
University of Hyogo

CONTENTS

PREFACE	i
CONTENTS	iii
ORGANIZATION	iv
CURRENT STATUS OF NewSUBARU	
<i>NewSUBARU Storage Ring</i>	1
<i>Beamlines</i>	3
<i>Construction of multilayered-mirror monochromator at BL07A</i>	10
<i>Construction of X-ray fluorescence spectrometer in the Ultra-soft X-ray region</i>	12
<i>BL05 Operating Status</i>	15
<i>Recent upgrade of 15MeV Electron Linear Accelerator LEENA for THz Radiation Sources</i>	16
RESEARCH ACTIVITIES	
<i>Investigation of Spectral recovery of Etching Damage Observed in XAS spectra of TiO₂ Thin Films</i>	19
<i>Oxidation State Analysis Soft X-ray Absorption Fine Structure Using M_{4,5} edge of Tin</i>	21
<i>Surface analysis of GaN treated by Ar ion beam etching</i>	23
<i>NEXAFS Study on Soft X-ray Irradiation Effect on Highly Hydrogenated Diamond-like Carbon Films</i>	26
<i>Atomic Oxygen beam irradiation Effect on the Si-doped DLC Films</i>	28
<i>Molecular Orientation at the Near-surface of Photolithography Films Determined by NEXAFS</i>	30
<i>EUV Resist Chemical Reaction Analysis using SR</i>	32
<i>Phase defect characterization on an extreme-ultraviolet blank mask using micro coherent extreme-ultraviolet scatterometry microscope</i>	39
<i>Low-Temperature Activation of Boron in B₁₀H₁₄-doped Si wafer by Soft X-ray Irradiation</i>	45
<i>Two Modified Layers in the surface of Silica-Based Films by Undulator Radiation</i>	47
<i>Microprocessing using Soft X-ray from Laser Produced Xe Plasma</i>	49
<i>Broadband spectroscopy of magnetic response in a nano-scale magnetic wire</i>	51
<i>Dihedral Corner Reflector Array for floating image manufactured by Synchrotron radiation</i>	56
<i>Evaluation of localized friction for antisticking layer by atomic force microscopy</i>	58
LIST OF PUBLICATIONS	
<i>Papers</i>	61
<i>International Meetings</i>	66
ACADEMIC DEGREES	81
COVER PHOTOGRAPHS	83
EDITORIAL BOARD	84

The Organization of Laboratory of Advanced Science and Technology for Industry University of Hyogo

The organization



Staff (FY 2011)

Research and faculty staff

MIYAMOTO Shuji, Professor, Director
 KINOSHITA Hiroo, Professor
 MATSUI Shinji, Professor
 KANDA Kazuhiro, Professor
 UTSUMI Yuichi, Professor
 NIIBE Masahito, Associate Professor
 SHOJI Yoshihiko, Associate Professor
 WATANABE Takeo, Associate Professor
 HARUYAMA Yuichi, Associate Professor
 YAMAGUTI Akinobu, Associate Professor
 AMANO Sho, Research Associate
 HASHIMOTO Satoshi, Research Associate
 HARADA Tetsuo, Research Associate
 OKADA Makoto, Research Associate

Specially appointed staff

MOCHIZUKI Takayasu, Professor

Guest staff

OHOKUMA Haruo, Professor
 ASANO Yoshihiro, Professor
 TAKAHASHI Yukio, Associate Professor
 NAGATA Yutaka, Associate Professor

Administrative staff

MATSUMOTO Shigeaki, General Manager
 KOGA Hitomi, Manager
 SONOHARA Kazuhiko, Chief
 KAMIYA Miki, CAST
 MAEDA Kaori, CAST
 YAMAMOTO Keiko, CAST
 YOKOYAMA Yuka, CAST
 FUJIMAKI Hisae, CAST
 KANATANI Naoko, NewSUBARU
 YAMADA Miki, CAST
 YAMAMOTO Mako, NewSUBARU
 KUSUMOTO Kumi, CAST
 MORIGUCHI Miyuki, Harima Forum of
 Science and Technology for 21st Century

Sharing of Advanced Research Infrastructure staff

ANDO Ainosuke, NewSUBARU
 FUKADA Noboru, NewSUBARU
 UMESAKI Masanori, NewSUBARU
 ISHIKAWA Kazuko, NewSUBARU
 INOUE Tomoaki, NewSUBARU
 KODAKA Takuya, NewSUBARU
 SHIMODA Mayu, NewSUBARU

Contact address

CAST (Center of Advanced Science and Technology, Hyogo)

3-1-2 Kouto, Kamigori-cho, Ako-gun, Hyogo, 678-1205 JAPAN.
 T:+81-791-58-0249 F:+81-791-58-0242

NewSUBARU Synchrotron Radiation Facility

1-1-2 Kouto, Kamigori-cho, Ako-gun, Hyogo, 678-1205 JAPAN.
 T:+81-791-58-2503 F:+81-791-58-2504

Web URL <http://www.lasti.u-hyogo.ac.jp/>, <http://www.lasti.u-hyogo.ac.jp/NS/>

e-Mail lasti@lasti.u-hyogo.ac.jp

Access <http://www.lasti.u-hyogo.ac.jp/NS-en/access/>

Current Status of NewSUBARU

NewSUBARU Storage Ring

Y. Shoji

Storage Ring Parameters

The machine parameters of the 1.5 GeV storage ring are listed in Table I. Although the machine condition remains the same, some of the values are revised according to the new model calculation.

Table I Main parameters of the NewSUBARU storage ring in FY2013.

Circumference	118.73 m
Bending lattice type	modified DBA
Number of bending cells	6
Straight sections	4m X 4, 15m X 2
Bending radius	3.22 m
Injection energy	1.0 GeV
Maximum energy	1.5 GeV
RF frequency	499.955 MHz
Betatron tune	6.29 (H), 2.23 (V)
<u>Momentum compaction factor</u>	<u>0.0014</u>
<u>Electron energy</u>	<u>1.0 GeV 1.5 GeV</u>
RF voltage	100 kV 260 kV
Natural energy spread	0.047% 0.072 %
Natural emittance	50 nm 112 nm
<u>Maximum beam current</u>	<u>500 mA</u>

Operation Status

The ring has two user-time operation modes, 1.0 GeV top-up operation mode and 1.5 GeV operation mode. The basic operation time is 9:00 - 21:00 of weekdays. Monday is used for machine R&D, Tuesday is for 1.5 GeV user time, Wednesday and Thursday are for 1.0 GeV top-up user time, Friday is for 1.0 GeV or 1.5 GeV user time. Night period or weekend is used for machine study and user time with the special mode, single bunch operation and Laser-Compton Gamma ray, if necessary.

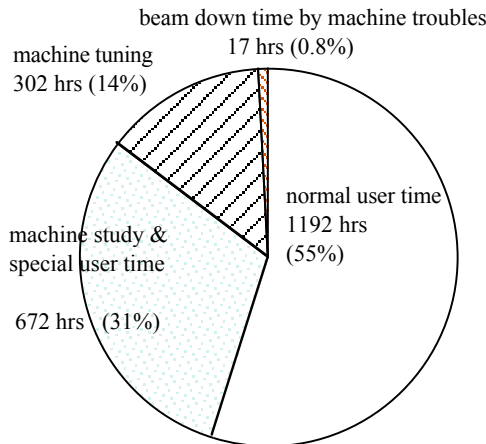


Figure 1: Machine time in FY2013.

The total machine time in FY2013 was 2183 hrs, 82% of that of FY2012, including the beam down time. Fig. 1 shows the breakdown. The beam down time includes not only the down by a failure, but also off-beam periods by a beam abort or others due to the beam instability. The reduced machine time from the previous FY was category 'beam line commissioning', which had been 659 hrs in FY 2012. The total of the normal user time and the beam line commissioning in this FY, 1192 hrs, was a 100% of that in FY2012. Time for machine study and special users was 123% of that in FY2012. The down time due to the machine trouble was 0.8%, 2/3 of that in FY 2012.

Machine Troubles

The machine troubles in FY2013 are listed in Table II. The rate of hardware troubles were increasing because they get older.

Machine Study and Special User Time

Table III shows the list of machine studies in FY 2013. Most of the study reports are open to the public on the home page of NewSUBARU (http://www.lasti.u-hyogo.ac.jp/beam_physics/NewSUBARU).

Accelerator Improvements

The top-up operation current had been raised from 250 mA to 300 mA since October 2012. Fig.2 shows typical operation in these 5 years. That condition was kept during FY2013, even at a worst case when the Compton-gamma line was in operation.

The synchrotron oscillation feed-back system was installed to reduced the coherent synchrotron oscillation. It improved the measurement accuracy of machine parameters at a special operation, such as a non-achromatic mode. The longitudinal oscillation spectrum with the feed-back on and off are shown in Figure 1.

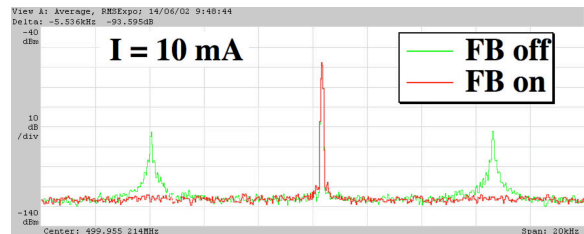


Figure 1: Measured time spectrum of the beam structure with and without feedback of synchrotron oscillation. The center line was the rf frequency and the broad side bands were synchrotron oscillation.

The injection timing system of the linac was improved. It effectively eliminated the dead time for changing the transportation line, to NewSUBARU or to the booster synchrotron. It reduced the time for

the beam accumulation of 300 mA from 35 min to 25 min (typical value). It also improved the atability of the top-up current from ± 0.5 mA to ± 0.3 mA.

Table II Machine troubles in FY2013.

Group	Failure/trouble	beam down time (hr)
Operation	Miss operation (human error)	2.7
	Beam loss by a beam instabilities	2.1
	Short Lifetime	3.9
Control	Program hung-up	1.0
	COD control failure	0.1
RF & Timing	Timing module	0
	Coupler failure	1.0
	Circulator arc	0.1
Magnet	Cooling water leak at Power supply	3.2
	Magnet IL failure	2.8

Table III List of machine studies in FY2013. The unit of study time is counted by shifts (typically 12 hrs).

R&D theme and special user mode	responsible person	study shift
Laser-Compton backscattering γ -rays	S. Miyamoto	17
Commissioning of visible light profile monitor port SR5	Y. Shoji	3
Optimization of vertical beam size for 1.5 GeV user time	K. Kanda	1
Betatron amplitude dependent orbit shift	Y. Shoji	1
Coherent synchrotron radiation by chromaticity modulation	Y. Shoji	15
Commissioning of the multi-element corrector	Y. Shoji	5

Beamlines

Takeo Watanabe and Hiroo Kinoshita
LASTI, University of Hyogo

Total nine beamlines are operating in the NewSUBARU synchrotron facility. Four beamlines of BL01, BL03, BL06 and BL11 were constructed until 1999. Three beamlines of BL07, BL09 and BL10 were started the operation from 2000.

BL03B beamline branched from the BL03 beamline propose for the usage of the EUVL (extreme ultraviolet lithography) microscope for the EUVL finished mask inspection.

BL09B beamline branched from BL09 beamline for the usage of the usage of the EUV interference lithography to evaluate. And BL09C beamline branched from BL09B

beamline for the usage of the thickness measurement of the carbon contamination originated to the resist outgassing during the EUV exposure.

BL02 beamline was constructed for the usage of LIGA in 2003.

BL05 beamline was constructed in response to a demand in the industrial world in 2008, which is the enhancement of the analysis ability in the soft X-ray region with the development of nanotechnology.

The arrangement of the beamlines in the NewSUBARU synchrotron radiation facility is shown in Fig.1.

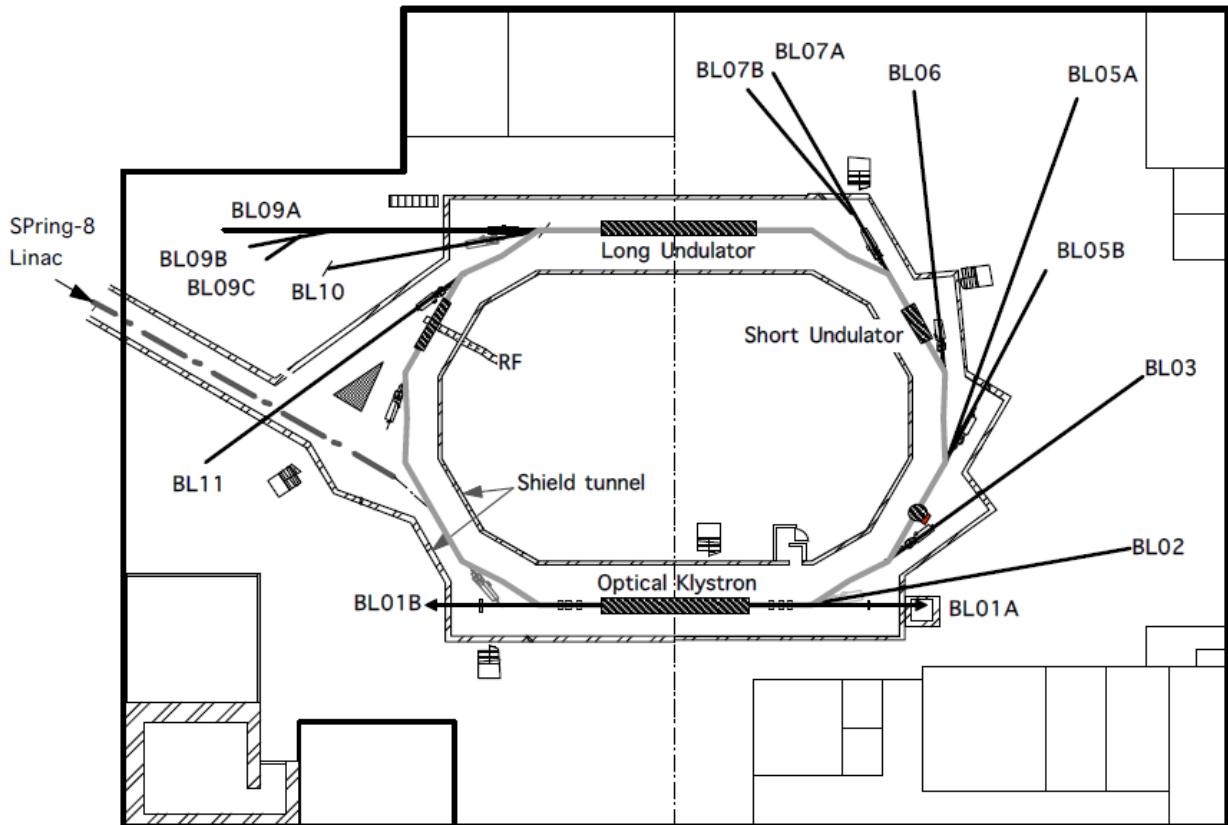


Fig. 1 Beamline arrangement in NewSUBARU.

I. BL01

BL01 is a beamline for research and developing new light sources. This beamline is one of two long straight section on NewSUBARU. Optical klystron was installed at this straight section. Upstream side of this beamline (BL01B) is intended to be used for visible and infrared light generated from free electron laser (FEL) or synchrotron radiation (SR). Downstream side of this beamline (BL01A) is used for laser Compton scattering gamma-rays source. Gamma-ray beamline hutch just outside of the storage ring tunnel was constructed in 2004 for gamma-ray irradiation experiments.

New gamma-ray irradiation hutch "GACKO" was installed at BL01A, collaborating with Konan University. Table 1. shows the specification of "GACKO".

Table 1. Specification of "GACKO"

Maximum gamma-ray power	0.33 mW
Maximum gamma-ray energy	1.7 MeV - 73 MeV
CO ₂ laser, wavelength/power	10.59 μm / 10W
1-1.7MeV gamma-ray flux	2×10^7 $\gamma/\text{sec}@10\text{W}/300\text{mA}$
Nd:YVO ₄ laser, wavelength/power	1.064 μm / 30W, 0.532 μm /20W
10-17 MeV gamma-ray flux	5×10^7 $\gamma/\text{sec}@30\text{W}/300\text{mA}$

II. BL02

The LIGA (abbreviated name of Lithographic, Galvanoformung and Abformung) process which consists from deep x-ray lithography, electroforming, and molding process is one of the promising candidates for such 3D microfabrication. More than hundreds aspect ratio for microstructure can be attained by the usage of the higher energy x-rays (4-15 keV) from synchrotron radiation (SR) with deeper penetration depth to the photosensitive resist. In this system we have succeeded to enlarge the exposure area up to A4 size and the fabrication dimension from submicron to millimeter by varying the energy of the x-ray source in accordance with the size of desired microparts. Microstructure with high aspect ratio over several hundred will be achieved using the x-rays over 10 keV since high energy x-ray has deep penetration depth to the photo-sensitive resist materials. Whereas, in the case of lithography for low energy x-rays from 1 keV to 2 keV, submicron structures with high aspect ratio will be achieved using the x-rays mask with precise line-width and thinner absorber, since low energy x-rays has low penetration depth. Based on this principle, the beamline for x-ray exposure have constructed with continuous selectivity of x-rays from 100 eV to 15 keV by using the

x-ray mirrors (plane and cylindrical mirror) and Be film filters. The horizontal angle of the outgoing SR could be obtained up to 12.5 mrad, which corresponds to the horizontal size of 220 mm (A4 horizontal size) at the exposure position. The second characteristic performance of the beamline is the high efficiency differential pumping system. This was necessary for maintain the vacuum difference between the storage ring ($<10^{-9}$ Pa) and the end-station ($<10^{-9}$ Pa) at which gasses for substrate cooling will be introduced in the exposure apparatus.

The flexibility for the shapes and functions of microstructure will be enlarged by achieving 3D microfabrication process using multi step exposure at various configuration between x-ray mask and substrates. The relative positions between x-ray mask and substrates, tilt and rotation angle to the SR incident direction can be moved simultaneously during SR exposure using 5 axis stages. The movement of each axis is controlled by the PC in terms of the scanning speeds, scanning length, and repetition number. In order to decrease the heat load of sample substrate suffered during SR irradiation helium introduction and substrate cooling mechanism were also equipped. Specification of spectrometer is listed in Table 2.

Table 2. Specification of the LIGA exposure system

Optics	Plane and cylindrical mirror, Be filters
Exposure energy	100 - 2 keV, and 4 - 15 keV
Exposure method	Proximity and multi-step exposure
Wafer size	A4 or 8 inch
Exposure area	230 mm(H) × 300 mm(V)
Exposure environment	< 1 atm (He-gas)

III. BL03

BL03 is a beamline for the developing the next generation lithographic technology so called extreme ultraviolet lithography (EUVL). The exposure tool is installed at the end station. Using this exposure tool, the research and development of the next generation lithography such as the less than 70 nm node is going on process. The exposure wavelength is 13.5 nm.

The semiconductor industry plays a very important role in the information technology (IT). In 2006, 256 Gbit DRAM with a gate length of 70 nm will be demanded in the IT industry. The extreme ultraviolet lithography (EUVL) is a promise technology for fabricating a fine

pattern less than 70 nm. To meet this schedule, this technology has to be developed in the pilot line until 2004. As for the practical use, it is very important that both to achieve large exposure area and to fabricate fine patterns. Therefore, at Himeji Institute of Technology, large exposure field EUV camera consists of three aspherical mirrors was developed. First in the world, we fabricated 60 nm line and space pattern in the large exposure area of 10 mm×10 mm on a wafer. Furthermore, BL03B beamline branches from the BL03 beamline propose for the usage of the EUVL microscope for the EUVL finished mask inspection. Table 3 shows the specification of ETS-1.

Table 3. Specification of the exposure tool (ETS-1)

Imaging optics	Three aspherical mirrors
Exposure wavelength	13.5 nm
Numerical aperture	0.1
Demagnification	1/5
Resolution	60 nm
Depth of focus	0.9 μm
Exposure area (static)	30 mm × 1 mm
Exposure area (scanning)	30 mm × 28 mm
Mask size	4 inch, 8 inch, and ULE 6025
Wafer size	8 inch
Exposure environment	In vacuum

IV. BL05

BL05 was constructed in response to a demand in the industrial world, which is enhancement of the analysis ability in the soft x-ray region with the development of nanotechnology. BL05 consists of two branch lines for use in the wide range from 50 eV to 4000 eV. BL05A and BL05B are designed to cover the energy range of 1300-4000 eV and 50-1300 eV, respectively. The incident beam from the bending magnet is provided for two branch lines through different windows of a mask. Therefore, these two branch lines can be employed simultaneously. At the end stations of each branch, the transfer vessel systems were mounted for the measurements of sample without

exposure to air. In addition, globe box was placed for the preparation of samples into transfer vessel.

1) The double crystal monochromator was installed at the BL05A. InSb, Ge, Si, SiO₂, Beryl and KTP crystals are prepared for a double-crystal monochromator. Toroidal mirrors are used as a pre-mirror and a focusing mirror of BL05A. XAFS measurement in the total electron yield mode and fluorescence XAFS measurement using SSD (SII Vortex) can be performed. The fluorescence XAFS spectra can be measured for samples at the end station filled with He gas. Table 4 shows the specification of monochromator.

Table 4. Monochromator specification

Monochromator	Double crystal monochromator
Monochromator crystals	SiO ₂ (1010) , InSb (111) , Ge (111) , Beryl (1010) , KTP (110) , Si (111)
Energy range	1300-4000 eV
Resolution	$E/\Delta E=3000$

2) The constant-deviation monochromator consisting of a demagnifying spherical mirror and a varied-line-spacing plane grating (VLSPG), which can provide high resolution, simple wavelength scanning with fixed slits, was mounted on BL05B. The optical system consists of a first mirror (M0), a second mirror (M1), an entrance slit (S1), a pre-mirror (M2), and three kinds of plane grating (G), an exit slit (S2) and a focusing mirror (M3). The including angle of the monochromator is 175°. Two measurement

chambers are prepared at the end station of BL05B. The XAFS spectra in the total electron yield mode and fluorescence XAFS spectra using SDD (Ourstex) can be measured in a high vacuum chamber. In addition, the photoelectron spectrum can be measured using spherical electron analyzer (VG Sienta, R3000) in an ultrahigh-vacuum chamber. The chambers can be replaced by each other within 1 hour. Table 5 shows the specification of the monochromator.

Table 5. Monochromator specification

Monochromator	Varied-line-spacing plane grating monochromator
Grating	100 l/mm, 300 l/mm, 800 mm/l
Energy range	50-1300 eV
Resolution	$E/\Delta E=3000$

V. BL06

BL06 has been mainly developed for irradiation experiments such as photochemical reaction, SR-CVD, photo-etching, surface modification. The white radiation beam from bending magnet is introduced to the sample stage using a pair of mirror, whose incident angle was 3°. The SR at BL06 sample stage had a continuous spectrum from IR to soft x-ray, which was lower than 1 keV. A

differential pumping system can be utilized for experiments in a gas atmosphere, which is difficult in the soft x-ray region. A sample holder can install four pieces of samples at a time. By using heater set in the sample holder, the sample can be heated from room temperature to 220°C. The temperature of sample is monitored using a Cr-Al thermocouple mounted on the sample holder.

VI. BL07A and BL07B

This beamline was designed for the development of new materials by SR technology. This beamline consists of two branch lines, which are provided with an incident beam from a 3-m-long undulator by switching the first mirror. One of them is a high photon-flux beamline with a multilayered-mirror monochromator for the study of SR-process (BL07A) and another is a high-resolution beamline with a varied line spacing grating monochromator for the evaluation of nano-structure characteristics by SR-spectroscopy (BL07B). The useful range of emitted photons from 50 to 800 eV is covered at both beamlines. The light source of BL07 is a 3-m length planar undulator, which consists of 29 sets of permanent magnets, a period length of which is 76 mm. The incident beam from the undulator is provided for two branch lines by translational switching of first mirror.

1) BL07A

The multilayered-mirror (MLM) monochromator, which has high reflectivity in the soft X-ray region, was

installed at the BL07A. It consists of a switching mirror chamber, a slit chamber, a MLM monochromator, a filter chamber and a reaction chamber. To obtain a large photon flux, we decided to use only first mirror (switching mirror), M0, for focusing. The MLM monochromator is designed to cover an energy range of up to about 800 eV by combination of three kinds of mirror pairs with 4 kinds of filter. The flux deliver by this design is estimated to be between a maximum of 10^{17} photons/s at 95 eV and a minimum 2×10^{14} photons/s at 300 eV for a 500 mA ring current. Table 6 shows the summary of BL07A. In addition, X-ray fluorescence (XRF) apparatus using spherical varied line spacing grating was mounted at the downstream of irradiation chamber. The poly capillary was used to enhance beam-condensing efficiency. Measurement energy range was from 30 eV to 450 eV. This XRF apparatus was expected to utilize the chemical analysis on the light metals, Li and Be, and light elements, B, C and N.

Table 6. Summary of BL07A.

Energy range (eV)	Multilayer mirror					Filter	
	Material	spacing	Thickness Ratio	number of layers	$\Delta E/E$	material	Thickness
50-60	Mo/Si	20 nm	0.8	20	6.2 %	Al	100 nm
60-95						None	—
90-140	Mo/B ₄ C	11 nm	0.5	25	3.3 %	Ag	100 nm
140-194						Cr	500 nm
190-400	Ni/C	5 nm	0.5	60	2.5 %	Ni	500 nm
400-560							
550-800							

2) BL07B

The constant-deviation monochromator consisting of a demagnifying spherical mirror and varied line spacing plane grating (VLSPG), which can provide to high resolution, simple wavelength scanning with fixed slits, was mounted on BL07B. The optical system consists of a first mirror (M0), an entrance slit (S1), a premirror (M1), and three kinds of plane grating (G), an exit slit (S2) and a focusing mirror (M2). The monochromator is designed to

cover the energy range 50-800 eV with three gratings, of which including angle are 168°. The VLSPG has been well known to obtain high resolution in extreme ultraviolet region by diminishing various kinds of aberration. The total resolving power about 3000 can be realized in the whole energy region. Table 7 shows the specification of the monochromator.

Table 7. Monochromator specification

Mount type	Hettrick-Underwood type
Grating G1, G2, G3	Plane VLS (600 l/mm, 1200 l/mm, 2400 l/mm)
Energy range	50-150 eV, 150 – 300 eV, 300-800 eV
Resolving power (E/ ΔE)	~3000

VII. BL9

A purpose of this beamline is studies on a soft x-ray interferometry or a holographic exposure experiment with making use of highly brilliant and coherent photon beams radiated from 11 m long undulator in NewSUBARU.

BL09 consists of M0 mirror, M1 mirror, G grating and M2 and M3 mirror. M0 and M3 mirrors are used for horizontal deflection and beam convergence, M1 is used for vertical beam convergence at the exit slit, and M2 is used for vertical deflection and beam convergence. A monochromator is constructed by M1 and a plane grating. The maximum acceptance of the undulator beam is 0.64 mrad in horizontal and 0.27 mrad in vertical. The acceptance can be restricted by 4-jaw slits equipped at upstream of the M0 mirror.

BL09A beamline is used for material analysis: X-ray

absorption spectroscopy (XAS) and X-ray photoelectron spectroscopy (XPS). In 2013, X-ray emission spectrometer (XAS) was introduced at the endstation of the BL09A. The energy range and resolution of the XAS was designed to be about 50-600 eV and 1500, respectively.

BL09B beamline branched from BL09 beamline for the usage of the EUV interference lithography for the evaluation of the exposure characteristics of EUV resist. Coherence length of 1 mm at the resist exposure position was achieved using BL09B beamline. And BL09C beamline branched from BL09B beamline for the usage of the thickness measurement of the carbon contamination originated to the resist outgassing during the EUV exposure. Table 8 shows the specification of the monochromator.

Table 8. Monochromator specification

Mount type	Monk-Gillieson type
Grating	Plane VLS (300, 900, 1200 l/mm)
Energy range	50 – 750 eV
Resolving power (E/ ΔE)	~3000

VIII. BL10

BL10 is for the global use in the Himeji Institute of Technology. M0 mirror is used for horizontal deflection and beam convergence, M1 is used for vertical beam convergence at the exit slit, and M2 is used for vertical deflection and beam convergence. A monochromator is constructed by M1 and a plane grating. At the beginning, the multilayers reflectivity measurement was carried out at this beamline. The characteristics of this beamline and the result of the Mo/Si multilayers measurement are carried out for the development of the EUV- mask technology.

BL10 utilizes a monochromator of the varied line spacing plane grating monochromator (VLS-PGM). The line density of the monochromator in central region of the gratings were 600, 1800 and 2,400 lines/mm. The reflectometer is a two axis vacuum goniometer using two Huber goniometers. One axis carries the sample, which may for example be a mirror at the center of the reflectometer vacuum tank (θ -motion). The other (ϕ -motion) carries the detector on a rotating arm. In

addition there are through-vacuum linear motions to translate the sample in two orthogonal directions (x,y). All motors are controlled by computer. The sample itself is mounted on a kinematic holder. The control stage monochromator rotation, and data analysis were program using LABVIEW software. The reflectivity result obtained at BL10 has a good agreement with that at LBNL. Table 9 shows the specification the monochromator.

The micro-CSM tool was adapted at the most downstream of the BL10 beamline for the EUV mask defect inspection. This too is very effective for the inspection of the actinic patterned mask.

A large reflectometer was installed in a branch line for large EUV optical component including EUV collector mirrors. The reflectometer has a sample stage with y, z, θ , ϕ , and Tilt axis, which can hold large optical elements with a maximum weight of 50 kg, a diameter of up to 800 mm, and a thickness of 250 mm. The entire sample surface is able to be measured.

Table 9. Monochromator specification

Mount type	Hettrick-Underwood type
Grating	Plane VLS (600, 1800, 2400 l/mm)
Energy range	50 – 1,000 eV
Resolving power ($E/\Delta E$)	~ 1000

IX. BL11

A beam line BL11 is constructed for exposure Hard X-ray Lithography (DXL) in the LIGA (German acronym for Lithographite Galvanoformung and Abformung) process. LIGA process, that utilizes a useful industrial application of SR, is one of the promising technologies for fabrication of extremely tall three-dimensional (3D) microstructures with a large aspect ratio. This process was invented at the Institut Fur Mikrostrukturtechnik (IMT) of the Karlsruhe Nuclear Center (KfK) in 1980. Microstructures with height of over a few hundreds μm have been widely applied to various fields such as micro-mechanics, micro-optics, sensor and actuator technology, chemical, medical and biological engineering, and so on. This beam line was designed by the criteria ; photon energy range from 2 keV to 8 keV, and a density of total irradiated photons $\geq 10^{11}$ photons/cm². The BL11 can provide the most suitable photon energy for microfabrication in X-ray lithography, while the BL2 is equipped for fabricating fine pattern submicron-scale

structure and microstructure with high aspect ratio by selectivity of X-rays using movable mirror system. That is, LIGA process in NewSUBARU can provide the best 3D microfabrication because the BL11 and BL2 are complementary. The beamline BL11 is consisting of an absorber chamber, a first-mirror chamber (M1), a 4-way slit chamber, a Be and polyimide window chamber, and an exposure chamber. The horizontal angle of the outgoing SR could be obtained up to 17.8 mrad, providing a beam spot size on the exposure stage $\geq 80 \times 10 \text{ mm}^2$. The micron-scale structure with high aspect ratio will be achieved using the toroidal typed mirror M1 which can produce a parallel collimated beam of X-rays. In addition, the homogeneity of the beam is excellently controlled by a novel adding system.

Using the precision stage in the exposure chamber, the flexibility for the shaped and functions of microstructure will be enlarged by achieving 3D microfabrication process using multi step exposure at various configuration

between x-ray mask and substrates. The exposure area of 200 mm × 200 mm is brought to fruition. In order to decrease the heat load of sample substrate suffered during

SR irradiation, helium introduction and substrate cooling system were also equipped. The specification of the LIGA exposure system is listed in Table 10.

Table 10. Specification of the LIGA exposure system

Exposure method	Proximity exposure
Wafer size	8 inch
Exposure area	200 mm(H) × 200 mm(V)
Exposure environment	< 1atm (He-gas)

Acknowledgement

We would like to thank all the staff who work at NewSUBARU synchrotron light facility for their help to describe the update details of the beamlines.

Construction of multilayered-mirror monochromator at BL07A

Shotaro TANAKA¹, Ryo IMAI¹, Kazuhiro KANDA¹, and Sei FUKUSHIMA²

¹*LASTI, University of Hyogo, 3-1-2 Koto, Kamigori, Ako, Hyogo 678-1205 Japan*

²*National Institute for Materials Science, 1-2-1 Sengen, Tsukuba-shi, Ibaraki, 305-0047, Japan*

Abstract

A new multilayered-mirror monochromator was constructed at a 3-m undulator beamline, BL07A. This monochromator was designed to cover an energy range from 80 eV to 800 eV using three kinds of multilayer mirror pairs. Using this monochromator, BL07A can be used as a high-photon flux and energy tunable beamline.

Introduction

A multilayered-mirror (MLM) monochromator designed especially for synchrotron radiation (SR) stimulated process experiments and a light source of X-ray fluorescence spectrometer has been constructed at BL07A. The light source of BL07 is a 3m length planar undulator. Undulator light has higher photon flux compared to light from a bending magnet but it is quasi-monochromatic, because several higher harmonic lights are generated corresponding to an undulator gap. A MLM monochromator can monochromatize incident soft X-rays with a high throughput and its resolving power, $E/\Delta E$, is lower than 10, but, it is sufficient to remove the higher harmonic lights from undulator light except the purpose light. As a result, BL07A can be utilized as a high-photon flux and energy tunable beamline by the combination of undulator with a MLM. By the elimination of unnecessary harmonic lights, BL07A can be used for the SR stimulated process experiments at low temperature, such as crystallization of amorphous silicon, modification of glass as an optical wave guide, and any other surface modification using soft X-rays. In addition, a high-flux photon beam monochromatized with a MLM monochromator can be useful as a light source of X-ray fluorescence spectrometer which is mounted downstream of irradiation chamber of BL07A.

Specification

The MLM monochromator constructed in the present study covers an energy range from 80 eV to 800 eV by combinations of mirror pairs with filter. Soft X-ray is absorbed at the material surface to have high energy, and reflectance is extremely low. The multilayered reflecting mirror stacks a light element and a heavy element in turn and can achieve high reflectance by the borrowed light from the border of the layer interfering it, and strengthening it. The reflectance is decided at the properties of matter of the multilayer film material, a layer thickness and depends on the incidence angle to use interference. Three kinds of mirror pairs are prepared for this MLM monochromator, Mo/Si, Mo/B₄C, and Ni/C, whose bilayer spacing, d , are 19.5, 11.2, and 5.1, respectively, and whose ratios of thickness of metal layer by d spacing, Γ , are 0.22, 0.53, and 0.51, respectively. Incident angle of this MLM monochromator can be varied from 4° to 65°. The filter is used to eliminate higher energy radiation included in reflected light from multilayered reflecting mirror. Three kinds of metal foil are prepared as a filter, Ag, Cr, and Ni, whose thickness are 100, 500, and 500 nm, respectively and their energy of absorption edge are 368 eV (Ag, M-shell), 574 eV (Cr, L-shell), and 852 eV (Ni, L-shell). As a result, the MLM monochromator constructed in the present study covers an energy range from 80 eV to 800 eV by combinations of three kinds of mirror pairs with three kinds of filter as summarized in Table 1.

Table 1 Summary of MLM monochromator

Energy range(eV)	Multilayer	Filter
80-140	①Mo/Si	None
125-140	②Mo/B ₄ C	None
140-200	①Mo/Si	Ag
140-360	②Mo/B ₄ C	Ag
260-400	③Ni/C	Ag
400-560	③Ni/C	Cr
560-800	③Ni/C	Ni

For the estimation of a photon flux, current detected with a photodiode (PD) was measured. During this experiment, the electron energy of the NewSUBARU ring was 1.5 GeV. Measured PD current was normalized by ring current at 300 mA, because the ring current decreased with time. Figures 1-5 depict normalized PD current at each harmonic light with a kind of filter. We can obtain photon flux from these data.

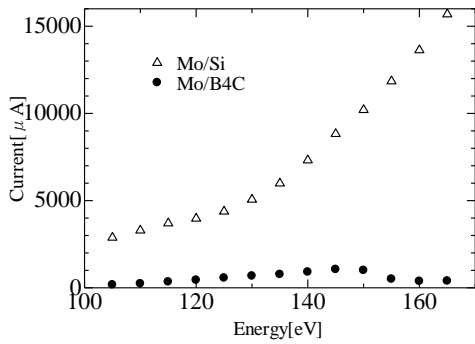


Fig. 1 PD current at 1st harmonic light without filter.

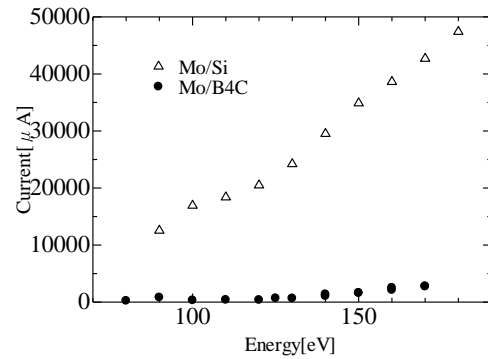


Fig. 2 PD current at 3rd harmonic light without filter.

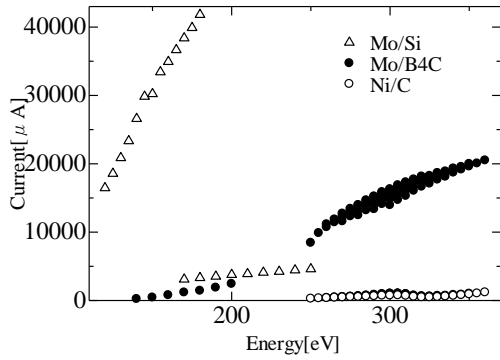


Fig. 3 PD current at 3rd harmonic light with a Ag filter.

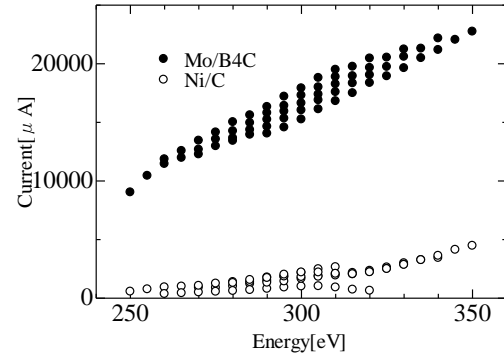


Fig. 4 PD current at 5th harmonic light with a Ag filter.

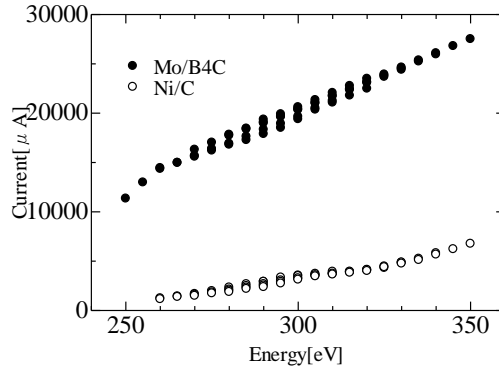


Fig. 5 PD current at 7th harmonic light with a Ag filter.

Construction of X-ray fluorescence spectrometer in the Ultra-soft X-ray region

H. Takamatsu¹, K. Kidena¹, K. Kanda¹, and S. FUKUSHIMA²

¹*LASTI, University of Hyogo, 3-1-2 Koto, Kamigori, Ako, Hyogo 678-1205 Japan*

²*National Institute for Materials Science, 1-2-1 Sengen, Tsukuba-shi, Ibaraki, 305-0047, Japan*

Abstract

We constructed a ultra-soft X-ray spectrometer, which can be measured in the range of ultra-soft X-rays of about 33-470 eV at the undulator line BL07A. The high-flux and high-resolution is performed by the use of two kinds of spherical varied-line spacing gratings, a poly-capillary, and a backside illumination type CCD camera. This spectrometer is expected to a high-resolution analysis of light-elements, light-metals, and transition metals.

Introduction

An X-ray fluorescence (XRF) spectrometer is used for routine, relatively non-destructive chemical analyses of industrial materials, biological materials, and environmental materials. The analysis of major and trace elements in samples by X-ray fluorescence is made possible by the behavior of atoms when they interact with radiation. When materials are excited with X-rays, they can become ionized. If the energy of the radiation is sufficient to dislodge a tightly-held inner electron, the atom becomes unstable and an outer electron replaces the missing inner electron. When this happens, energy is released due to the decreased binding energy of the inner electron orbital compared with an outer one. The emitted radiation is of lower energy than the primary incident X-rays and is termed fluorescent radiation. Because the energy of the emitted photon is characteristic of a transition between specific electron orbitals in a particular element, the resulting fluorescent X-rays can be used to detect the abundances of elements that are present in the sample.

For the measurement of XRF spectra, the use of SR presents especially the following advantages: 1) SR has high brilliance. 2) The excitation energy can be selected and adapted to the problem. 3) The radiation is linearly polarized. We constructed the SR-XRF setup at BL07A in the NewSUBARU facility. BL07A has a 3-m undulator as a light source and a high-photon flux and energy tunable light is supplied from a multilayered-mirror monochromator in the energy range from 50 eV to 800 eV. .

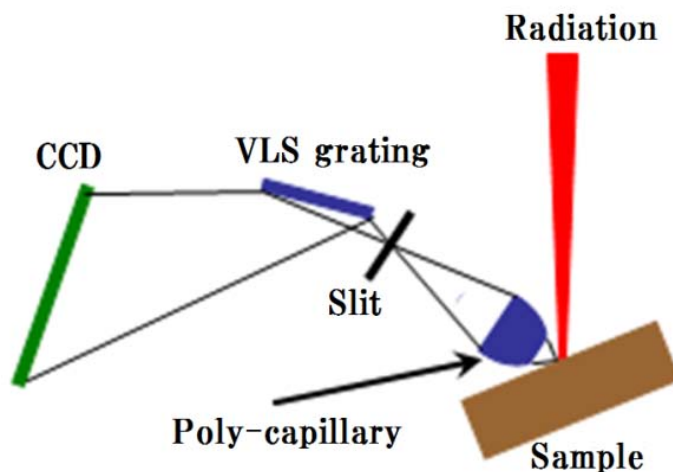
Specifications

Undulator light dispersed by a MLM monochromator was introduced to a Cr-coated planer mirror Cr mounted upstream XRF spectrometer to eliminate the high energy light higher than 500 eV, especially for oxygen, from the MLM monochromator. A schematic view of the XRF spectrometer is shown in Fig. 1. Reflected light at the plane mirror was incident to a sample. The fluorescent radiation in the ultra-soft X-ray

region was focused onto a slit using the poly-capillary, whose beam spot was ≈ 1 mm diameter. Dispersed ultra-soft X-rays by a grating were detected with a CCD camera. This spectrometer can measure the range of ultra-soft X-rays of about 33-470 eV.

This spectrometer has three characteristics. At first, two kinds of spherical VLS (varied line spacing) gratings designed with equal focal curves are used as the dispersion

Fig. 1 A schematic view of the ultra-soft X-ray fluorescence spectrometer



components. By using an appropriate grating properly by the energy range, XRF spectra can be obtained easier than a use of a single grating. The second feature is the use of a poly-capillary as the input component of the spectrometer. Using a poly-capillary, it is possible to increase the effective capturing angle of the ultra-soft X-rays, such that the ultra-soft X-rays can be efficiently converged and the detection efficiency increases. Moreover, the slit can be positioned on the poly-capillary's focus point to get the X-rays dispersed by gratings. The picture of the tip of the poly-capillary is shown in Fig. 2. The final feature is the use of backside illumination type CCD camera. This CCD camera has not a movable part and can detect the X-rays dispersed by the grating. The dispersion direction of the grating is set precisely to match the direction of the pixel lines on the projection plane. This setting made it possible to obtain the spectrum of ultra-soft X-rays because this measures the total signal strength of a pixel line perpendicular to the distributed direction. At the last, the specifications of the main components of the spectrometer are listed in Table 1.



Fig. 2 The photograph of the tip of a poly-capillary

Table 1. The specifications of the main components of the spectrometer

grating	flat field spherical varied line spacing type Radius of curvature: 6005 mm braze angle: $1.7 \pm 0.3^\circ$ the incidence angle: 87.19° the incidence focal length: 240 mm the injection focal length: 300 mm size: 52×32 mm grating 1 (33 eV–140 eV) the number of the central fissure line: 300 Lmm ⁻¹ grating 2 (106 eV–470 eV) the number of the central fissure line: 1090 Lmm ⁻¹
poly-capillary	collective solid angle: 0.072 Sr. input focal distance: 19.75 mm output focal distance: 215 mm
CCD camera	Roper SC-1300B (back side illuminated type) number of pixel: 1340×1300 pixel size: 20 μm×20 μm detection area size: 26.8 mm×26 mm
slit	1mmφ, 100 μm×2 mm, 50 μm×2 mm, 2 mmφ (full open)
vacuum system	magnetic-levitating turbo-molecular pump spectrometer chamber: $\sim 1 \times 10^{-5}$ Pa, sample chamber : $\sim 1 \times 10^{-7}$ Pa

BL05 Operating Status

T. Hasegawa¹, M. Uemura¹, N. Fukada¹, N. Umesaki² and K. Kanda²

¹ Synchrotron Analysis L.L.C., 3-2-24 Wadamiya-dori, Hyogo-ku, Kobe, Hyogo 652-0863 Japan
² LASTI, University of Hyogo, 3-1-2 Koto Kamigori, Ako, Hyogo 678-1205 Japan

Abstract

A material analysis beamline for the industrial enterprises' use was completed at BL05 in March 2008. This beamline is constructed on the basis of strong demand of industrial users for X-ray absorption fine structure (XAFS) spectroscopy. The used time of BL05 increased steadily every year. BL05 was broadly upgraded corresponding to the user's demands. This upgrading was expected to increase used time and to expand the industrial users.

Introduction

BL05 consists of two branch lines, one is a double crystal monochromator beamline (BL05A) for the use in the higher-energy region (1300-4000 eV) and the other is a varied line spacing plane grating (VLSPG) monochromator beamline (BL05B) for the use in the lower-energy region (50-1300 eV) [1]. These branches can be operated simultaneously. BL05 is managed and maintained by the Synchrotron Analysis L.L.C. (SALLC), which is composed of the industrial companies, in cooperation with the staffs of the Laboratory of Advanced Science and Technology for Industry in University of Hyogo.

1. BL05 Operating Status

The operation for public use of BL05 has started since 2008. In Fig.1, used time of BL05 is shown. The used time of BL05 increased every year. This beamline can be used as a trial use from 2010, which is supported from the ministry of education, cultur, sports, science and technology. Total used time, which included paid use and trial use, reached for 185 hours at total time of 2011, and broke through 200 hours in 2012. The used time of 2013 exceeded that of the previous year, although machine time of New SUBARU decreased due to the repair of SPring-8. The upgradings of BL05, installation of the calculation and combination type double crystal monochromator, systems of measurement in an in-situ environment, introduction systems for anaerobic sample, and the operation of beamline optics by remote control, were completed in 2014.

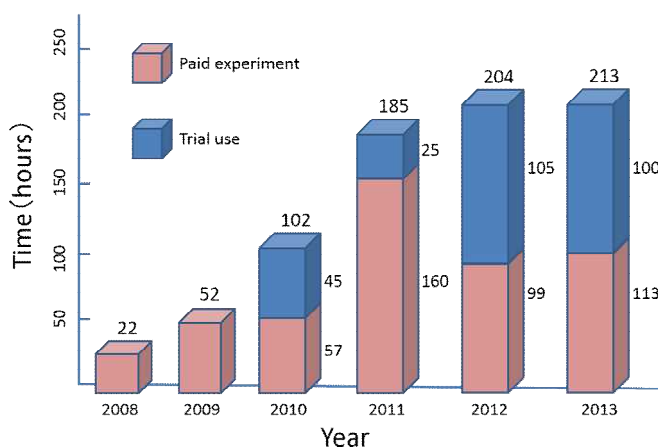


Fig.1. Transition of used time of BL05.

2. The training program for industrial researchers

For the purpose of enhancement the analytical skills using synchrotron radiation of industrial enterprises, we have opened the training program for industrial researchers from 2011 in cooperation with local public body etc (Fig.2). This program is covered not only lesson in the classroom, but hands-on practice of analysis using beamline. Some of the companies that participated in the program, used BL05 as a paid use.



Fig.2. Hands-on practice of analysis using synchrotron radiation.

Reference

[1] T.Hasegawa *et al.*, *Advances in X-ray Chem. Anal. Jpn.*, **41**, pp.99-106 (2010) [in Japanese].

Recent upgrade of 15MeV Electron Linear Accelerator LEENA for THz Radiation Sources

S. Hashimoto, K. Kobayashi, K. Kawata, Y. Minagawa[#], Y. Takemura[#], S. Amano and S. Miyamoto
 LASTI, University of Hyogo
[#]JASRI

Abstract

The 15MeV electron linear accelerator LEENA has been upgraded towards tunable and high-power tera-hertz (THz) light sources using relativistic electrons. Recently we installed a solenoid coil for electron beam focusing and an OTR monitor for beam profile measurement. And also we constructed a THz beam-line for user experiments.

Introduction

In the building of NewSUBARU synchrotron light facility, we are developing tunable and high-power THz radiation sources using relativistic electron beams from a 15 MeV compact linear accelerator LEENA [1]. Synchrotron radiation from a bending magnet and Smith-Purcell radiation from a metal grating have been successfully observed in THz regime. A general layout of LEENA is shown in Fig. 1. Main parameters of the accelerator are shown in Table 1. If the electron bunch length is shorter than the wavelength of radiated electromagnetic wave, the electron beam coherently emits high-power radiation. In the last year several components of LEENA have been upgraded; (1) the installation of a solenoid magnet for focusing electron beam radius just after an electron gun, (2) the installation of OTR monitor for measuring electron beam profile and (3) the construction of THz beam-line.

Table 1. Main parameters of LEENA accelerator.

Beam energy	6 – 15MeV
Macro pulse current	100mA
Macro pulse width	5 μ s
Repetition rate	1-10Hz
RF frequency	2856 MHz
Normalized emittance	< 10mm·mrad
Energy spread	< \pm 0.5%@15MeV
Electron gun	RF gun
Cathode	LaB6 (thermal)
THz radiation sources	Bend, Smith-Purcell
Radius Curvature (BM3)	0.2m

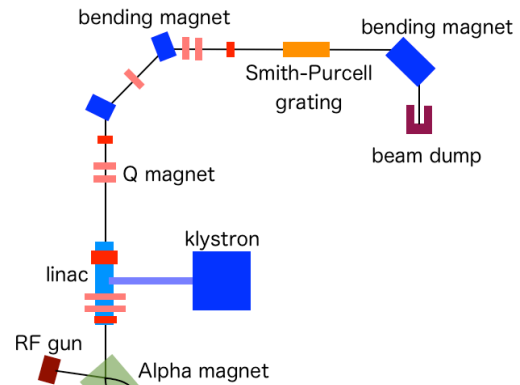


Fig.1 Layout of LEENA.

Solenoid magnet for electron beam focusing

One of problems on beam operation was the beam divergence at low energy region just after an electron gun. In order to correct the divergence of the beam radius, a new water-cooled solenoid coil of 22500 AmpereTurns as shown in Fig.2 is designed and installed at 10cm downstream of the RF electron gun. The maximum current of 300A generates magnetic field of 0.37T. Outside of the coil is covered with an iron plate of 5mm thickness to prevent the magnetic field from leaking. Figure 2 also shows the magnetic field calculated using POISSON code [2] with two-dimensional axial symmetry. It finds that field components on a cathode of the RF gun, which causes beam emittance growth, is very weak. With fine-tuning of the solenoid field, beam current loss became very small.

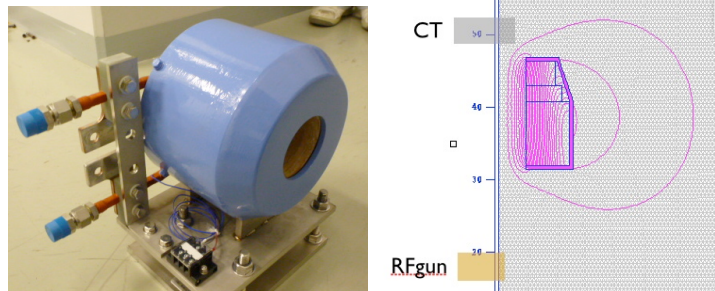


Fig.2 Solenoid coil (left) and 2D axial symmetric magnetic field calculated using POISSON code (right).

OTR monitor for measuring beam profile

When an electron passes through a surface of a thin metal film such as aluminum, the transition radiation is observed due to the difference of the dielectric constants of the vacuum and the metal. The transition radiation in the optical regime is commonly used as an electron beam monitor in linear accelerators (Fig. 3). Changing focal length of CCD camera lens, both the spot size and the divergence angle of an electron beam pulse can be measured.

The installed film is aluminum of thickness 12 μm . An IEEE1394 camera observes the OTR of 5 μs time duration in synchronization with the electron beam. The acquired CCD image data is transferred to a PC and the application software developed by LabVIEW performs the real-time image processing and beam parameters can be evaluated as shown in Fig. 4.

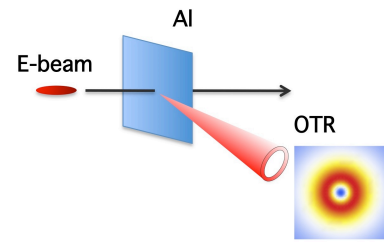


Fig.3 Optical Transition Radiation (OTR).

Beam size measured using the OTR monitor is 0.8 mm in horizontal and 0.24 mm in vertical. And the measured beam divergence is 52 mrad in horizontal and 150 mrad in vertical. Thus the measured normalized emittances of 13.2π mm-mrad in horizontal and 11.5π mm-mrad in vertical are well corresponding to the designed value of 10π mm-mrad. The OTR monitor is useful tool for the optimization of beam parameters towards the THz light source.

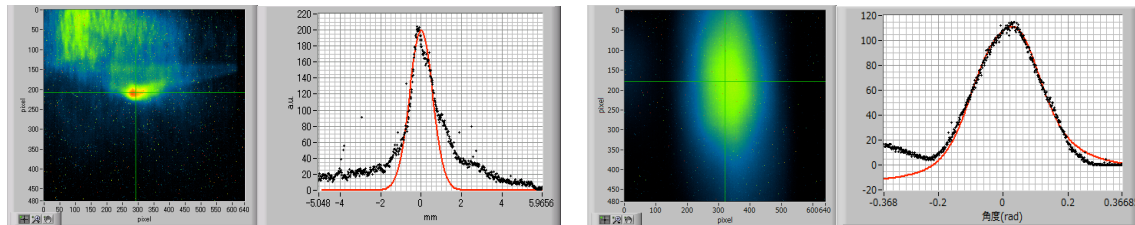


Fig.4 Observation of Optical Transition Radiation (OTR). Beam spot image and data fitting in vertical direction (left). Beam divergence and data fitting in vertical direction (right).

THz beam-line for user experiments

THz radiation was previously measured inside the concrete tunnel for the radiation protection. It was inconvenient to stop the machine every time we enter the tunnel for measurement setup.

In the newly constructed beam-line, THz radiation from the bending magnet is focused and transmitted using two curved-mirrors through a penetration hole in the concrete wall to the next experimental room, where an optical table is equipped for user experiment.

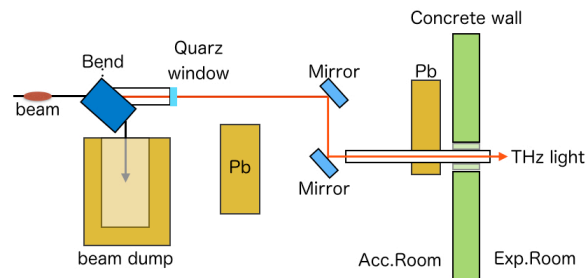


Fig.5 THz beam-line.

Recent operation status and future plans

The beam operation of LEENA has been stopped since January 2014 because of the failure of a high-voltage power supply for the RF klystron. The beam operations towards the generation of the coherent THz radiation by the short-bunched electron beams would be resumed after completion of the repair.

References

- [1] S.Hashimoto *et al.*, IEEJ Transactions on Electronics, Information and Systems, **vol.134** No.4 pp.495-501 (2014)
- [2] K. Halbach and R. F. Holsinger, Particle Accelerators 7, pp.213-222 (1976)

Research Activities

Investigation of Spectral Recovery of Etching Damage Observed in XAS spectra of TiO₂ Thin Films

Keiji Sano¹, Masahito Niibe¹, Retsuo Kawakami², Yoshitaka Nakano³
(Univ. Hyogo¹, Univ. Tokushima², Chubu Univ.³)

Abstract

We analyzed TiO₂ thin films etched with capacitively coupled plasma etching apparatus by near edge X-ray absorption fine structure (NEXAFS) method. As a result, spectral change due to disordering of the crystalline structure was observed by TFY method (including visible light) in the sample treated with higher gas pressure. We also found that disordered Ti-L_{2,3} spectra of etched sample recovered to as-grown-like by irradiation with soft X-rays. Furthermore, the spectra of recovered samples were returned to disordered shape by exposing the sample to air or keeping in vacuum for a long time. On the other hand, the spectra that measured by TFY method excluding visible light emission was not changed due to the etching and the soft X-ray irradiation.

Introduction

TiO₂ is known not only photocatalytic material but also high dielectric constant material. Therefore, TiO₂ is expected to apply as MOS gate oxide film because of its high dielectric constant. To use TiO₂ as MOS gate film, it has to be processed by etching. However, there are a few reports about the effect of etching damage to TiO₂ thin films by etching process. Therefore, we analyzed the effect of etching damage to TiO₂ samples by NEXAFS method. We have found the phenomenon during the analyzing process that disordered NEXAFS spectra of the etched film recovered to as-grown-like by irradiation with soft X-rays^{[1],[2]}.

The purpose of this study is the elucidation of the phenomenon that NEXAFS spectra of etched TiO₂ thin film recovered by soft X-ray irradiation. We investigated the spectral recovery condition of the etching damage. For example, recovery of the spectra was studied for irradiation condition, and compared between the presence and absence of visible light emission.

Experiments

TiO₂ thin films (anatase) were deposited on a glass substrate (Corning 1737) by facing cathodes DC magnetron sputtering system. We used capacitively coupled plasma etching apparatus (Tokushima Univ.) to etch the samples. The etching gas was N₂, and its pressure and etching time were 100 mTorr and 60 minutes, respectively. These samples were analyzed by NEXAFS method conducted at the beamline BL09A in the NewSUBARU synchrotron radiation facility^[3]. NEXAFS method can obtain the information of chemical state or local structure around the element selectively and non-destructively by measuring an absorption edge of any element in the sample. The measurements were carried out with total electron yield (TEY) method (surface sensitive) and total fluorescence yield (TFY) method (bulk sensitive) at the Ti-L_{2,3} edges (443 ~ 496 eV)^[4]. TFY measurement was carried out with two types of photodiodes. One can cut off visible light by aluminum coating (PD-1), another is uncoated (PD-2). Therefore, it can investigate presence or absence of visible light emission.

Results

As shown in Fig.1 (a), the spectra of etched sample measured by TEY method changed that the peak near 467 eV became lower compared with as-grown sample. However, the spectra of the etched sample recovered to as-grown-like by soft X-ray irradiation (undulator light source, tens of W/cm²) for 1 minute. As shown in Fig.1 (b), the spectra of as-grown sample and etched sample measured by TFY (PD-1) method changed that the peak became lower on the whole absorption region. And the spectra of etched sample were not changed by soft X-ray irradiation. The spectra of etched sample measured by TFY (PD-2) method were the same spectra measured by PD-1 as shown in Fig.1 (c) (middle). However, the spectra of the etched sample recovered to as-grown-like by soft X-ray irradiation for 3 minutes as shown in Fig.1 (c) (higher).

The spectra of as-grown sample and etched sample measured by TFY (PD-1) method were affected by self-absorption which was specific to TFY method. On the other hand, the spectra of etched sample measured by TFY (PD-2) method (middle) was affected by self-absorption, but spectra of as-grown sample (lower) and irradiated sample (higher) were TEY-like without the influence of self-absorption. Thus, we found that the spectra of the etched sample recovered to as-grown-like by soft X-ray irradiation. Fig.2 shows the recovery process of the NEXAFS spectra by soft X-ray irradiation measured with TFY (PD-2) method. The spectrum of etched sample gradually became as-grown-like by soft X-ray irradiation (496 eV, tens of mW/cm²) for 5 ~ 25 minutes.

The recovered spectra of the samples were returned to disordered shape by exposure to air or keeping about three days in vacuum. After returning to the disordered shape, the spectrum changed to as-grown-like again by re-irradiation with soft X-rays. Therefore, the recovery phenomenon is not a permanent change but is a reversible change.

In the etched sample, the bonding orbital around the Ti atoms should be disturbed by generation of oxygen vacancies. The spectra should be disturbed by disarray of crystalline structure. Presumably, the spectra should be recovered by trapped electrons to compensate the defective part. Based on these speculation, we considered that the mechanism of recovery phenomenon is related to the influence of secondary emission. First, we thought about the recovery in TEY method as follows. Electrons from electron-hole pairs generated by the soft X-ray irradiation should be trapped in oxygen vacancies (defects) generated by plasma etching. As a result, it became easier to emit photoelectron by decreases of scattering by the defects. Second, we thought about recovery in TFY method as follows. Spectra of etched sample change to spectra of self-absorption type by suppression of secondary photoemission from as-grown sample. However, the spectra became non-self-absorption (normal) type by change to easily emit light again due to the influence of electrons trapped in the oxygen vacancies. From the measured results of PD-1 and PD-2, the light emissions should be the visible and ultraviolet region, which were cut off by aluminum coating. We considered that the recovery phenomenon is not a permanent change, it returned to disturbed spectra again due to the trapped electrons react with water and oxygen in air or lifetime of the electrons trapped by oxygen vacancies.

References

- [1] K.Sano *et al.*, LASTI. Annual Report **vol.14**, 43-44 (2012).
- [2] M.Niibe *et al.*, J. Appl. Phys., **113**, 126101 (2013).
- [3] M.Niibe *et al.*, AIP Conf. Proc. No.**705** (AIP, New York, 2004), p.576
- [4] T.Kotaka and M.Niibe: Adv. X-ray Chem. Analysis, **43** (2012) 175.

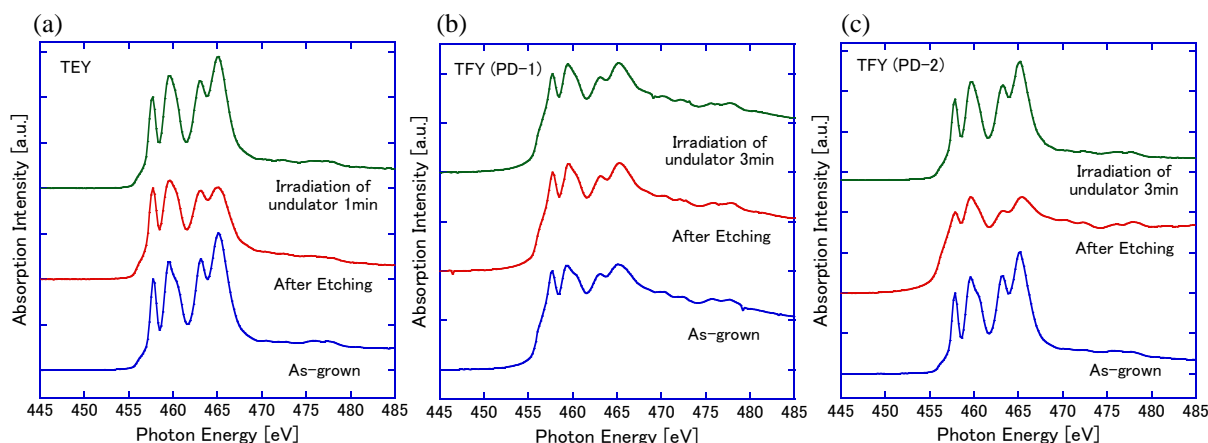


Fig.1 Ti-L_{2,3} NEXAFS spectra of etched TiO₂ thin films
(a): TEY method and (b): TFY (PD-1, Al coated) method and (c): TFY (PD-2, non-coated) method.

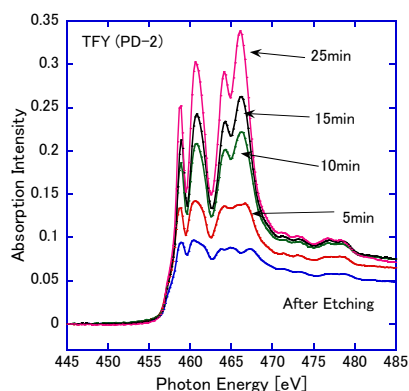


Fig.2 Recovery of Etching Damage by Soft X-ray Irradiation.

Oxidation State Analysis by Soft X-ray Absorption Fine Structure Using $M_{4,5}$ edge of Tin

Takumi Yonemura¹, Junji Iihara¹, Koji Yamaguchi¹, and Masahito Niibe².
¹ Sumitomo Electric Industries, Ltd. ² University of Hyogo

Abstract

We found that soft x-ray absorption fine structure for $M_{4,5}$ edge of Tin was effective for investigating the oxidation states on the surface. Using this method, we have investigated the oxidation state of Sn plate whose surface was processed by the wet thermal oxidation and have found that the oxidation state on the surface became SnO.

Introduction

Tin (= Sn) is widely used for contact materials such as the electroplated layer on the connector and solder. The solder, for example, is an alloy whose main component is Sn. The solder is often used for the connection between the electric parts and the printed circuit in the electric products. The resistivity on that connected regions influences the electric properties. This resistivity depends on the oxidation states of the solder. Therefore, to investigate the oxidation state on the surface region is necessary to develop the process for decreasing the resistivity.

There are some methods for analyzing the oxidation states, for example, the x-ray photoelectron spectroscopy (XPS), the cyclic voltammetry (CV), and so on. XPS can detect the several nm thickness oxidation layers on the surface. However, it is difficult to distinguish the oxidation states between SnO and SnO₂, because the peak positions of the photoelectron spectra for these Sn compounds are very close to each other. CV also can detect the oxidation states. However, it is difficult to investigate the particular region like the surface layer.

We focused on x-ray absorption fine structure (XAFS) which is useful to investigate the chemical state. XAFS spectrum is obtained by measuring the absorbance for the incident x-ray. The absorbance is obtained by measuring the number of the auger electrons, the photo currents, the fluorescence x-ray intensity, and so on, because these signals are in proportion to the absorbance. In addition, the effective depth of the signal for these probes are different each other. This indicates that the analysis depth can be controlled by using them properly.

We tried to investigate the native oxide of Sn plate at BL16B2 of SPring-8 by the conversion electron yield (CEY) which is the surface sensitive method in XAFS and utilizes the auger electrons. Although we obtained the Sn K edge XAFS spectrum, it was almost the same to that of Sn metal. The native oxide couldn't be detected because the energy of the auger electrons was probably high. Therefore, XAFS measurement using the Sn $M_{4,5}$ absorption edge in soft x-ray region could be effective for overcoming that issue and investigating the oxidation state on the surface more sensitive.

In this report, we have considered the XAFS measurement with Sn $M_{4,5}$ absorption edge for the oxidation state analysis on the surface region, using the highly brilliant soft x-ray of NewSUBARU.

Experiments and Results

Five samples were prepared, as listed in Table I. Sample A1 and A2 were SnO and SnO₂ powder as standard, which were fixed on the carbon tape, respectively. Sample B1 and B2 were Sn powder and Sn plate, respectively. Sample C was Sn plate whose surface was processed by the wet thermal oxidation. This process imitated a use environment. The surface of the sample B2 and C was connected to the ground by using the carbon tape to prevent the charge-up phenomenon.

Table I. Prepared Samples

Sample	Details
A1	SnO powder fixed on carbon tape (standard)
A2	SnO ₂ powder fixed on carbon tape(standard)
B1	Sn powder fixed on carbon tape
B2	Sn plate
C	Sn plate with the wet thermal oxidation process

We performed the XAFS measurements using soft x-ray from the synchrotron radiation source at BL9A of NewSUBARU. Figure 1 was the schematic picture of BL9A measurement system. We used the Sn $M_{4,5}$ absorption edge (= 484 eV). Therefore, the excited x-ray energy was varied between 480 and 505 eV with an interval of 0.12 eV. The undulator gap was set to 34.5 mm so that the incident x-ray intensity became stronger in the above energy regions. The grating and exit slit were set to 1200 lines/mm and 50 μ m, respectively. The incident x-ray intensity (I₀) was monitored with the photo currents on the gold-mesh using Keithley6514 type picoammeter. XAFS measurements were performed in a total electron yield (TEY) which

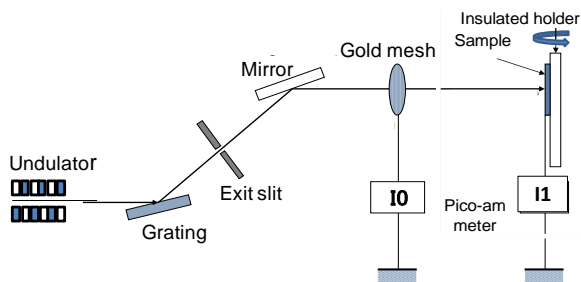


Fig. 1. The measurement system at BL9A

is the surface sensitive mode and utilizes the photo currents. The current (I1) was monitored with a Keithley6517A type picoammeter.

Figure 2 (a) shows the Sn $M_{4,5}$ -XAFS spectra of standard sample A1 and A2 obtained by TEY. Comparing with these two spectra, the XAFS spectrum of SnO has the characteristic peak at 486 eV. On the other hand, that of SnO₂ has the characteristic peak at 490 and 501 eV. These characteristic peaks indicate that the oxidation states of Sn are distinguished clearly by using $M_{4,5}$ -XAFS spectra.

Figure 2 (b) and (c) show the Sn $M_{4,5}$ -XAFS spectra of sample B1 and B2. We found that the XAFS spectrum of sample B1 has three characteristic peaks at 486, 490, and 501 eV. While, that of sample B2 has only one characteristic peak at 486 eV. This indicates that the surface oxidation state of Sn powder, sample B1, was mixed with SnO and SnO₂. On the other hand, that of Sn plate, sample B2, was only SnO. These surface oxidation states probably show the native oxide layer. Above results indicate that Sn $M_{4,5}$ XAFS measurement in TEY is effective for the investigation of the oxidation states on the surface of Sn compounds.

Finally, we have applied the above method to sample C. Figure 2 (d) shows the Sn $M_{4,5}$ -XAFS spectra obtained by TEY. We found that the spectrum was almost the same to that of SnO. In short, the oxidation state became SnO by the wet thermal oxidation process.

In summary, we have considered how to investigate the surface oxidation states of the Sn compounds, and have found that the XAFS measurement by TEY with Sn $M_{4,5}$ absorption edge was effective. We have successfully obtained the Sn $M_{4,5}$ -XAFS spectra from the native oxide layer of Sn plate and Sn powder. The oxidation state of Sn plate and Sn powder were SnO and the mixture with SnO and SnO₂, respectively. Using this method, the effect of the wet thermal oxidation process to Sn plate has been investigated. It has been found that the surface oxidation state became SnO.

References

- [1] M. Niibe, M. Mukai, S. Miyamoto, Y. Shoji, S. Hashimoto, A. Ando, T. Tanaka, M. Miyai, and H. Kitamura, Synchrotron Radiation Instrumentation, AIP Conf. Proc. **705**, 576-579 (2004).

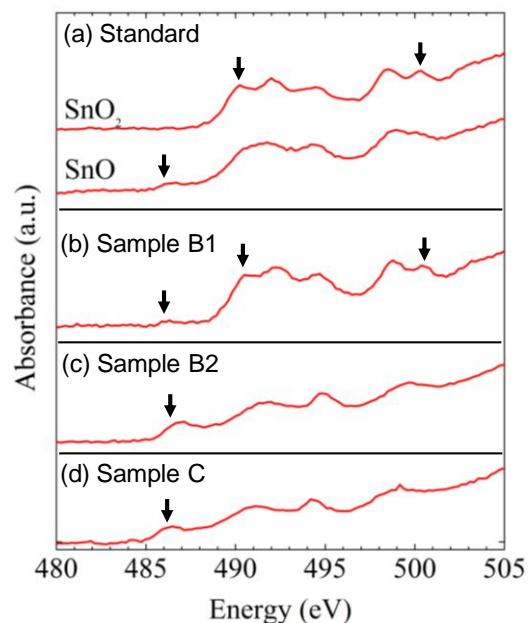


Fig. 2. Sn $M_{4,5}$ -XAFS spectra of (a) SnO powder and SnO₂ powder, (b) Sn powder, (c) Sn plate, and (d) Sn plate with the wet thermal oxidation process

Surface analysis of GaN treated by Ar ion beam etching

Shodai Hirai¹, Masahito Niibe²

Graduate School of Eng¹. and LASTI², University of Hyogo.

Abstract

To understand how would change the surface composition and the etching depth, the surface of n-GaN was etched by Ar ion beam. The etched surfaces were analyzed by two-beam interference microscope, X-ray photoelectron spectroscopy (XPS) and soft X-ray absorption spectroscopy (XAS) methods. The etching rates of n-GaN were about 0.13 nm/min and 0.97 nm/min at the acceleration voltage of 0.5 kV and 1.0 kV, respectively. The surface composition of etched n-GaN changed to Ga-rich as the N/Ga ratio shifts to about 0.5. The relative oxygen content increased about 3 times. The shape of the Near Edge X-Ray Absorption Fine Structure (NEXAFS) of the N-K edge measured by TEY method changed with increasing acceleration voltage and processing time. The appeared peak around 402 eV is explained by formation of N₂ molecules on the sample surface. The disturbance of crystal structure did not occur in deeper region greater than 5 nm.

Introduction

Gallium Nitride (GaN) is expected as semiconductor materials used for power electronic devices and light emitting devices because the band gap of GaN is large and interatomic distance is short. In order to improve the performance of the devices, suppression of etching damage to a circuit during processing is important. However, understanding of reducing the damage to the surface by etching is still insufficient. On the other hand, it is necessary to know the changes in properties of the material by ion beam etching, because ion beam etching is used for depth analysis in materials. Therefore, in this study, we investigated how would change the surface composition, the etching depth, and surface structure when n-GaN was etched by ion beam.

Experimental Methods

The sample was Si dope n-type GaN grown on a sapphire substrate by MOCVD. Etching of n-GaN was carried out using Ar ion beam, the gas pressure of which was 50 μ Torr. Filament current of the ion gun was 25 mA. Acceleration voltage was changed in the range of 0.5-1.0 kV. Processing time was changed up to 3 hours. A part of the n-GaN sample surface was covered with metal mask to make a step by

etching. Further, we investigated the etching depth of a Si wafer to compare the etching rate. After the etching, n-GaN was exposed to atmosphere. We measured etch depth with using two-beam interference microscope.

The composition change of the etched n-GaN surface was analyzed by an XPS method. All XPS spectra were obtained using Shimadzu ESCA-1000 System with a Mg-K α radiation ($h\nu=1253.6$ eV). The N/Ga ratio on the surface was determined from the integrated intensities of Ga3s and N1s peaks. The relative composition deviation was calculated with the N/Ga ratio of the as-grown sample is one.

NEXAFS spectroscopy was conducted at nitrogen K-edge soft X-ray absorption to analyze etching damage. The NEXAFS measurement was carried out at the analyzing station of beamline 9, at the NewSUBARU synchrotron radiation facility at the University of Hyogo. The measurement was carried out by total electron yield (TEY) method in a sample current mode and total fluorescence yield (TFY) method. In TFY method, we measured the amount of fluorescence with an Al-coated photodiode in order to cut off visible light emission[1]. Both measurements were carried out simultaneously for

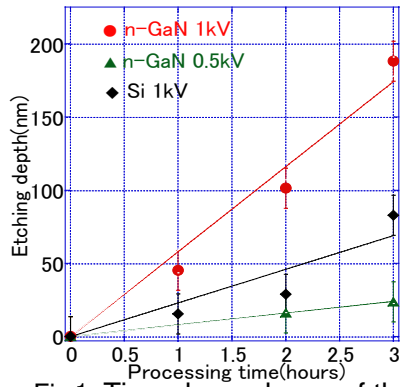


Fig.1. Time dependence of the etch depth of the Si and n-GaN.

the same sample at the same position. TEY method can get information on a shallow region of less than about 5nm from the sample surface because of the short escape length of photogenerated electrons. On the other hand, TFY method can get information on a deeper area (bulk) of the sample of more than 100 nm because X-ray fluorescence comes out from deeper place in the sample compared to electrons.

Results

Figure 1 shows the time dependence of the etch depth of the n-GaN and Si. The etch depth of the n-GaN samples increased almost linearly with increasing the processing time. The etching rate of n-GaN were about 0.13 nm/min at the acceleration voltage of 0.5 kV and about 0.97 nm/min at 1.0 kV. The etching rate of Si was about 0.38 nm/min at the acceleration voltage of 1.0 kV. In the n-GaN samples, the etching rate of 1.0 kV was 7.3 times greater than the case of 0.5kV. The etching rate of n-GaN was 2.5 times greater than that of Si. Binding energy of Ga-N and Si-Si are about 9.0 eV [2] and 3.5 eV [3], respectively. Therefore, we have expected that Si would be etched with higher rate. However, in this study, it was found that the etching rate of n-GaN was higher than that of Si. This is a very interesting result. We will continue to clarify the reason why the etching rate of n-GaN is higher than that of Si, in the future.

Figure 2 shows the composition (N/Ga ratio) and the relative oxygen content of the n-GaN surfaces at the acceleration voltage of 1.0 kV, obtained by XPS method. N/Ga ratio was about 0.5 comparing with that of the as-grown sample in all the etching time. The relative amount of oxygen was about 3 times greater comparing with the as-grown sample in all the

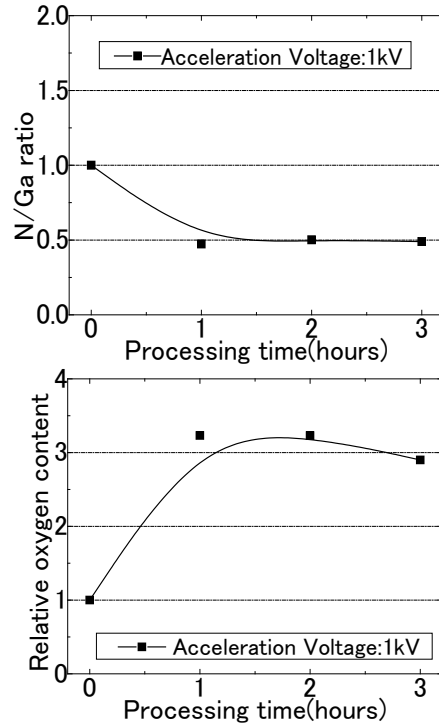


Fig.2. Etching time dependence of N/Ga ratio and the relative amount of oxygen of n-GaN

etching time.

Figure 3 shows the NEXAFS spectra of N-K edge of the n-GaN sample measured by TEY method at the soft X-ray incident angle of 90° from the surface. Figure 3 (a) and (b) show the NEXAFS spectra at the acceleration voltage of 0.5 kV and 1.0 kV, respectively. As shown in Fig. 3, the peak at 403 eV and the spectral shape of other peaks are smoothed when processing time is increased. It indicates that the crystal structure of the n-GaN surface was distorted. In addition in the case of 1.0 kV, a change in the spectral shape was greater than that of 0.5 kV. In TFY method, the spectral shape of overall was not changed with changing in the accelerating voltage (not shown here). It indicates that the disturbance of crystal structure was restricted at the surface.

As shown in Fig. 3 (b), a new peak was formed at the vicinity of 402 eV with increasing in the etching time of 1 and 2 hours. The peak decreased when etching time is increased to 3 hours. The peak around 402 eV is a spectrum derived from N₂ molecules [4]. N₂ molecules were produced on the sample at the early stage of etching, and desorbed when etching time increased.

Dicussion

We consider the changes in the structure of n-GaN by Ar ion beam etching. First, N was selectively etched from the surface of the sample by ion beam etching, and the sample surface became gallium rich. After that, N/Ga ratio became constant at about 0.5 because the selective etching of nitrogen is suppressed by the impinging of Ar ion to more Ga. From the results of TEY method, the disturbance of crystal structure of the sample surface occurs when n-GaN surface is etched. From the results of TFY method, the disturbance does not occur in the deep place from the surface.

References

- [1] T. Kotaka, M. Niibe, and T. Mitamura, *Adv. X-ray. Chem. Analysis, Jap.* **43** 175-180 (2012).
- [2] I. Grzegory, *J. Phys: Condens. Matter.* **13** 6875-6892 (2001).
- [3] Eric J. Lee, et al, *J. Am. Chem. Soc.* **118** 5375-5382 (1996).
- [4] M. Katsikini, et al, *J Phys: Conference Series.* **190** 012065 (2009)

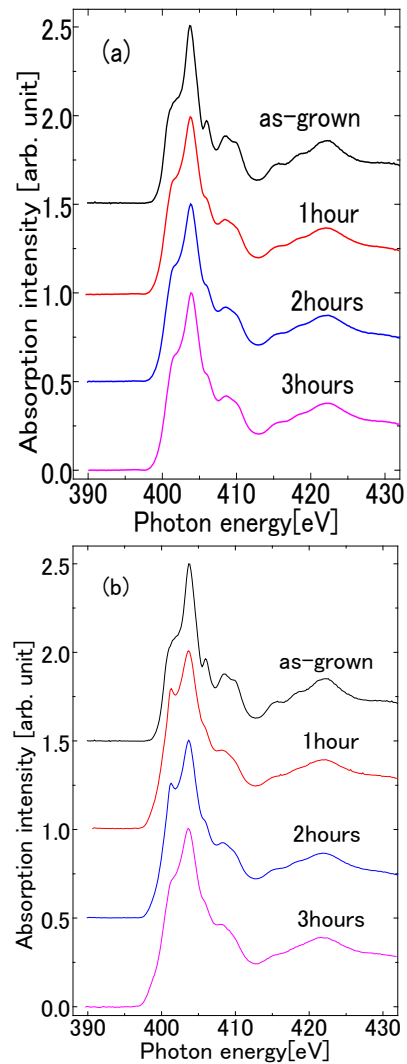


Fig.3. NEXAFS spectra of nitrogen K-edge of n-GaN etched by Ar ion beam, obtained by the TEY method at the soft X-ray incident angle of 90° from the surface. (a) Acceleration voltage of 0.5kV. (b) Acceleration voltage of 1.0kV.

NEXAFS Study on Soft X-ray Irradiation Effect on Highly Hydrogenated Diamond-like Carbon Films

Ryo IMAI, Kazuhiro KANDA

Laboratory of Advanced Science and Technology for Industry, University of Hyogo

Abstract

Structure changes of a hydrogenated diamond-like carbon (H-DLC) film exposed to synchrotron radiation (SR) in the soft X-ray region were investigated by near-edge X-ray absorption fine structure (NEXAFS) spectroscopy using synchrotron radiation. We found that structure of H-DLC films by the SR exposure is greatly modified. The $sp^2/(sp^2+sp^3)$ ratio of C atoms in the H-DLC films, which is quantitatively analyzed from NEXAFS spectra, increased with SR dose.

Introduction

Diamond-like carbon (DLC) films have excellent properties including high hardness, a low friction coefficient, high abrasion quality, a gas barrier, chemical inertness, and surface lubrication and are therefore being utilized as coating materials on automobile parts, hard disks, artificial blood vessels, edged tools, and food containers. Film-forming methods affect the properties of DLC films differently, and thus a wide variety of DLC films have been developed. DLC films are expected to be used in outer space as a lubrication substitution for oil, which cannot be used in space because it disappears in vacuums [1-2].

DLC films are generally known to be durable against X-ray exposure [3]. However, it has recently been reported that soft X-ray exposure on highly hydrogenated DLC (H-DLC) films leads to desorption of hydrogen and an increase in film density and refractive index [4-5]. Clarification of the effect of soft X-ray exposure on DLC films is necessary to ensure that DLC films can be used in outer space safely.

In this study, we investigated the modification processes by soft X-ray exposure on H-DLC films. Specifically C-K edge NEXAFS spectra of H-DLC films were measured using SR, and the $sp^2/(sp^2+sp^3)$ ratio of C atoms in the H-DLC films were obtained.

Experiments

200-nm-thick H-DLC films were deposited on Si wafers by using an amplitude-modulated RF plasma-enhanced CVD method. This method enables the deposition of DLC films containing a lot of hydrogen. The hydrogen content of H-DLC films was estimated to be ≈ 50 at.% by using the combination of Rutherford backscattering spectrometry (RBS) and elastic recoil detection analysis (ERDA) techniques [6].

The SR irradiation of the H-DLC films was carried out at BL06 of the NewSUBARU synchrotron facility. The SR at the BL06 sample stage had a continuous spectrum from IR to soft X-rays, lower than 1 keV. This includes 300 eV, which is the ionization energy of a carbon K shell. As a result, the K-shell electrons of the C atoms could be excited by the SR at BL06. During this experiment, the electron energy of the NewSUBARU ring was 1.0 GeV. The BL06 sample stage was room temperature and the pressure in the chamber was the order of 10^{-5} Pa. An SR dose [mA·h] is derived from the product of the ring current [mA] and exposure time [h].

NEXAFS spectra were measured by total electron yield (TEY) method at BL09A of the NewSUBARU. This measurement enabled us to know information on the local structure near surface of sample. The SR exposure to sample carried out at magic angle (54.7°) with respect to the surface of the sample. The measured energy range in the experiment was 270-330 eV of C-K edge, and the energy resolution was about 0.5 eV.

Results and discussion

Figure 1 shows C-K edge NEXAFS spectra of H-DLC films exposed to the SR, that of the H-DLC film before exposure and that of a commercial DLC film as a typical DLC films. This commercial DLC film was deposited on 200 nm-thick on Si wafers by using ion plating method and it was named an IP-DLC film. A sharp π^* peak observed at 285.38 eV is ascribed to $C1s \rightarrow \pi^*$ resonance transition originating from carbon double bonding. A broad σ^* peak observed at about 285-310 eV is ascribed to $C1s \rightarrow \sigma^*$ resonance transition.

In the C-K edge NEXAFS spectrum of H-DLC before exposure, specific peaks were observed at around 290 eV and 300-305 eV unlike IP-DLC as shown in Fig. 1. Intensity of these specific peaks in spectrum of H-DLC films became to decrease with increasing of the SR dose, and these peaks in spectrum of the H-DLC films after 200 mA·h SR dose exposure disappeared. As a result, this spectral feature of the H-DLC films after the SR exposure of more than 200 mA·h became to resemble that of IP-DLC film. That means the SR exposure to H-DLC films led to the structural change close to typical DLC films. These changes of C-K edge

NEXAFS spectra are considered to correspond to hydrogen desorption from films. In addition, these change occurred at the SR exposure less than 200 mA·h. Specific peaks observed in the C-K edge NEXAFS spectrum of H-DLC films before exposure are ascribable to hydrogen bond in H-DLC films.

Figure 2 shows the SR dose dependence of $sp^2/(sp^2+sp^3)$ ratio of H-DLC films. These ratios were quantitatively estimated by C-K edge NEXAFS spectra of H-DLC films in Fig. 1. The amount of sp^2 bonded carbon atoms can be extracted by normalizing the area of the resonance corresponding to $1s \rightarrow \pi^*$ transitions at 285.4 eV with the area of a large section of the spectrum. The absolute $sp^2/(sp^2+sp^3)$ ratio was determined by the comparison with that from the NEXAFS spectrum of graphite.

The $sp^2/(sp^2+sp^3)$ ratio of H-DLC films before exposure was ≈ 0.33 and it increased rapidly with SR dose in the region less than 200 mA·h. However the SR dose above 200 mA·h, the $sp^2/(sp^2+sp^3)$ ratio was approximately constant at ≈ 0.50 .

Conclusions

In the C-K edge NEXAFS spectra of H-DLC films before exposure, specific peaks were observed. The structure of this spectra greatly changed in the SR dose region less than 200 mA·h. As a result, the C-K edge NEXAFS spectra of H-DLC films became to resemble that of IP-DLC film, which can be regarded as a typical DLC film.

The $sp^2/(sp^2+sp^3)$ ratio increased rapidly from ≈ 0.33 to ≈ 0.50 by the SR exposure to H-DLC of 200 mA·h. It was constant at ≈ 0.50 in the SR dose region over 200 mA·h.

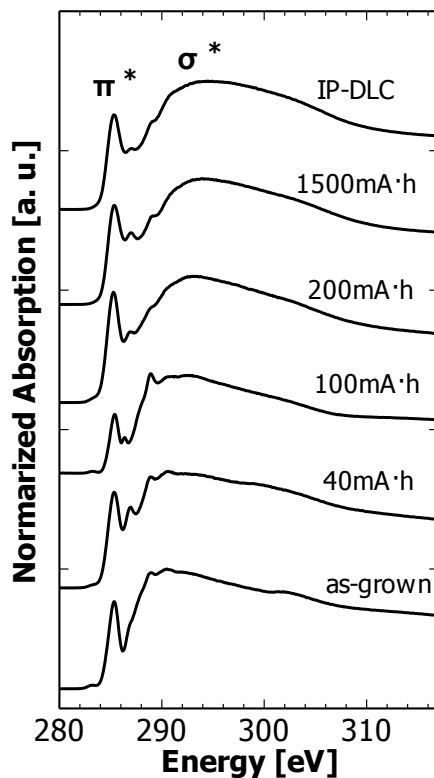


Fig. 1. C K-edge NEXAFS spectra of H-DLC films before and after exposure to Soft X-ray and IP-DLC

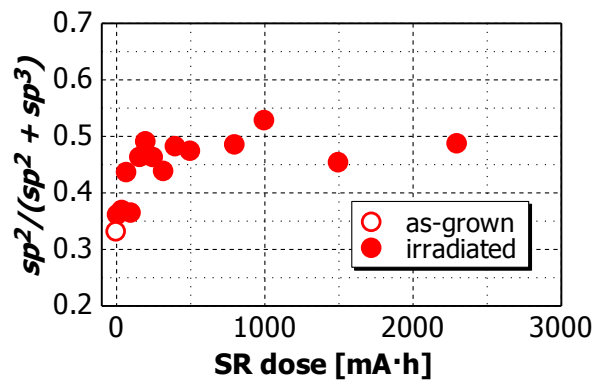


Fig. 2. SR dose dependence of $sp^2/(sp^2+sp^3)$ of H-DLC films calculated by their C-K edge NEXAFS spectra

References

- [1] C. Donnet *et al.*, Tribology of Diamond-like Carbon, Springer (2008).
- [2] C. Donnet *et al.*, Surf. Coat. Technol. 68-69 (1994) 626.
- [3] H. Kyuragi *et al.*, Appl. Phys. Lett. 50 (1987) 1254.
- [4] K. Kanda *et al.*, Jpn. J. Appl. Phys. 50 (2011) 055801.
- [5] H. Matsuura *et al.*, SEI Tech. Rev. 171 (2007) 36 [in Japanese].
- [6] R. Imai *et al.*, Diamond Relat. Matter. 44 (2014) 8-10.

Atomic Oxygen Beam Irradiation Effect on the Si-doped DLC Film

Kengo Kiden¹), Minami Endo¹), Ryo Imai¹), Masahito Niibe¹), Kumiko Yokota²),
Masahito Tagawa²), and Kazuhiko Kanda¹

¹Laboratory of Advanced Science and Technology for Industry, University of Hyogo

²Faculty of Engineering, Kobe University

Abstract

Irradiation effect of an atomic oxygen beam on Si-doped Diamond-Like Carbon (Si-DLC) films was investigated by the measurements of near edge X-ray absorption fine structure (NEXAFS) spectra and X-ray photoelectron spectra (XPS). We found that carbon atom in the Si-DLC film was desorbed from surface and silicon oxide was formed on the Si-DLC surface by the irradiation of atomic oxygen. On the other hand, it was concerned that no change in the thickness of Si-DLC film occurred by the irradiation of atomic oxygen from the Rutherford backscattering spectrometry (RBS) study.

Introduction

Diamond-like carbon (DLC) films are expected to use as lubrication materials in space, where oil cannot be used, because they exhibit excellent low friction properties both in a vacuum and in air. The region less than 2000 km above the ground, where almost artificial satellites are positioned, are called “low Earth orbit (LEO)”. In this orbit, artificial satellites and spacecrafts are exposed to atomic oxygen, which is the dominant species in the upper atmosphere of the Earth. However, it was found that DLC films were etched by the collision with atomic oxygen in our previous work¹). Recently, Si-doped DLC films have been widely used due to their oxidation resistance. In the present study, we investigated the resistance of Si-DLC film against atomic oxygen and elucidated the mechanism of this durability, to use Si-DLC film as lubrication material in LEO.

Experiments

Si-DLC films were deposited on a Si substrate by plasma-enhanced chemical vapor deposition (PE-CVD). These Si-DLC films consist of $\approx 50\%$ hydrogen and $\approx 10\%$ Si. We exposed Si-DLC films to an atomic oxygen beam with a collisional energy of 5.46 eV, which corresponded to the collisional energy at LEO, by laser detonation-type beam apparatus (Kobe University)²). In the present study, the fluence of atomic oxygen beam exposed to Si-DLC film corresponded to 1.16×10^{17} , 3.52×10^{17} , 1.16×10^{18} , and 1.16×10^{19} atoms cm^{-2} .

We investigated the effect of atomic oxygen exposure on the Si-DLC films by measuring the NEXAFS spectra and RBS spectra. The measurement of NEXAFS spectra were carried out at beamline 09A in the NewSUBARU synchrotron radiation facility. Film thickness of the Si-DLC surfaces was estimated by RBS measurement using electrostatic tandem foundation graph accelerator 5SDH (Kobe University).

Results

Variations in the local structure of the Si-DLC film due to the exposure to an atomic oxygen beam are discussed on the basis of the NEXAFS measurements. Fig. 1 shows the C *K*-edge NEXAFS spectra of Si-DLC films exposed to an atomic oxygen beam with that of a Si-DLC film before exposure. The spectrum of SiC powder is also shown for a reference. The resonance peak at 285.4 eV was ascribed to the transition from the C 1s level to unoccupied π^* orbit principally originated from sp^2 (C=C) sites. The broad band observed in the photon energy region of 290-320 eV was ascribed to the transitions from C 1s level to unoccupied σ^* states.

With increasing of fluence of atomic oxygen, the intensity of the sharp peak at 285.4 eV decreased, and spectral shape of broad peak at 290-320 eV became sharper. When the fluence of atomic oxygen was beyond 1.16×10^{19} atoms cm^{-2} , the C *K* NEXAFS spectrum of Si-DLC film resembled well the spectrum of SiC powder. From this observation, the dominant species bonding to C atom in the Si-DLC can be considered to change from C=C sites from Si-C sites.

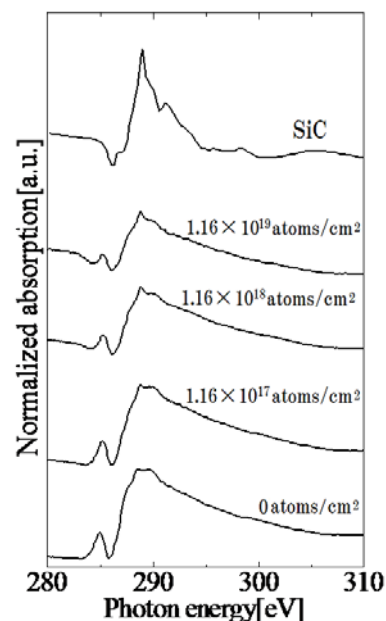


Fig. 1 C *K*-edge NEXAFS spectra of Si-DLC films and SiC powder

This conclusion was supported from the measurement results of O *K*-edge and Si *L*-edge NEXAFS spectra. From the measurement of O *K*-edge NEXAFS spectrum, intensity of the peak derived from SiO₂ increased with fluence of atomic oxygen. After the irradiation of atomic oxygen beyond 1.16×10^{19} atoms cm⁻², the spectral features of O *K* NEXAFS spectrum of Si-DLC film changed into a similar shape with the spectrum of SiO₂. In the Si *L*-edge NEXAFS spectrum of the Si-DLC film before exposure, most of structural peak was not observed as well as that of SiC powder. With fluence of atomic oxygen, structural peaks were observed in the Si *L*-edge NEXAFS spectrum. After the irradiation of atomic oxygen beyond 1.16×10^{19} atoms cm⁻², the spectral features of Si *L* NEXAFS spectrum of Si-DLC film changed into a similar shape with the spectrum of SiO₂. From these NEXAFS study, the Si atoms almost bonded with C atoms before exposure to an atomic oxygen beam and the Si atom bonding to O atom increased with the fluence of the atomic oxygen beam on the surface of Si-DLC films.

Elementary composition of the surface of Si-DLC films due to the irradiation of an atomic oxygen beam was estimated by the measurement of the XPS spectra. Fig. 2 shows the XPS spectra of the Si-DLC films before and after exposure to an atomic oxygen beam. Several peaks originating from C, Si, and O atoms, were observed in the spectrum of Si-DLC films before exposure. The peaks at 532, 235, 153, and 102 eV were assigned to the O1s, C1s, Si2s, and Si2p, respectively. After exposure to an atomic oxygen beam, the intensity of the peaks originating from the Si and O atoms increased and those originating from the C atoms decreased. The results of elementary analysis are listed in Table 1. The amounts of Si and O atom in the Si-DLC films increased with the fluence of the atomic oxygen beam. However, that of C atoms decreased monotonically.

These variation of elementary composition of the surface of Si-DLC films by the exposure to atomic oxygen beam can be considered as follows: C atoms decreased due to desorption from Si-DLC film by the irradiation of atomic oxygen, to form gas species, CO and/or CO₂. O and Si atoms increased due to the formation of Si oxide by the irradiation of atomic oxygen. Si oxide was not eliminated from Si-DLC film because it is solid, unlike oxide of C.

Variations in thickness of Si-DLC films due to the irradiation of an atomic oxygen beam were estimated by the measurement of RBS. Fluence dependence of film thickness was depicted in Fig. 3. Film thickness of DLC film, which did not include Si atom, was reported to decrease with atomic oxygen fluence¹⁾, whereas that of Si-DLC film was constant after the exposure to atomic oxygen beam.

From these results, the C atoms on the Si-DLC surface were desorbed as the CO and/or CO₂, but Si atoms were remained on the Si-DLC surface as the SiO_x. It was interpreted that this SiO_x layer disturbed the erosion of bulk film against atomic oxygen.

Reference

- [1] M. Tagawa *et al.*, Appl. Surf. Sci., **256**, pp. 7678-7683 (2010).
 [2] K. Yokota *et al.*, J. Spacecraft Rockets, **40**, pp. 143 (2002).

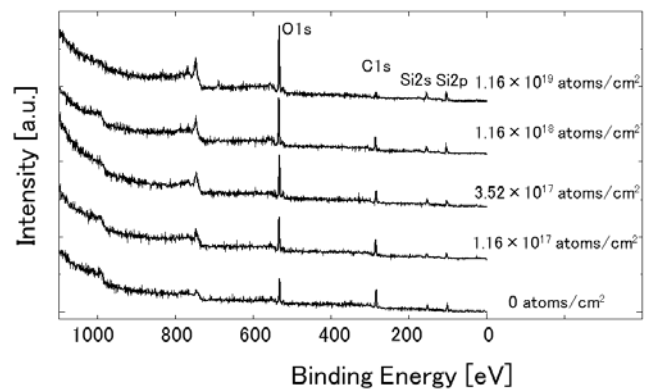


Fig. 2 XPS spectra of Si-DLC films before and after exposure to atomic oxygen beam.

Table 1

Elementary composition of the surface of Si-DLC films before and after exposure to atomic oxygen beam.

Fluence atoms cm ⁻²	C	O at. %	Si
0	10	54	37
1.2×10^{17}	15	45	40
3.5×10^{17}	16	39	44
1.2×10^{18}	21	28	51
1.2×10^{19}	22	24	55

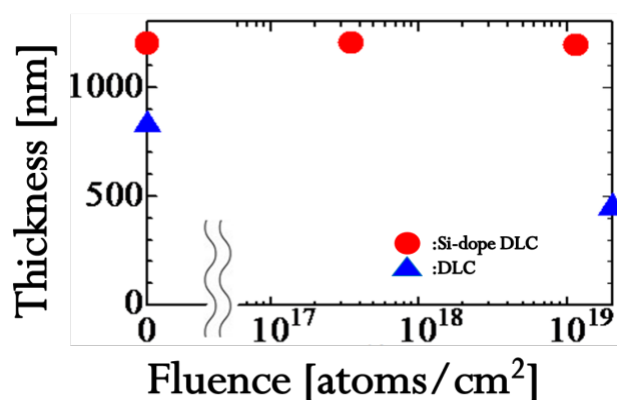


Fig. 3 Fluence dependence of Film thickness

Molecular Orientation at the Near-surface of Photoaligned Films Determined by NEXAFS

Yuichi Haruyama¹, Makoto Okada¹, Emi Nishioka², Mizuho Kondo², Nobuhiro Kawatsuki², and Shinji Matsui¹

¹Laboratory of Advanced Science and Technology for Industry, University of Hyogo

²Department of Materials Science and Chemistry, Graduate School of Engineering, University of Hyogo

Abstract

Near-edge X-ray absorption fine structure (NEXAFS) spectra of polymethacrylate, which has a hexamethylene spacer group terminated with a 4-oxycinnamic acid in its side chain (P6CAM), were measured at the C K-edge region. Several peaks in the NEXAFS spectra of photoaligned P6CAM films were observed and the resonances at 285 eV, 288 eV, and 293-305 eV were assigned to carbon 1s to \tilde{A}^* of the phenyl rings, carbon 1s to \tilde{A}^* of C=O, and carbon 1s to \tilde{A}^* transitions, respectively. From the dependence on the incident angle of the linear polarized synchrotron radiation in the NEXAFS spectra of photoaligned P6CAM films, it was found that the liquid crystals orient perpendicular to the polarization direction of the UV light.

Introduction

Studies on the photoinduced orientation of the polymeric films have attracted significant attention for a potentially wide range of applications such as birefringent optical devices, the photo alignment layer of liquid crystal displays, optical memories, and holographic data storage devices [1-2]. Optical anisotropy of the polymeric films is created by irradiating the polarized UV light to the films. The polymethacrylate, which has a hexamethylene spacer group terminated with a 4-oxycinnamic acid in its side chain (P6CAM), is a photoreactive liquid crystalline polymer comprised of cinnamic ester side groups as shown in Fig. 1. It was observed that the molecular orientation of photoreactive liquid crystalline polymer controlled by the linearly polarized UV radiation and the subsequent annealing procedure [3-5]. In this study, we obtained the C K-edge NEXAFS spectra of P6CAM in order to investigate the molecular orientation at the near-surface of the photoreactive liquid crystalline polymers.

Experiments

P6CAM were synthesized as described in a previous paper [3]. Thin films of P6CAM were prepared by spin-coating a tetrahydrofuran (THF) solution of polymers onto ITO coated SODA glasses. The thickness of the thin films was 170 nm. The photoaligned thin films of P6CAM were prepared by irradiating the linear polarized UV light to the films and by subsequently annealing at 180 °C for 10 minutes. After the procedures, the liquid crystal part of P6CAM reorients to the vertical to the polarization direction of the linear polarized UV light.

All NEXAFS spectra measurements were carried out using the BL-7B beamline of the NewSUBARU synchrotron radiation facility at the University of Hyogo. As an excitation source, linear polarized synchrotron radiation with photon energy (h ν) range from 280 to 330 eV was used and the total energy resolution was about 0.5 eV. NEXAFS spectra were measured by the total electron yield method. The base pressure in the NEXAFS measurements chamber was 2×10^{-8} Pa. The sample could be rotated around a vertical axis to change the incident angle θ of the synchrotron radiation to the sample surface. The direction of the polarization in the synchrotron radiation was horizontal. To reduce the irradiation damage of the samples, the samples were cooled at about 80 K and NEXAFS spectra were recorded at this temperature. In addition, the sample was shifted to a different position after each measurement of the NEXAFS spectrum.

Results

Figure 2 shows the C K-edge NEXAFS spectra of photoaligned P6CAM films as a function of incident angle θ of the synchrotron radiation. NEXAFS spectra are aligned in increasing order of the incident angle θ from the bottom. The reoriented direction of the liquid crystal in P6CAM was parallel to the incident plane of the synchrotron radiation. The NEXAFS spectra were normalized by the edge-jump intensity. Two sharp peaks were observed at 285 and 288 eV were observed. In addition, two broad peaks were visible at 293-305 eV. With increasing the incident angle θ , the intensity of the peak at 285 eV was remarkably decreased while the intensities of the peaks at 293-305 eV were increased. In the case that the reoriented direction of the liquid

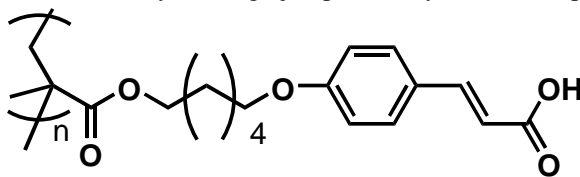


Figure 1. Chemical structure of P6CAM.

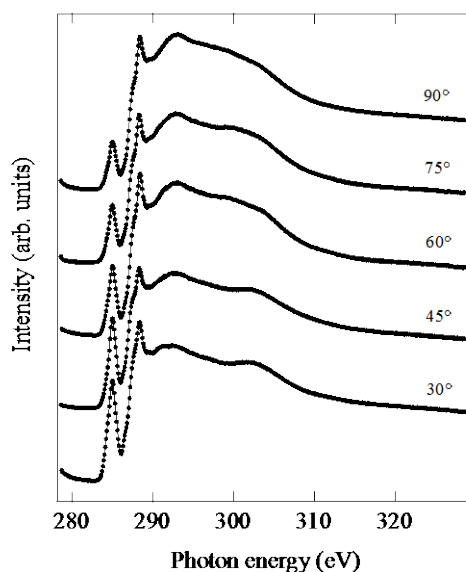


Figure 2. C K-edge NEXAFS spectra of photoaligned P6CAM films as a function of the incident angle θ , relative to substrate surface. The reoriented direction of the liquid crystal in P6CAM was parallel to the incident plane of the synchrotron radiation.

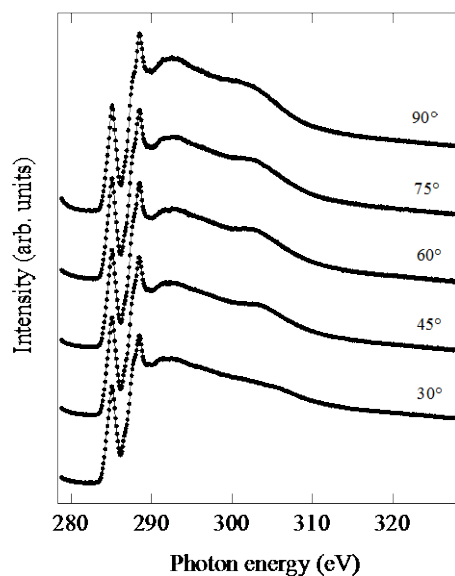


Figure 3. C K-edge NEXAFS spectra of photoaligned P6CAM films as a function of the incident angle θ , relative to substrate surface. The reoriented direction of the liquid crystal in P6CAM was perpendicular to the incident plane of the synchrotron radiation.

crystal in P6CAM was perpendicular to the incident plane of the synchrotron radiation, the C K-edge NEXAFS spectra of photoaligned P6CAM thin films as a function of incidence angle θ of the synchrotron radiation was shown in Fig. 3. With increasing the incident angle θ , the intensity of the peaks at 285 eV was not changed while the intensities of the peaks at 293-305 eV were slightly increased. Thus, from the difference on the angular dependence of the NEXAFS spectra, it was confirmed the anisotropy of photoaligned P6CAM thin films. In the C K-edge NEXAFS spectrum, transitions from the C 1s orbital to the unoccupied π^* and \tilde{A}^* orbitals are observed at specified sites. In P6CAM, the resonances at 285 eV, 288 eV, and 293-305 eV correspond to carbon 1s to \tilde{A}^* of the phenyl rings, carbon 1s to \tilde{A}^* of C=O, and carbon 1s to \tilde{A}^* transitions, respectively. Figure 4 shows the angular dependence of the π^* resonance intensity in the parallel and perpendicular geometries for photoaligned P6CAM thin films. From the angular dependence of the π^* resonance intensity, it was found that the liquid crystals orient perpendicular to the polarization direction of the UV light.

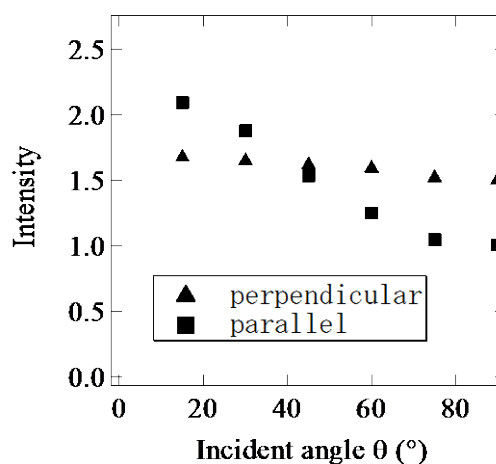


Figure 4. Angular dependence of the resonance intensity in the parallel and perpendicular geometries for photoaligned P6CAM thin films.

References

- [1] N. Kawatsuki and H. Ono: *Org. Electron. Photonics* **2** (2007) 301.
- [2] N. Kawatsuki, H. Ono, H. Takatsuka, T. Yamamoto, and O. Sengen: *Macromolecules* **30** (1997) 6680.
- [3] N. Kawatsuki, T. Kawanishi, and E. Uchida: *Macromolecules* **39** (2006) 9357.
- [4] M. Okada, S. Manabe, M. Kurita, M. Kondo, Y. Haruyama, K. Kanda, A. Emoto, H. Ono, N. Kawatsuki, and S. Matsui: *Jpn. J. Appl. Phys.* **49** (2010) 128004.
- [5] M. Okada, S. Manabe, M. Kurita, M. Kondo, Y. Haruyama, K. Kanda, N. Kawatsuki, and S. Matsui: *Microelectronic Engineering* **88** (2011) 2079.

EUV Resist Chemical Reaction Analysis using SR

Takeo Watanabe¹⁾, Kazuya Emura¹⁾, Daiju Shiono³⁾, Yuichi Haruyama¹⁾, Yasuji Muramatsu²⁾,
Katsumi Ohmori³⁾, Kazufumi Sato³⁾, Tetsuo Harada¹⁾, and Hiroo Kinoshita¹⁾

¹Center for EUVL, LASTI, University of Hyogo,
3-1-2 Kouto, Kamigori, Ako-gun, Hyogo 678-1205, Japan.

²Graduate School of Engineering, University of Hyogo,
2167 Shosha, Himeji, Hyogo 671-2280.

³Tokyo Ohka Kogyo,
1590 Tabata, Samukawa, Koza, Kanagawa, 253-0114, Japan.

The chemical reaction in EUV irradiation of the several photoacid generators (PAGs) which employed triphenylsulfonium (TPS) salts as the cation of PAG, is discussed on the basis of the analysis using the SR absorption spectroscopy in the soft x-ray region. The fluorine atoms of the anion PAGs which have the chemical structure of the imidate type such as TPS-Imidate-1, and TPS-Imidate-2 strongly decomposed under EUV exposure. In the case of these PAG type, it is found that in addition to the ionization reaction, the anion decomposition reaction originated by the photo excitation of the photoacid generator might occur under EUV exposures. Thus the sensitivity seemed to be high comparison to tri-phenylsulfonium perfluorobutanesulfonate (TPS-Nonaflate) under EUV exposure. In the case of tri-phenylsulfonium camphorsulfonate (TPS-Cs), the anion which does not contain fluorine seemed to be very stable under EUV exposure and the sensitivity is lower than TPS-Nonaflate.

Keyword: EUVL, chemically amplified resist, photoacid generator, decomposition of anion of PAG, SR absorption spectroscopy

1. Introduction

The extreme ultraviolet lithography (EUVL)¹⁾ will be used from 16-nm node for the manufacturing semiconductor electronic devices such as memory and MPU devices. And according to the International Technology Roadmap for Semiconductors (ITRS), 8-nm node lithography is required from 2025.²⁾

The top three issues of EUV lithography for high volume manufacturing (HVM) are 1) the achievement of the high power and a long term stable EUV source, 2) the fabrication of the defect free mask and its defect inspection and repair, and 3) the development of the EUV resist which has the high resolution, the high sensitivity, low line width roughness (LWR), and low outgassing and low carbon contamination, simultaneously.

To relax the specification of the EUV power and maintain the high-lithographic throughput, the high sensitive EUV resist is required. The low

activation energy chemically amplified³⁻⁵⁾ resist were performed for the high sensitive resist, but the LWR not refined.⁶⁾ The LWR is one of the resist issues to maintain the device electric performance. There are many reports to improved LWR from resist material development. One is the application of compounds of low molecular weight and/or narrow polymer dispersity⁷⁻¹¹⁾ and monomer resist¹²⁻¹⁷⁾ may be one of the key concepts to resolve this issue due to its reduced molecular size compared with linear polymers against the intended feature print size.

There is a trade-off relationship between resolution, sensitivity, and LWR; so called RLS trade-off.^{18,19)} Now the resolving this trade-off relationship 1X nm node and below becomes very significant and difficult issue.^{20,21)} Thus more fundamental resist studies for 1X nm and below is required to clarify the chemical reaction under EUV exposure.

To increase the sensitivity and decrease the

LWR, the acid production yield should increase. Although the acid production yield of the photoacid generator (PAG) of the chemically amplified resist had been studied^{22,23}, the requirement of the EUV resist was still not satisfied yet. Thus, more effective fundamental work should require to be clarified the chemical reaction under EUV exposure. The photo-ionization (ionization) reaction might be dominant and the secondary electron plays the important role in the chemical reaction under EUV exposure²³. In addition, we had found out that the decomposition reaction was occurred near the large photo absorption atom in the solvent, so called “solvent effect”²⁴. In the case of the PAG chemical reaction analysis in EUV irradiation, not only ionization reaction but also the direct excitation in EUV irradiation might be needed to achieve the high sensitive EUV resist. In the previous report, for resists which employed tri-phenylsulfonium cyclo(1,3-perfluoropropanedi-sulfone) imidate (TPS-Imidate-1) and tri-phenylsulfonium perfluorobutane- sulfonate (TPS-Nonaflate) as PAGs, the peak at the absorbance at 1156 cm^{-1} in the fourier transform infrared (FT-IR) spectra increased after EUV exposure.²⁵⁻²⁹ As a results of the electron orbital calculation using perturbation theory by the software code Gaussion03³⁰, the peak at approximately 1156 cm^{-1} in FT-IR spectra of resist A corresponds to the C-F bonding of the anion of TPS-Imidate-1. However, there was no change in the FT-IR spectra of resist which include TPS-Nonaflate, between before and after EUV exposure. As a result, the outgassing measurements

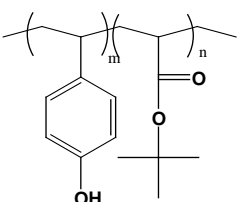
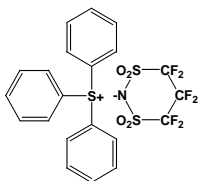
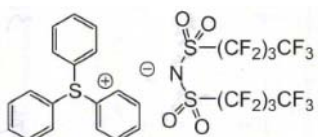
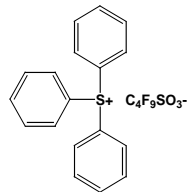
and the FT-IR spectra measurements indicated that the EUV-induced reaction of TPS-Imidate-1 occurred more efficiently than that of TPS-Nonaflate. To clarify the difference of the anion decomposition, the analysis using SR spectroscopy is performed. This paper focused on the chemical reaction analysis of the model chemically amplified resists which contains several PAG on the basis of tri-phenylsulfonium by the SR absorption spectroscopic method³².

2. Experimental

2.1. Materials for the Model Resists

The model resists which were employed in this study are shown in Table 1. The resists A, B, C, and D employed poly (hydroxystyrene-co-t-butylacrylate) (PHS-TBA) as the base polymer, and propyleneglycol monomethyletheracetate (PGMEA) as a solvent. The model resists A does not include any photoacid generator. Model resists, A, B, C and D employed TPS-Imidate-1 and TPS-Imidate-2, TPS-Nonaflate, and TPS-Cs as the photoacid generator, respectively. The PAG content#1 and content#2 ratio to the base resin such as PHS-TBA is approximately 2 mol% and 6 mol% of the base polymer for the sensitivity measurement and the SR absorption spectroscopy experiment, respectively. In sensitivity measurement, the PAG content#1 of 2 mol% is a normal value. However, the PAG content for SR absorption spectroscopy experiment should be larger than that for sensitivity measurement, because in SR spectroscopy experiment the signal from the atomic elements of the resist film is too small

Table 1. Chemical structure and contents of the model resists.

Sample	Resist A	Resist B	Resist C	Resist D
Base polymer	 <p style="text-align: center;">poly (vinylphenol-co-tert butylacrylate) (PHS-TBA)</p>			
Photoacid generator	TPS-Imidate-1 	TPS-Imidate-2 	TPS-Nonaflate 	TPS-Cs 
(content#1)	(2.04 mol%)	(1.34 mol%)	(2.02 mol%)	(2.09 mol%)
(content#2)	(6.11 mol%)	(4.03 mol%)	(6.06 mol%)	(6.18 mol%)
Solvent	propylene glycol monomethylether acetate (PGMEA)			

when the PAG content is 2 mol%.

The resist solution was spin coated on a 4-inches silicon wafer and the prebake was carried out on a hot plate at the temperature of 130°C in the time period of 90 s. The film thickness was measured by Nanometrics 6100A (NANOmetrics) and the resist film thickness was spin-coated to be 50 nm on a wafer. The EUV exposure to obtain the sensitivity curve in high accuracy, the resist sensitivity evaluation⁸⁾ system which can simulate the EUV exposure spectrum of the six-mirror-imaging optics was installed at the BL3 beamline in NewSUBARU synchrotron radiation facility³¹⁾ was utilized. This EUV spectrum which is same as the practical exposure tool such as ASML NXE3100B can be produced by the seven-time reflection by three-mirror optics.

2-2. SR photo absorption spectroscopy³²⁾

X-ray spectroscopy (XPS) is a beneficial measurement method to analyze the atomic chemical behavior of the material. However, for the absorption spectroscopy measurement of the atomic which is a small content such as the photoacid generator of the EUV resist, the high brilliance light source such as synchrotron radiation (SR) light is beneficial in absorption spectroscopy. Thus, soft x-ray of the SR absorption spectroscopy was employed for the chemical reaction analysis for the EUV resist materials.

The SR absorption spectroscopy measurements were performed at the end station of the BL07B beamline at the NewSUBARU synchrotron radiation facility. The short undulator was employed as a light source of this beamline. This beamline consists of three glancing mirrors such as M_0 , M_1 and M_2 , the monochromator (G), the entrance (S_1) and exit (S_2) slits and the end station exposure and analyzing chambers. The loadlock chamber was adapted to these chambers to exchange the sample. The variable-line-spacing plane gratings (VLSPG) were employed as monochromator. Three density types such as 600, 1200, and 2400 lines/mm were installed in the monochromator vacuum chamber. The photon energy region is from 80 eV and 800 eV in the SR spectroscopy. The exit slit size is 20 μm (H) \times 20 μm (V) and the SR light spot size on a sample is 1 mm(H) \times 1 mm (V). The energy resolution $E/\Delta E$ is approximately 1000. The photon flux of the photon energy of 91.8 eV ($\lambda=13.5$ nm)

is approximately 3.0×10^{11} photons/s/100mA. The absorption signal was obtained from the ratio of the photocurrent from the sample to the photocurrent from the gold mesh. The total energy resolution was approximately 0.1 eV. The photocurrent was measured by the electrometer (6514, Keithley).

The photon energy calibration was carried out by measuring the photon absorption spectrum of highly oriented pyrolytic graphite (HPOG). The photon energy at the absorption peak of the carbon π^* -bonding was adjusted at the photon energy of 285.5 eV.

For the absorption measurement of carbon 1s core level, the measured energy region is 280-330 eV and 1200 lines/mm VLSPG was employed with the undulator gap of 48.0 mm. For the absorption measurement of fluorine 1s core level, the measured energy region is 685-735 eV and 2400 lines/mm VLSPG was employed with the undulator gap of 52.0 mm. The electron current generated on the sample is measured in the SR absorption experiment during the SR light exposure.

3. Results and Discussions

3.1 Sensitivity

The sensitivities curves of the resists A, B, C and D under EUV are shown in Fig. 1. The E_0 values which is the exposure dose to clear the resist remained thickness after the development, of resists A, B, C and D are 1.1 mJ/cm^2 , 2.7 mJ/cm^2 , 3.8 mJ/cm^2 , and 6.0 mJ/cm^2 , respectively. The sensitivity differences of resists A, B, C, and D under EUV exposure would be discussed by the analysis of the SR photo absorption spectroscopy in the soft x-ray region.

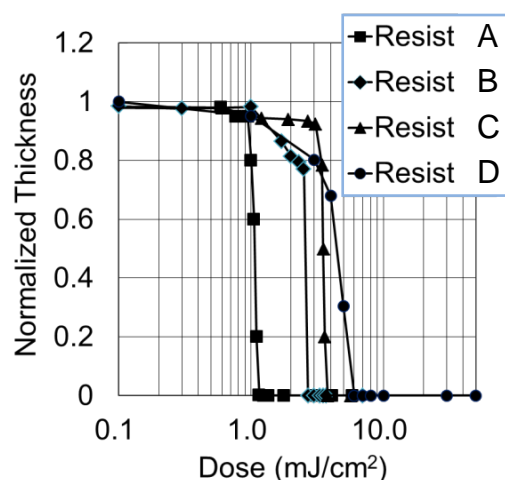


Fig.1 Sensitivity curves under EUV exposure for model resist A, B, C, and D.

3.2 SR absorption spectroscopy

The absorption spectra of carbon 1s core level for resists A, B, C and D were measured as shown in Figs 2, 3, 4 and 5, respectively. For each sample the measured energy range was from 280 eV to 330 eV. To highlight the peak height changes, the SR absorption spectra were plotted in the energy region from 280 eV to 295 eV. The absorption peak at 285.5 eV is corresponding the π^* -bonding of the benzyl group in the cation of PAG (TPS). From the outgassing results²⁵⁻²⁹, this changes correspond to the cation of PAG such as TPS decomposition occurred by the secondary electron originated by the EUV irradiation as shown in Fig. 6. As the increasing the EUV dose, the absorption spectra of the π^* -bonding became smaller. Furthermore, the absorption peak at 287 eV corresponds to the σ^* -bonding of the protection group of tert-butylacrylate (TBA) of the base polymer. From the outgassing results²⁵⁻²⁹, this changes correspond only to the protecting group decomposition reaction of TBA in base polymer occurred by the secondary electron originated by the EUV irradiation as shown in Fig. 7.

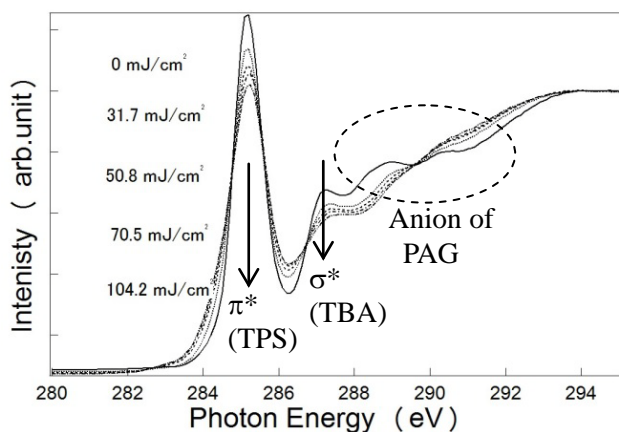


Fig. 2 SR absorption spectra carbon 1s core level in resist A.

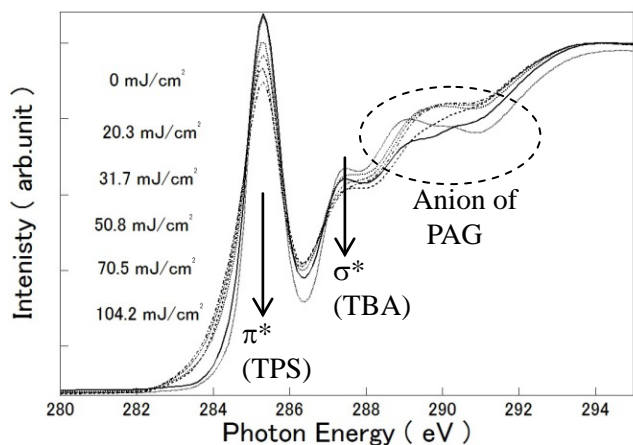


Fig. 3 SR absorption spectra carbon 1s core level in resist B.

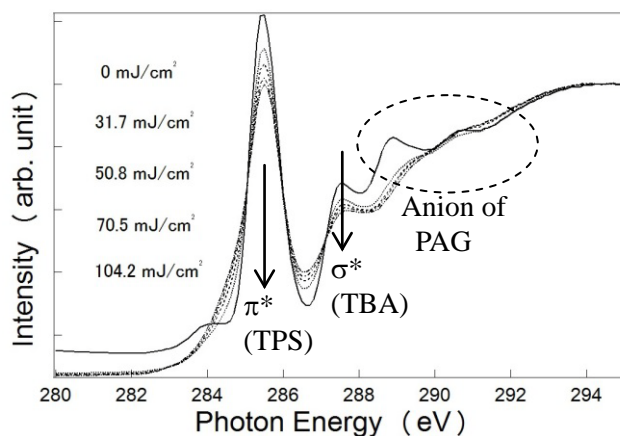


Fig. 4 SR absorption spectra of carbon 1s core level in resist C.

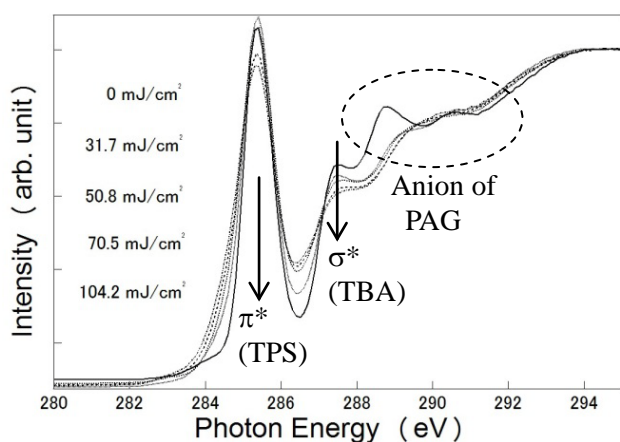


Fig. 5 SR absorption spectra of carbon 1s core level in resist D; (a) 280 eV-330eV, and (b) 285 eV-295 eV.

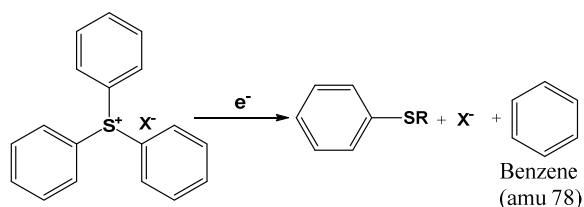


Fig. 6 Decomposition reaction of the triphenylsunfonium employed as the cation of PAG by the secondary electron.

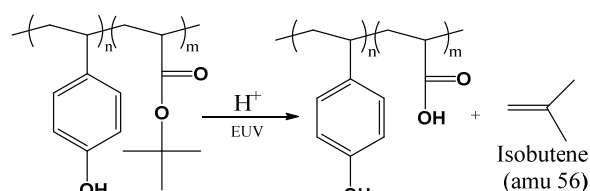


Fig. 7 Decomposition reaction of PHS-TBA.

The absorption spectra of fluorine 1s core level for resists A, B and C were measured by the SR absorption spectroscopic method. Figures 8, 9, and

10 show the EUV exposure dose dependency of the absorption of fluorine 1s core level in resists A, B, and C, respectively. Comparison of Figs 8, 9, and 10, the fluorine of the anion of the PAG in resists A and B decompose easily rather than that of the anion of PAG in resist C.

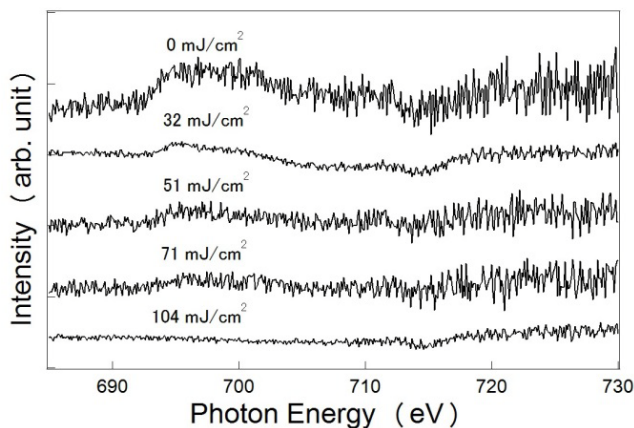


Fig. 8 SR absorption spectra of fluorine 1s core level for resist A.

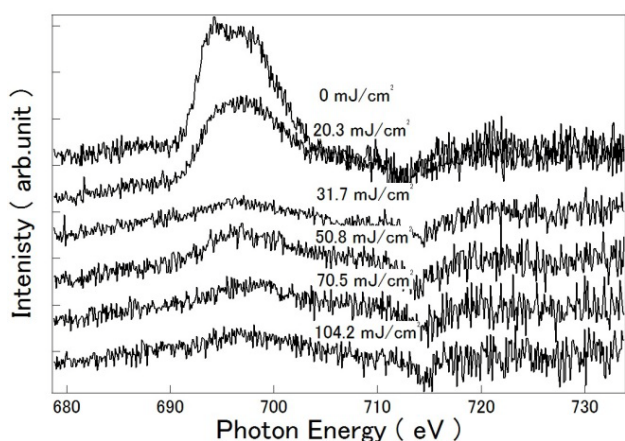


Fig. 9 SR absorption spectra of fluorine 1s core level for resist B.

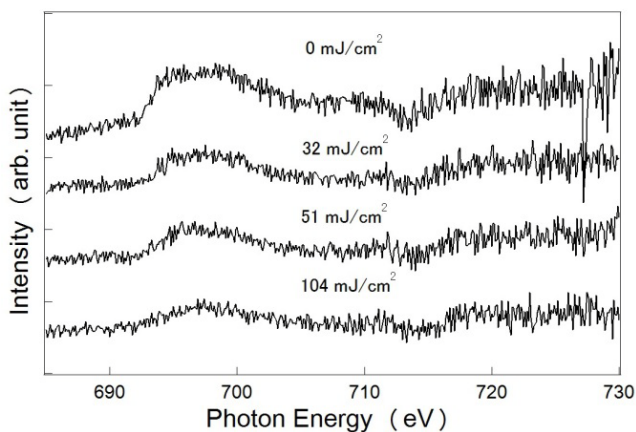


Fig. 10 SR absorption spectra of fluorine 1s core level for resist C.

As the results, the resist including imidate type in the anion of PAG which is easy to decompose in EUV irradiation has higher sensitivity rather than others. On the other hand, for TPS-Cs, there is not changes in the oxygen 1s core spectra as increasing EUV exposure dose. Thus as the anion of TPS-Cs is very stable, resist including TPS-Cs has lowest sensitivity.

In addition, to control the line edge roughness, generally shortening the acid diffusion in chemically amplified resist during PEB might be beneficial by increasing the molecular size of the anion of PAG. However, if the decomposition reaction of the anion of PAG in EUV irradiation is occurred strongly, the acid diffusion length might become large. Thus, the simultaneous achievement of the high sensitive and the shortening LWR, the anion decomposition reaction based on the direct excitation of PAG should be considered and analyzed.

Figure 11 shows two scheme of the decomposition reaction of the Imidate type PAG reaction under EUV irradiation. In Fig. 11(a), R Ph, and X⁻ indicate the base polymer such as PHS polymer, the benzyl group of the cation of PAG, and the anion of PAG, respectively. In Fig. 10(b), X⁻ is the anion of PAG, and X₁⁻, X₂⁻, and X₃⁻ are decomposition species from the anion of X⁻ which has a negative charge. N₁, N₂, and N₃ are decomposition component which have a neutral charge. The dominant chemical reaction of the EUV light is ionization and the cation of the PAG decomposes by secondary electron as shown in Fig. 11(a).

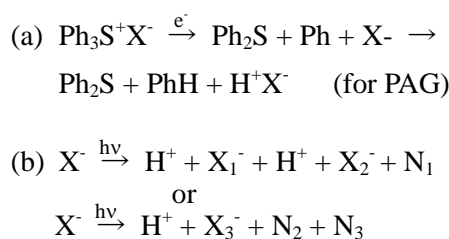


Fig. 11 (a) The decomposition reaction by the secondary electron generated from the ionization reaction and (b) the decomposition reaction of the anion of PAG by the direct excitation reaction under EUV irradiation.

For the decomposition reaction of the anion of PAG, it seems to not occur by the secondary electron. In the case of Imidate of PAG, the anion of PAG decomposes by the direct excitation of PAG as shown in Fig. 11(b). Therefore, the EUV

sensitivity of the model resists which contain Imidate as the anion of PAGs are higher than that contains Nonaflate and Cs as the anion of PAGs.

Therefore, the low sensitivity of the model resist contains TPS-Cs depends on the stable chemical structure of the anion of PAG. Otherwise, the high sensitivity of the model resist contains TPS-Imidate-1 and TPS-Imidate-2 depend on the decomposition reaction of the anion of PAG.

4. Conclusions

The chemical reaction in EUV irradiation of the several photoacid generators (PAGs) which employed triphenylsulfonium (TPS) salts as the cation of PAG, is discussed on the basis of the analysis using the SR absorption spectroscopy in the soft x-ray region. The fluorine atoms of the anion PAGs which have the chemical structure of the imidate type such as TPS-Imidate-1, and TPS-Imidate-2 strongly decomposed under EUV exposure. In the case of these PAG type, it is found that in addition to the ionization reaction, the anion decomposition reaction originated by the photo excitation of the photoacid generator might occur under EUV exposures. Thus the sensitivity seemed to be high comparison to tri-phenylsulfonium perfluorobutanesulfonate (TPS-Nonaflate) under EUV exposure. In the case of tri-phenylsulfonium camphorsulfonate (TPS-Cs), the anion which does not contain fluorine seemed to be very stable under EUV exposure and the sensitivity is lower than TPS-Nonaflate.

The SR absorption spectroscopy is a powerful analysis method to analyze the decomposition reaction of the anion of PAG. To satisfy the specification of the EUV resist which require for high volume manufacturing, all the chemical reaction should be taken in account, such as the ionization and the direct excitation reactions. Increasing the sensitivity, it might have more space to achieve the low LWR resist.

References

1. H. Kinoshita, K. Kurihara, Y. Ishii and Y. Torii, *J. Vac. Sci. & Technol.*, **B7** (1989) 1648.
2. International Technology Roadmap for Semiconductors 2011 Edition.
3. H. Ito, C. G. Willson, and J. M. J. Frechet, *Digest of Tech. Papers 1982 Symp. VLSI Tech.*, (1982) 86.
4. H. Ito and C. G. Willson, *Polym. Eng. Sci.*, **23** (1983) 1012.
5. H. Ito, G. Breyta, D. Hofer, R. Sooriyakumaran, K. Petrillo, and D. Seeger, *J. Photopolym. Sci. Technol.*, **7** (1994) 433.
6. J. W. Thackeray, R. A. Nassar, K. Spear-Alfonso, T. Wallow, B LaFontaine, *J. Photopolym. Sci. Technol.*, **19** (2006) 525.
7. D. C. Tully, A. R. Trimble and J. M. J. Frechet, *Adv. Mater.* **12** (2000) 1118.
8. J.B. Kim, H. J. Yun and Y.-G. Kwon, *Chem. Lett.*, **10** (2002), 1064.
9. M. Ishida, J. Fujita, T. Ogura, Y. Ochiai, E. Ohshima and J. Momoda: *Jpn. J. Appl. Phys.*, **42** (2003) 3913.
10. T. Kadota, M. Yoshiiwa, H. Kageyama, F. Wakaya, K. Gamo and Y. Shirota, *Proc. SPIE*, **4345** (2001) 891.
11. J. B. Kim, Y.-G. Kwon, T. Fujigaya, Y. Shibasaki and M. Ueda, *J. Mater. Chem.*, **12** (2002) 53.
12. T. Hirayama, D. Shiono, H. Hada and J. Onodera, *J. Photopolym. Sci. Technol.*, **17** (2004) 435.
13. H. Hada, T. Hirayama, D. Shiono, J. Onodera, T. Watanabe, S. Y. Lee and H. Kinoshita, *Jpn. J. Appl. Phys.*, **44** (7B) (2005) 5824.
14. Daiju Shiono, Hideo Hada, Kazufumi Sato, Yasuyuki Fukushima, Takeo Watanabe, and Hiroo Kinoshita, *J. Photopolym. Sci. Technol.*, **22**, (2009) 737.
15. H. Kudo, R. Hayashi, K. Mitani, T. Yokozawa, N. C. Kasuga, and T. Nishikubo, *Angew. Chem. Int. Ed.*, **45**, (2006) 7948.
16. H. Seki, S. Kuwabara, H. Kudo and T. Nishikubo, *Chemistry Letters*, **40**, (2011) 464.
17. Hiroto Kudo, Nobumitsu Niina, Tomoharu Sato, Hiroaki Oizumi, Toshiro Itani, Takuro Miura, Takeo Watanabe and Hiroo Kinoshita, *J. Photopolymer Sci. Technol*, **25** (2012) 587.
18. T. Watanabe, H. Kinoshita, H. Nii, K. Hamamoto, H. Hada, H. Komano, and S. Irie, *J. Vac. Sci. Technol.*, **B19** (2001) 736.
19. K. Hamamoto, T. Watanabe, H. Hada, H. Komano and H. Kinoshita, *J. Photopolym. Sci. Technol.*, **15** (2002) 361.
20. Yasuyuki Fukushima, Naoki Sakagami, Teruhiko Kimura, Yoshito Kamaji, Takafumi Iguchi, Yuya Yamaguchi, Masaki Tada, Tetsuo Harada, Takeo Watanabe, and Hiroo Kinoshita, *Jpn. J. Appl. Phys.*, **49** (2010) 06GD06-1.
21. Takuro Urayama, Takeo Watanabe, Yuya Yamaguchi, Naohiro Matsuda, Yasuyuki Fukushima, Takafumi Iguchi, Tetsuo Harada, and Hiroo Kinoshita, *J. Photopolymer Sci.*

- Technol*, **23** (2011) 681.
22. T. Kozawa, A. Saeki, K. Okamoto and S. Tagawa, 3rd EUVL Symposium 2004.
 23. T. Kozawa, H. Yamamoto, A. Saeki, and S. Tagawa, *J. Vac. Sci. Technol.*, B **23** (2005) 2716.
 24. T. Watanabe, K. Hamamoto, H. Kinoshita, H. Hada and H. Komano, *Jpn. J. Appl. Phys.*, **43** (2004) 3713.
 25. H. Hada, T. Watanabe, H. Kinoshita and H. Komano, *J. Photopolym. Sci. Technol.*, **18** (2005) 475.
 26. T. Watanabe, H. Hada, S. Y. Lee, H. Kinoshita, K. Hamamoto and H. Komano *Jpn. J. Appl. Phys.*, **44** (2005) 5866.
 27. T. Watanabe, Y. Haruyama, D. Shiono, K. Emura, T. Urayama, T. Harada, and H. Kinoshita, *J. Photopolymer Sci. Technol.*, **25** (2012) 569.
 28. T. Watanabe, H. Hada, H. Kinoshita, Y. Tanaka, H. Shiotani, Y. Fukushima and H. Komano: *Proc. SPIE*, **6153** (2006) 615343-1.
 29. T. Watanabe, H. Hada, Y. Fukushima, H. Shiotani, H. Kinoshita and H. Komano, *Synchrotron Radiation Instrumentation: Ninth International Conference*, AIP **879** (2007) 1470.
 30. Gaussian03 electron orbital calculation software is informed in URL:<http://www.gaussian.com/home>.
 31. S. Hashimoto, A. Ando, S. Amano, Y. Haruyama, T. Hattori, K. Kanda, H. Kinoshita, S. Matsui, H. Mekar, S. Miyamoto, T. Mochizuki, M. Niibe, Y. Shoji, Y. Utsumi, T. Watanabe and H. Tsubakino, *Trans. Mater. Res. Soc. Jpn.*, **26** (2001) 783.
 32. T. Watanabe, Y. Haruyama, D. Shiono, K. Emura, T. Urayama, T. Harada, and H. Kinoshita, *J. Photopolymer Sci. Technol.*, **25** (2012) 569.

Phase defect characterization on an extreme-ultraviolet blank mask using micro coherent extreme-ultraviolet scatterometry microscope

Tetsuo Harada, Yusuke Tanaka, Takeo Watanabe, Hiroo Kinoshita
Center for EUV Lithography, LAST, University of Hyogo, Kamigori, Hyogo 678-1205, Japan

Abstract

Defect-free mask production is a critical issue in extreme-ultraviolet (EUV) lithography. On EUV masks, phase defects are buried by multilayer coating, which is a serious EUV-specific issue. These defects should be hidden or be compensated completely by the absorber pattern for the production of defect-free masks. A phase image of the phase defects at the EUV lithography exposure wavelength is essential to characterize the defects. For characterization of phase defects, we have developed the micro coherent EUV microscope (micro-CSM). This system is lensless and is based on a coherent diffraction imaging method, which records diffraction images. The intensity and phase images of the defects are reconstructed through iterative calculations. The micro-CSM system has focusing optics of a Fresnel zone plate to observe small defect. The detection size limits of the phase defects were a width of 25 nm and a depth of 1.4 nm. Diffraction images from an asymmetric phase defect were related well to the defect shapes and volumes. The defect position was also inspected by mapping image that was measured using by step-and-repeat observation. The actinic defect signals were observed by the micro-CSM system.

Introduction

In extreme-ultraviolet (EUV) lithography, defect-free mask production is a critical issue for high-volume manufacturing of semiconductor devices. The mask is a master pattern for manufacture of a semiconductor device, and there must be no defects on this mask. The EUV mask is a reflective-type mask, unlike the transparent-type mask that is used for conventional 193 nm lithography. The EUV mask is coated with a Mo/Si multilayer followed by an absorber layer, in which patterns are printed to form the device pattern. However, phase structures such as bumps or pits on the substrate or particles in the multilayer can form printable defects in EUV exposure tools. For example, a shallow structure of 1 nm depth on the surface of a mask substrate can cause a large reflection phase shift of 53° at the 13.5-nm EUV wavelength. As a result, this buried defect is printable. The printability has been evaluated by some groups using EUV actinic microscopes. Buried defects can be detected efficiently at the mask blank state of manufacture.

We have developed a coherent EUV scatterometry microscope for phase defect characterization.[1–5] The sample phase defect was exposed using coherent EUV light, and the diffracted light was recorded using a CCD camera. To reconstruct the pattern image, the phase information of the diffraction image is required, but this information is not recorded. We use a coherent diffraction imaging (CDI) method[6-8] to retrieve the missing phase. With coherent illumination, the phase is embedded in the oversampled diffraction image. This phase information is then retrieved via iterative calculations using Fourier transforms and inverse Fourier transforms. The periodic structures of the line-and-space (L/S) and hole patterns and the aperiodic structures were reconstructed well.[2] In addition to the conventional intensity images, the phase images were also acquired by the CSM.[5] The EUV-phase shift value of an absorber structure and the phase difference in the L/S pattern with shadowing effects were evaluated, because they could cause actinic critical-dimension changes. The phase distribution of a 1 μm square-sized phase defect was also reconstructed, from which the phase value was quantitatively evaluated.[5] This EUV-phase distribution is the basic information required to predict defect printability at the EUV exposure tools. Because the defect shape on a glass substrate is different to the defect shape on a multilayer surface, the conventional atomic force microscope (AFM) tool cannot be used to evaluate the printability.

The illumination spot size of the CSM system was about 5 μm , which is too large for evaluation of a target defect that is less than 50 nm wide and 1 nm high. Therefore, the defect signal was much weaker than the background signals. The sources of these background signals were the CCD camera noise and scattering from the mask. The scattering noise problem in this system is an intrinsic problem, which cannot be avoided. For example, high

EUV illumination flux or even an ideal detector cannot improve the detection limit. Thus, we proposed the micro-CSM system with a focused illumination probe, which has a probe size of several hundred nm.[10] The phase distributions of small defects (< 50 nm wide, < 1 nm high) will be evaluated by the CDI method using the micro-CSM system. It is difficult to characterize such small defects using conventional EUV microscopes with objective lenses. Because the micro-CSM is a lensless system, the diffraction image is aberration-free and allows us to characterize the defect accurately. In this paper, we show preliminary results of the micro-CSM, which includes observation result of various phase defects.

Experiments and Results

Defect-free mask production is a critical issue in extreme-ultraviolet (EUV) lithography. On EUV masks, phase defects are buried by multilayer coating, which is a serious EUV-specific issue. These defects should be hidden or be compensated completely by the absorber pattern for the production of defect-free masks. A phase image of the phase defects at the EUV lithography exposure wavelength is essential to characterize the defects. For characterization of phase defects, we have developed the micro coherent EUV microscope (micro-CSM). This system is lensless and is based on a coherent diffraction imaging method, which records diffraction images. The intensity and phase images of the defects are reconstructed through iterative calculations. The micro-CSM system has focusing optics of a Fresnel zone plate to observe small defect. The detection size limits of the phase defects were a width of 25 nm and a depth of 1.4 nm. Diffraction images from an asymmetric phase defect were related well to the defect shapes and volumes. The defect position was also A schematic view of the micro-CSM system is shown in Fig. 1. The coherent EUV illumination is focused on the mask by a Fresnel zone plate (FZP). Diffraction from defects is recorded directly by a CCD camera. The focusing layout of the FZP is off-axis to use the reflection signal, and has a window that enables it to accept reflected EUV light.

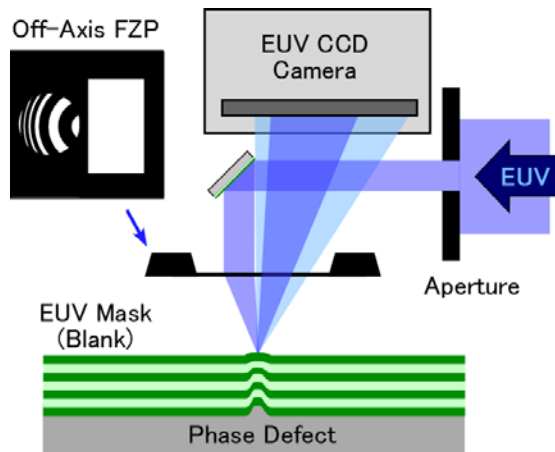


Figure 1. Schematic view of micro-CSM system. The EUV illumination light is focused by the off-axis FZP. Diffraction from defects is recorded directly by the CCD camera.

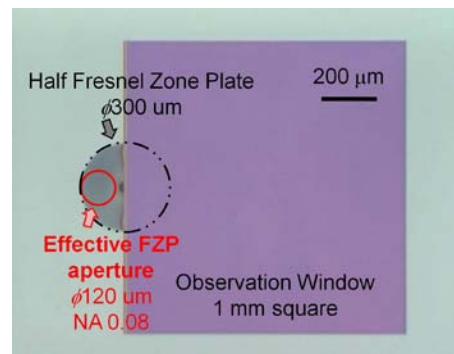


Figure 2. Optical microscope image of the FZP. The half FZP is patterned on the SiC membrane. The focal length is $750\ \mu\text{m}$. This was taken by the sample side.

Figure 2 shows an optical microscope image of the FZP that was fabricated by NTT Advanced Technology Corporation. The designed focal length is approximately $750\ \mu\text{m}$. The diameter of the original on-axis FZP is approximately $300\ \mu\text{m}$. Half of the FZP region was patterned on the membrane. A circular region of $120\ \mu\text{m}$ in diameter, indicated as a bold line, is used to focus the EUV illumination, which is equivalent to an effective numerical aperture of 0.08. The expected focusing size determined by the NA is approximately 100 nm. The support membrane is made from 200 nm-thick SiC. The absorber material is 100 nm-thick Ta. The narrowest line width at the outermost FZP region is approximately 34 nm. A $1\ \mu\text{m}$ square rectangular window was also patterned to accept the reflected EUV rays. The angle of incidence of the main focused EUV ray is approximately 6.8° , which is near the angle of the EUV scanner.

The micro-CSM system is located on beamline 10 of the NewSUBARU synchrotron radiation facility[26,27]. The entrance slit design is slitless. The monochromator type is that described by Hettrick and Underwood[29] in which the mechanically ruled, plane varied-line-space grating operating the converging light produced by a concave spherical mirror. The spectral resolution is approximately 1300 at the EUV wavelength 13.5 nm. The exit slit is relayed up to 5.2 m downstream at unity magnification by a vertical refocusing mirror, where the focusing size is approximately $0.05 \times 0.8\ \text{mm}^2$. A $400\ \mu\text{m}$ -diameter pinhole was inserted at the refocusing

position to improve the spatial coherence. The FZP in the micro-CSM system was located 2.1 m downstream from the pinhole.

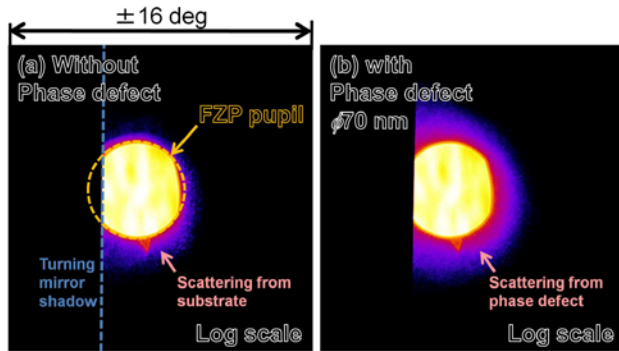


Figure 3. CCD camera images from the micro-CSM system. The sample was a programmed-defect mask. The intensity is shown in log scale. Direct reflection of the focused EUV (by the FZP pupil) and diffraction (scattering) were recorded. The observation positions were on (a) the no-defect region and (b) a 70 nm-wide defect.

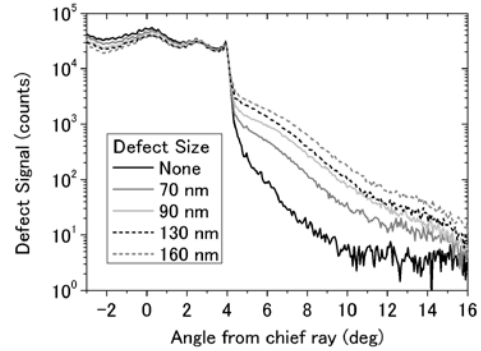


Figure 4. The signal profile of a phase defect with variable width. The horizontal axis indicates the angle from the chief ray of the focusing EUV.

The diffraction signal from a defect is recorded using a back-illuminated CCD camera (Roper Scientific MTE-2048B). This camera can operate in a high-vacuum environment, and is cooled to a temperature of -50°C . The CCD surface is placed parallel to the mask surface. The imaging area is $27.6 \times 27.6 \text{ mm}^2$, and contains 2048×2048 arrays of imaging pixels with areas of $13.5 \times 13.5 \text{ } \mu\text{m}^2$. The CCD chip is located parallel to the mask, and the distance from chip to mask is approximately 50 mm. Therefore, the numerical aperture of the micro-CSM system is approximately 0.28. The acceptance angle of the main ray is $\pm 16^{\circ}$. The estimated spatial resolution is 30 nm at half pitch. The sample mask was a blank EUV mask containing programmed bump structures on a glass substrate. The bumps were located with about $10 \text{ } \mu\text{m}$ pitch. The designed bump height was 7 nm, while the bump width was varied in a range from 70 to 420 nm, and the bumps were square in shape.

Figure 3 shows the observation results for the programmed defect mask, which are diffraction images recorded by the CCD camera. Figure 3(a) shows an area without a defect, and (b) shows an area with a 70 nm-wide defect. The image intensity is shown in log scale in both cases. The exposure time was 10 s. The CCD pixels were binned 4×4 to a pixel, and the array count of the CCD chip was 512×512 . The bright signal of the center region is caused by the direct reflection of the focused beam, which corresponds to the FZP pupil. The signal had approximately 40,000 counts in the pupil. The lack of signal on the left side of the pupil is caused by the shadow of the folding mirror. The strong diffraction signal from the defect was recorded around the pupil shown in Fig. 3(b), where the signal was 10 times stronger than that without a defect. Figure 4 shows the signal profiles of phase defects with varied widths of 70, 90, 130, and 160 nm. The vertical axis indicates the detector intensity, and the horizontal axis indicates the angle from the chief ray. The diffraction signal increased with increasing defect width. The pupil signal decreased with increasing defect width, which was caused by the destructive interference of the defects. The defect signal decreased with increasing diffraction angle; the signal from a 70-nm-wide defect was the same as that without any defect at around 16° . The diffraction signal without any defects was not zero between 4° and 10° , because of the scattering signal caused by the mask roughness. This signal is the background signal of the micro-CSM system, which determines the defect size detection limit. This background signal did not depend on the illumination size. However, the diffraction signal from the defects depended on the illumination size. Thus, the position of the focus is very important for the micro-CSM system, which changes the illumination size. The distance from the FZP to the mask is measured by a capacitive sensor, and the best focus position was once evaluated using the 70 nm defect to maximize the defect signal.

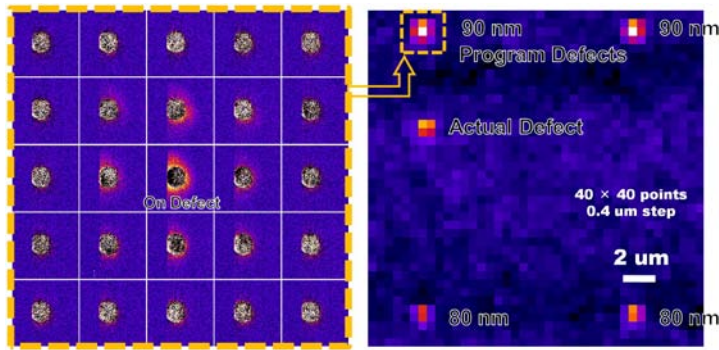


Figure 5. Mapping image of the diffraction intensity with step-and-repeat measurements. The diffraction images are shown in the left figure as differences from the diffraction image at the no-defect position. The intensity of each pixel in the right figure shows the integral diffraction signal of the diffraction images. The programmed defects and actual phase defect were clearly observed.

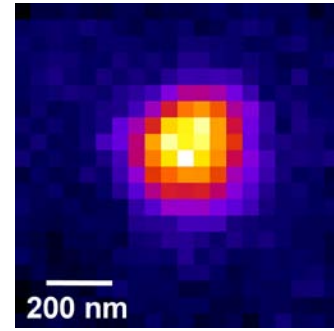


Figure 6. Mapping diffraction image of a 70 nm-wide phase defect. The focus size of the EUV illumination was estimated to be 230 nm (FWHM).

For defect position inspection, we perform mapping measurements of the diffraction image, which are composed of step-and-repeat observations in both the X and Y directions. A 40×40 pixel mapping image is shown in Fig. 5. The diffraction images on the left were recorded with step distances of 400 nm, with movements performed by the piezo stage, and are shown as differences from the diffraction image of no-defect position. The center image is located on the defect. Each pixel of the figure on the right shows the integral diffraction signal. The diffraction images on the left correspond to the rectangular region indicated by the dashed line, which is the diffraction intensity around the 90-nm-wide programmed defect. The right-hand part of Fig. 5 includes 40×40 pixels of the $16 \times 16 \mu\text{m}^2$ region. In this measurement, the 400- μm -diameter pinhole at the beamline refocusing position was not used to increase the illumination size and intensity. The exposure time for each observation was very short at 0.1 s, which indicates strong illumination intensity. In the mapping image, there were four programmed defects: two 90-nm-wide defects and two 80-nm-wide defects. All defect positions were clearly inspected during the mapping measurement. In addition to the programmed defects, there was also a diffraction signal from an actual defect. We measured the actual defect on the multilayer surface by AFM, which showed that the defect was 90 nm wide and 2.2 nm high. This AFM result indicates that the defect is a phase-type defect, because the defect volume is small. The micro-CSM system detected both the programmed defect and the actual phase defect.

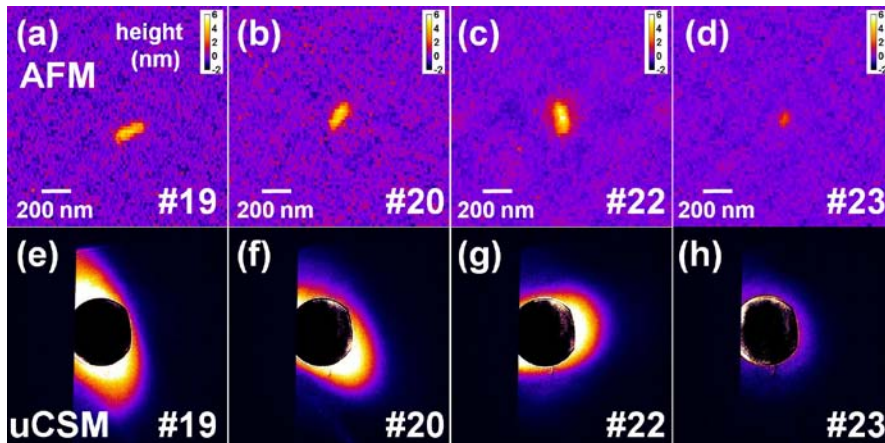


Figure 7. The observation results of the asymmetrically-shaped phase defects. (a)-(d) show the AFM results, and (e)-(h) show the micro-CSM diffraction images of the same defects.

We observed a 70-nm-wide defect by mapping measurements around a best-focus position. The mapping image at the best focus position is shown in Fig. 6, where the illumination size is minimized. The step distance was 50 nm, and the exposure time was 0.5 s. Because the defect width was much smaller than the illumination size, this image shows the illumination profile. The focused profile is almost circular, and was well focused. The scattering signal profile had a full width at half maximum (FWHM) of 250 nm. The illumination size was 230 nm, as evaluated by deconvolution of the defect width measured by AFM. In this deconvolution, the illumination profile and the defect profile were estimated to have Gaussian shapes. The

measured illumination size was 2 times larger than the size expected for the NA of 0.08. We will improve the FZP focusing conditions in future work to minimize the illumination size, which will then enlarge the defect signal.

Figure 7 shows the diffraction images of asymmetrically-shaped phase defects. Figure 7(a)-(d) show the AFM results, and Fig. 7(e)-(h) show the micro-CSM results for the same defects. Defects #19, #20, and #22 had oval shapes where the ratio of the long and the short axes was about 1:2. Defect #23 was the smallest phase defect on this programmed mask and was 60 nm wide and 2.2 nm high. The micro-CSM images were shown as differences from the diffraction image at a no-defect position. The diffraction signals of the oval defects had asymmetric diffraction, where the major axis corresponded perfectly to the minor axis of the AFM result. The diffraction signal is reciprocal space information of the defect. Therefore, the diffraction distribution of the micro-CSM system corresponds to the defect shapes. At the smallest defect, #23, the diffraction signal was also very small, and this was related to the phase defect volume. Thus, the micro-CSM measured both defect shape and defect volume. Because the diffraction orientation would be strongly dependent on the defect shape, the printability of the defect is also dependent on the defect shape.

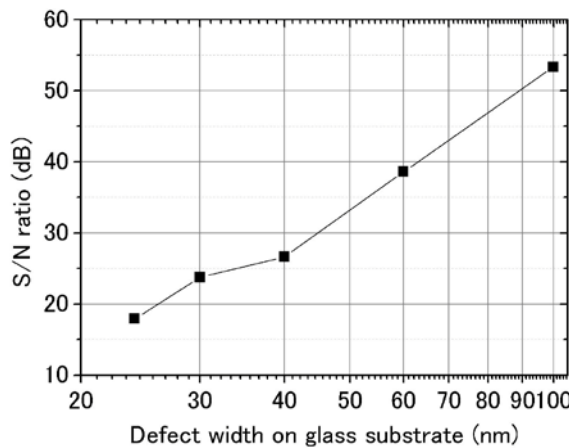


Figure 8. S/N ratio of the defect signal and background noise caused by scattering from the substrate.

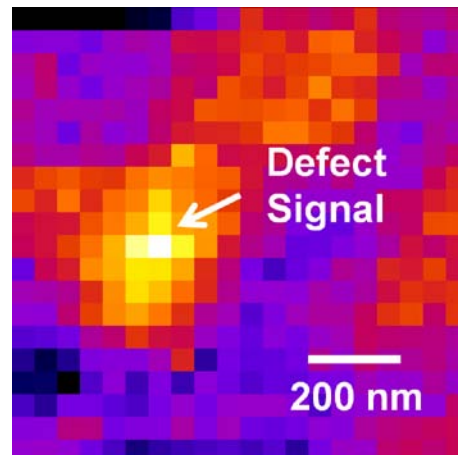


Figure 9. Mapping diffraction image of the smallest detectable defect with width of 25 nm and height of 1.4 nm on the glass

To evaluate the size detection limit of the micro-CSM, we observed another programmed phase defect mask. The mask had programmed pit structures on the glass substrate. The designed defect size range and depth were 10 – 400 nm and 1 nm, respectively. We performed mapping measurements around the pit defects with 50 nm step distances, exposure times of 5 s, and 10×10 measurement points. Figure 8 shows the S/N ratio for each defect size. The horizontal axis indicates the defect width on the glass substrate as measured by AFM, which was completely different to that on the multilayer surface. The vertical axis indicates the S/N ratio of the defect signal and noise. Noise in this case means the standard deviation that was evaluated from the signal fluctuation of the no-defect region. The size detection limits for the phase defect were 25 nm in width and 1.4 nm in height. The mapping image of the smallest detectable defect is shown in Fig. 9. The diffraction signal of this defect was clearly observed. The integral intensity of the diffraction on the no-defect region fluctuated, and this determines the noise level.

The micro-CSM system with FZP focusing optics was developed to characterize defects on EUV masks, with a focusing size of approximately 230 nm in diameter. The micro-CSM is a lensless system; the diffraction signals from defects are recorded directly with a CCD camera. The phase defect size detection limits were approximately 25 nm in width and 1.4 nm in depth. An actual phase defect with a width of 90 nm and a height of 2.2 nm was also detected. The diffraction image was related to both the defect volume and the defect shape. The actinic defect printability can be estimated from the diffraction image without any optical aberrations. At the oval phase defects, the defect orientation corresponded perfectly with the diffraction image. The defect position was also inspected via mapping image measurements composed of step-and-repeat observations.

ACKNOWLEDGMENTS

This work is re-contracted research from the EUVL Infrastructure Development Center (EIDEC). EIDEC programs are supported by the New Energy and Industrial Technology Development Organization (NEDO).

References

- [1] T. Harada, J. Kishimoto, T. Watanabe, H. Kinoshita, and D. G. Lee, *J. Vac. Sci. Technol. B* 27, 3203 (2009).
- [2] T. Harada, M. Nakasuji, T. Kimura, T. Watanabe, H. Kinoshita, and Y. Nagata, *J. Vac. Sci. Technol. B* 29, 06F503 (2011).
- [3] M. Nakasuji, A. Tokimasa, T. Harada, Y. Nagata, T. Watanabe, K. Midorikawa, and H. Kinoshita, *Jpn. J. Appl. Phys.* 51, 06FB09 (2012).
- [4] T. Harada, M. Nakasuji, T. Kimura, Y. Nagata, T. Watanabe, and H. Kinoshita, *Proc. SPIE* 8081, 80810K (2011).
- [5] T. Harada, M. Nakasuji, Y. Nagata, T. Watanabe, and H. Kinoshita, *Jpn. J. Appl. Phys.* 52, 06GB02, 2013.
- [6] J. Miao, D. Sayre, and H. N. Chapman, *J. Opt. Soc. Am. A* 15, 1662 (1998).
- [7] Y. Takahashi, A. Suzuki, N. Zettsu, Y. Kohmura, Y. Senba, H. Ohashi, K. Ymauchi, and T. Ishikawa, *Phys. Rev. B* 83, 214109 (2011).
- [8] J. M. Rodenburg and H. M. L. Faulkner, *Appl. Phys. Lett.* 85, 4795 (2004).
- [9] M. Maiden and J. M. Rodenburg, *Ultramicroscopy* 109, 1256 (2009).
- [10] T. Harada, M. Nakasuji, A. Tokimasa, T. Watanabe, Y. Usui, and H. Kinoshita, *Jpn. J. Appl. Phys.* 51, 06FB08 (2012).

Low-Temperature Activation of Boron in B₁₀H₁₄-doped Si wafer by Soft X-ray Irradiation

Akira Heya¹, Shota Hirano¹, Fumito Kusakabe¹, Naoto Matsuo¹, Kazuhiro Kanda²

¹ University of Hyogo, 2167 Shosha, Himeji, Hyogo 671-2280, Japan

Phone: +81-79-267-4909 E-mail: heya@eng.u-hyogo.ac.jp

² LASTI, University of Hyogo, 3-1-2 Koto, Kamigori, Hyogo 678-1205, Japan

Abstract

Novel activation method of B dopant in Si wafer using a soft X-ray undulator was investigated. As the photon energy closed with the energy of the core level of Si 2p, the activation was enhanced. The sheet resistance of soft X-ray irradiated sample was low in comparison with that of annealed sample. The low sheet resistance of 60 Ω/sq was obtained using a mixture of B₁₀H₁₄⁺ cluster and soft X-ray irradiation even at temperatures as low as 500 °C. The B activation occurred by the atomic migration of Si atoms due to the composition of lattice vibration and Coulomb force via the electron excitation.

Introduction

Low-temperature activation is required for the fabrication of an ultra-shallow junction below 10 nm. A novel activation method of B dopant using a soft X-ray undulator at low temperature was developed [1]. The cluster-ion beam is expected to realize the ultra-shallow doping because the energy a dopant atom is low. In this study, we tried to obtain the low-sheet resistance using B₁₀H₁₄⁺ cluster as a B source. The photon energy dependence of sheet resistance and the mechanism of soft X-ray activation was discussed in comparison with a thermal activation.

Experimental

B ion clusters (B₁₀H₁₄⁺) were implanted to Si (100) wafer (n-type, 10-25 Ωcm) with an energy of 47.8 keV and a dose of 6×10¹⁵ cm⁻² (0° tilt).

The irradiation of soft X-ray was carried out at BL07A of NewSUBARU (Fig. 1). The storage-ring energy and storage-ring current were 1 GeV and 300mA, respectively. The photon energy was changed from 50 to 250 eV, with the dose quantity of 50 mA h. The irradiation time was 600 s. The pressure during irradiation was 6×10⁻⁵ Pa. A part of sample was cooled using Cu holder with refrigerant of -20°C. The surface temperature of Si wafer was measured via a ZnSe window by a pyrometer. The emissivity was 0.6. For the comparison, the annealing in N₂ atmosphere was carried out in the 100 - 800°C range for 900 s.

The sheet resistance was measured by a four-point probe method at room temperature. In this study, correction factor of the four-point probe method was not used. The activation ratio is given by Irvin curve and implantation dose.

Results and discussion

The temperature and the sheet resistance of Si wafer as a function of photon energy are shown in Figs. 2 and 3, respectively. The temperature at the photon energy of 100 eV, which corresponds to the energy level of Si 2p core-electron (99.8 eV), shows the highest value. The Si 2p core-electrons are excited by soft X-ray irradiation and they relax resulting in a temperature increase. The activation was enhanced around 100 eV. According to Fermi golden rule, the electron excitation is enhanced by closing with the energy of core level. It is found that the sheet resistance after soft X-ray irradiation strongly depended on the irradiated photon energy. In the case of cooled sample, the sheet resistance was decreased from 880 to 430 Ω/sq after soft X-ray irradiation. It is found that the sheet resistance depend on not only thermal effect but also soft X-ray effect. It is considered that the dopant activation was enhanced by the electron excitation in core energy level during the soft X-ray irradiation.

The relationship between the sheet resistance and the treatment temperature is shown in Fig. 4. The sheet resistance of soft X-ray irradiated Si was lower than that of annealed Si. The tendency was as same as B⁺-doped Si wafer [2]. The sheet resistance for B₁₀H₁₄⁺ implant was low compared with B⁺ implant at treatment temperature around 500°C. The sheet resistance was reduced from 410 to 60 Ω/sq by using B₁₀H₁₄⁺ instead of B⁺.

Under this condition, the activation ratio is estimated to 36 %. Although the dose of $B_{10}H_{14}^+$ implantation is only three times larger than B^+ implantation, the sheet resistance was decreased to one sixth. It is considered that the amorphization during implantation is enhanced by using $B_{10}H_{14}^+$. Therefore, the repair of ion implant damage within Si is easy to occur in comparison with B^+ implantation.

Conclusions

- 1) The activation of B dopant depends on photon energy because the B activation is enhanced by electron excitation and atomic movement.
- 2) The low sheet resistance of 60 Ω/sq was obtained using $B_{10}H_{14}^+$ cluster and soft X-ray irradiation even at temperatures as low as 500 °C. The soft X-ray activation occurs by not only the thermal effect but also the excitation of the core electrons followed by the atomic migration.

Acknowledgments

The authors are grateful to Dr. M. Tanjo of Nissin Ion Equipment Co. Ltd. for supply of the $B_{10}H_{14}^+$ -doped Si wafer and comments.

References

- [1] T. Fukuoka, A. Heya, N. Matsuo, K. Kanda and T. Noguchi: Extended Abstracts of the 2011 International Conference on Solid State Devices and Materials, pp.40-41 (2011).
- [2] A. Heya, N. Matsuo, K. Kanda and T. Noguchi: 2014 International Workshop on Junction Technology (IWJT) Extended Abstracts, pp.23-26 (2014).

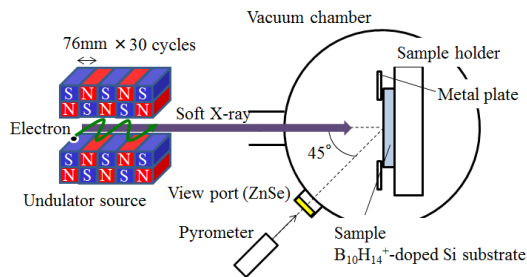


Fig. 1. A schematic diagram of soft X-ray activation apparatus and setup for measuring the sample temperature using a pyrometer. Soft X-ray is generated from a 2.28m-undulator at BL07A.

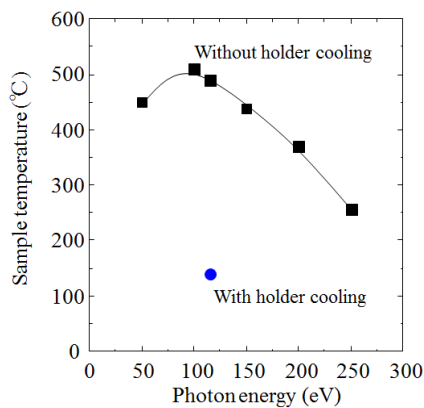


Fig. 2. Maximum sample temperature of $B_{10}H_{14}^+$ -doped Si wafer during irradiation as a function of photon energy of soft X-ray. A part of sample was cooled by refrigerant.

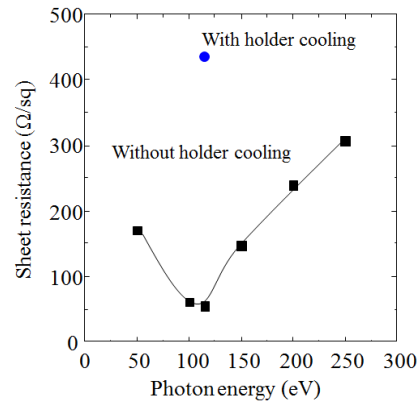


Fig. 3. Sheet resistance of $B_{10}H_{14}^+$ -doped Si wafer after soft X-ray irradiation as a function of photon energy of soft X-ray.

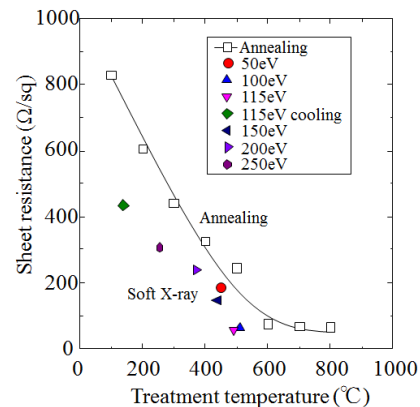


Fig. 4. Sheet resistance as a function of treatment temperature for $B_{10}H_{14}^+$ -doped Si wafer. Open symbols show the annealed sample.

Two Modified Layers in the surface of Silica-Based Films by Undurator Radiation

K. Moriwaki, H.Umeji, Graduate School of Eng., Kobe Univ.,
K.Kanda, and S.Matsui, LASTI/Univ. Hyogo

Abstract

Undurator radiation (UR) by the NewSUBARU is used to modify the surface in silica-based films for optical waveguide devices. It is found that the modifications are different between surface thin layers and inner layers for the samples irradiated by UR with the 1st peak energy ranging from 20 to 110eV. The thin layers with less than 5 nm thickness from the surface show strong reduction for both thermally-grown SiO₂ and synthetic silica glass by analyzing XPS (X-ray Photoelectron Spectroscopy) results. Amounts of the surface reduction show a clear dependence on the peak-energy of UR. Refractive index measurements before and after etching the surface reduction layers reveal that the higher refractive-index changes on the surface are mainly due to the surface reduction layer, and relatively lower refractive-index is also induced in the inner layer under the reduction layer.

Introduction

We use synchrotron radiation (SR) and undurator radiation (UR) for radiation-induced refractive-index changes in silica-based glass for optical devices^{1,2}. Our main objectives are to induce large refractive-index changes more effectively using SR or UR without a spectrometer, and to investigate their origins depending on wavelengths of SR or UR spectra. Especially, UR would be a very useful tool for the materials modifications, because it can select a useful wavelength and has very high intensity. For those reasons we mainly use UR for the present modification experiments. In this report, we investigate the modification effects on the surface of silica-based glasses irradiated with UR.

Experiments and Results

Experimental conditions are almost the same as in the previous experiments^{1,2}. UR (from the NewSUBARU BL-7A) was mainly used to investigate irradiation-wavelength effects. The electron energy of the SR was 1GeV. The UR with the first peak energy ranging from 20 to 110eV was used. The samples were thermally grown SiO₂ films (0.5 μm thickness) on Si substrates or pure synthetic silica-glass. XPS measurements including in-situ etching were used to investigate the surface modification effects and depth profiles for the modification. Refractive index was measured by spectroscopic ellipsometry before and after etching the surface layer. Optical absorption spectroscopy was also used for analyzing irradiation defects and thereby the cause of the refractive index changes.

It is shown in Fig.1 that Si-Si bonds are generated on the surface of thermally-grown SiO₂ films, after irradiating UR with peak energy of 20eV by measuring Si2p peaks in XPS. Figure 1 also shows depth profiles of the S-Si 2p peaks by in-situ etching. From the depth profiles, the Si-Si bond peaks disappear gradually within 5nm thickness, which shows a presence of a very thin reduction layer on the surface. Figure 2 shows that the amounts of the Si-Si bonds are increased by decreasing the UR peak energy from 90

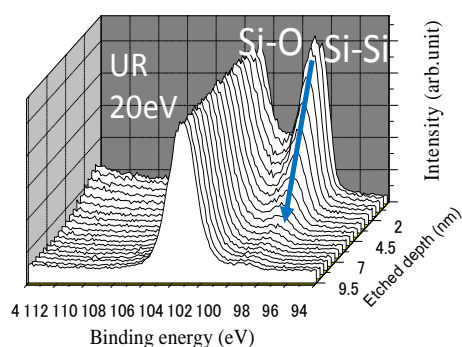


FIG.1. Si 2p XPS spectra with in-situ etching up to a depth of 10nm in thermally-grown SiO₂ films after irradiating UR with a peak energy of 20 eV. The UR dose is 500 mAh.

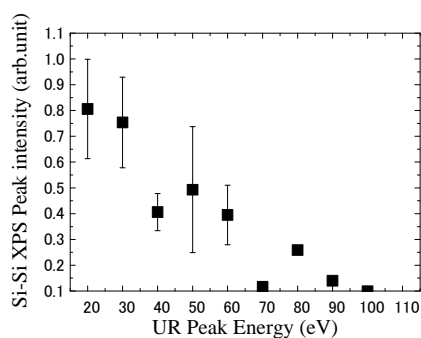


FIG.2. Si-Si bond peak-intensity in the XPS spectra in thermally-grown SiO₂ films as a function of the irradiating UR peak energy. The UR dose is 500mAh.

to 20eV. After irradiating UR with peak energy over 100eV, Si-Si bonds were not found on the samples.

By measuring refractive indices after UR irradiation with peak energies from 20 to 110eV, high refractive-index changes (10^{-2} - 10^{-1}) were found. Figure 3 indicates that there is a correlation between the refractive index and the amounts of Si-Si bonds appeared in Fig.2. The refractive-index changes were increased by decreasing the UR peak energy. Figure 4 shows that the higher refractive-index changes are decreased abruptly by removing the surface reduction layer by 20nm from the surface, while the lower refractive-indices (10^{-2}) remain after the surface etching. The refractive-index changes after the etching were nearly independent of the irradiation peak energy (in Fig.4).

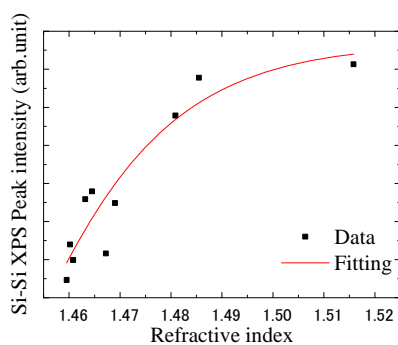


FIG.3. A correlation between the Si-Si bonds peak-intensity and refractive-indices for the samples used in Fig.2 irradiated by UR with a peak energy from 20 to 110eV.

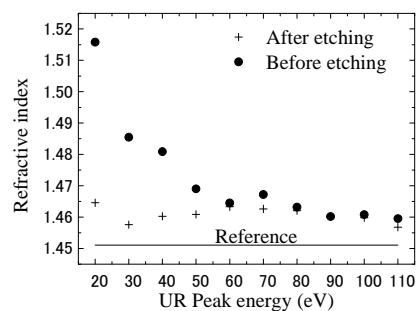


FIG.4. Measured refractive index for thermally-grown SiO_2 films irradiated by UR, and also after etching by 20nm from the surface. The UR dose was 500mAh. The reference indicates that of an initial sample.

Optical absorption spectroscopy revealed that many defects were in the UR-irradiated samples as shown in Fig.5. The surface defects might be caused by breaking of Si-O bonds and following desorption of O atoms. It was also found by the surface etching experiments that the most of the defects in Fig.5 were in the layer shallower than at least 20nm from the surface, while some defects remained after the etching. It is suggested that the remained defects after the etching are a major cause of the refractive-index changes in inner layer under the surface reduction layer.

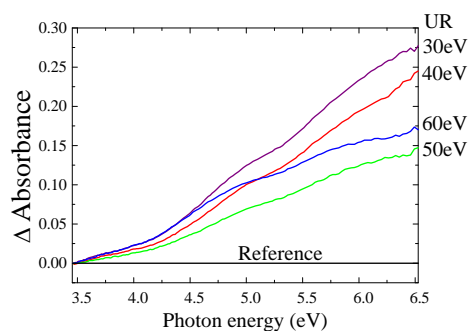


FIG.5. Optical absorbance for silica glass samples irradiated by UR with a peak energy from 30 to 60 eV. The UR dose was 500mAh.

From the results by the ellipsometry and the optical absorption measurements, it is found that the modification layers are separated into two parts of the surface (with less than 5nm thickness) and the inner layer in the samples by UR irradiation (Fig.6).

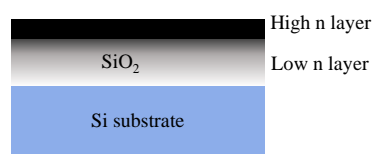


FIG.6. Two modification-layers model irradiated by UR with a peak energy from 20 to 110eV. Each layers show higher (10^{-2} - 10^{-1}) and lower (10^{-2}) refractive-index changes.

Conclusions

Refractive-index changes obtained by UR irradiation in silica-based films were found to be separated into two parts which were a higher refractive-index layer by surface reduction with less than 5nm thickness and relatively lower refractive-index layer by probably some irradiation defects. From our results, the higher refractive-index changes on the surface depended strongly on the irradiated UR peak energy. UR is expected to be a useful irradiation source for modifying materials effectively and controllably.

References

- [1] K.Moriwaki *et al.*, LASTI Annual Report vol.14 (2012).
- [2] K.Moriwaki *et al.*, LASTI Annual Report vol.13 (2011).

Microprocessing using Soft X-ray from Laser Produced Xe Plasma

S. Amano
LASTI/UH

Abstract

Microprocessing of poly(tetrafluoroethylene) (Teflon) and poly(methyl methacrylate) (PMMA) samples was carried out using soft X-ray from a laser produced Xe plasma source we developed. In the Teflon sample, a contact angle of a modified surface with a water drop increased from 90° to 110° to by an irradiation without a mirror and a mask, while the angle decreased to 50° by an irradiation with them. Scanning electron microscopy showed numerous microprotuberances and a masked pattern having micro-concavities on the each sample surface. These suggested that the changes of the contact angle were ascribable to the microstructures of the Teflon surface. We succeeded in controlling the wettability of the Teflon surface from hydrophobic to hydrophilic by microprocessing using the laser plasma X-ray. In the PMMA sample, its etching rate was investigated using an irradiation with a large number of pulses (192000 pulses) and a low power density of $8 \times 10^4 \text{ W/cm}^2$. The etching rate was calculated to be 5 pm/pulse and this was concluded to be a result by only photo-etching without thermal effect. We demonstrated pure photo-etching depth of $\sim 1 \mu\text{m}$.

Laser plasma X-ray is generated from high temperature and high density plasma produced by high intensity laser. This is useful for industrial applications as a compact light source with high intensity comparing to synchrotron radiation sources. In industrial uses of the X-ray, high average power is also required and we developed a laser produced Xe plasma source to satisfy this demand and started to study for microprocessing using this source. The developed soft X-ray source with a wavelength range of 5~17 nm consists of a rotating drum system supplying cryogenic Xe target and a high repetition rate pulse Nd:YAG slab laser. Fig. 1 shows a soft X-ray irradiation system to microprocess samples.

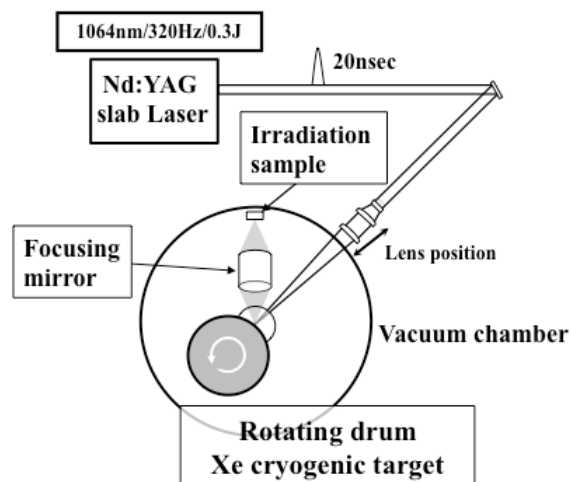


Fig.1 Experimental setup of the soft X-ray irradiation system.

The drum target system we developed has a cylindrical drum filled with liquid nitrogen, which cools its copper surface to the temperature of liquid nitrogen. Xe gas is directed onto the surface and condenses to form a solid Xe layer. The solid Xe-layer coated drum rotates about the vertical z-axis and moves vertically along the z-axis, resulting in a spiral motion, supplying a fresh target surface continuously for every laser shot. Emission spectrum from the Xe plasma has a very broad bandwidth (5~17 nm), so it was expected to be a high efficient soft X-ray source. When a Nd:YAG laser irradiated the target with a laser energy of 800 mJ and 300 mJ, a conversion efficiency in bandwidth of 5~17 nm was found to be 30 % and 21 %, respectively. The irradiation laser with a high average power (100 W) and a high repetition rate pulse (320 Hz) was also developed originally. It is a PCM-MOPA (Phase Conjugated Mirror – Master Oscillator and Power Amplifier) Nd:YAG slab system. High average output soft X-ray of 20 W at the wavelength range of 5~17 nm was achieved by using both the target system and the laser.

In order to increase an intensity of this soft X-ray, we used a focusing mirror. The mirror has a shape of a cylinder with three pieces of cylindrical Ru coated mirror. The piece with an angle of 101 degrees had a curvature radius of 26 mm. The X-ray energy intensity at a focal plane was measured to be 0.8 mJ/cm² using an X-ray diode. A beam pattern had a 1.8 mmf (FWHM) peak in a circle with a diameter of 24 mm[1].

Teflon PTEF: poly(tetrafluoroethylene) and PMMA: poly(methyl methacrylate) samples were irradiated to the soft-focused X-ray and their microprocessing was investigated[2].

In a Teflon sample, a contact angle of a modified surface with a water drop increased from 90° to 110° to by an irradiation without the mirror and a mask, while the angle decreased to 50° by an irradiation with the mirror and a Ni mesh (2000/inch) mask. Scanning electron microscopy showed numerous microprotuberances and a masked pattern having micro-concavities on the each sample surface (Fig.2). These suggested that the changes of the contact angle were ascribable to the microstructures of Teflon surface. We succeeded in controlling the wettability of the Teflon surface from hydrophobic to hydrophilic by microprocessing using the laser plasma X-ray.

PMMA is used for a resist in LIGA process and its etching rate for the laser plasma soft X-ray was investigated. After a large number of pulses (192000 pulses) with a low power density of 8×10⁴ W/cm² irradiated a PMMA sample through the Ni mesh, an etched depth was measured using a laser microscope. The etching rate was calculated to be 5 pm/pulse and this was concluded to be only photo-etching without thermal effect. We demonstrated pure photo-etching of the PMMA surface with the depth of ~1μm using the laser plasma X-ray.

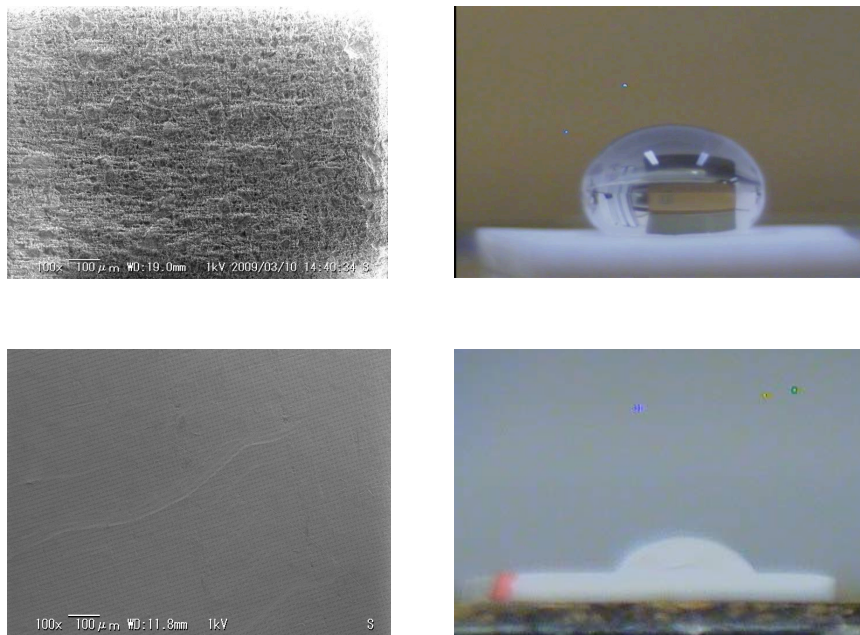


Fig.2 SEM pictures of the Teflon surface (left) and photographs of a water drop on it (right). The sample was irradiated without the mirror and the mask (upper), irradiated with them (lower).

References

- [1] S.Amano *et al.*, IEEJ Trans, **130**, pp.1768 (2010).
- [1] S.Amano *et al.*, IEEJ Trans, **134**, pp.489 (2014).

Broadband spectroscopy of magnetic response in a nano-scale magnetic wire

A. Yamaguchi¹, K. Motoi², H. Miyajima² and Y. Utsumi¹

¹Laboratory of Advanced Science and Technology for Industry, University of Hyogo, Koto Kamigori, Ako, Hyogo 678-1205

²Department of Physics, Keio University, Hiyoshi, Yokohama, Kanagawa 223-8522

Abstract

We measure the broadband spectra of magnetic response in a single layered ferromagnetic nano-scale wire in order to the size effect on ferromagnetic resonance. The resonance frequency difference between 300-nm- and 5- μm wide wires was varied by about 5 GHz. We detected the magnetization precession induced by the thermal direct current by using Wheatstone bridge circuit. Our investigation renders that the shape anisotropy is of great importance to control the resonance frequency and to provide thermal stability of the microwave devices

Introduction

The investigation on magnetization dynamics at gigahertz frequency in artificial nano-magnets is a great important subject for many applications of magnetic materials, examples of which include magnetoresistive random access memory, microwave detector and oscillator. [1] Up to now, these studies, by using not only electrical detection but also magnetic imaging techniques such as time-revolved Kerr microscopy and micro focus Brillouin light scattering, have been reported. In particular, the electrical detection, which allows the indirect detection of the resistance oscillation as a function of the input microwave signal frequency for the devices, provides high sensitive detection for magnetization dynamics on these devices below the several hundred nanometer scale. When we use a nano-scale magnet as a microwave device in a radio-frequency region, the magnetization fluctuation noise plays an important role. [2, 3] Several kinds of noise may restrict the signal-to-noise ratio, since the high-frequency thermal fluctuation of magnetization increases with the inverse of the device volume and it substantially limits both in the nano-scale device size and in the increase of the operating frequency. The theoretical and experimental understanding of the fundamental limitation is of practical importance.

The investigation on the non-equilibrium behavior of these systems is of great interest from a viewpoint of complicated magnetic processes; for example, the thermal nucleation of magnetic domain and the magnetization damping accompanied with the spin wave excitation. These problems have been investigated by the approach through simplifications that have proved successful in the theory of the stochastic processes. [3, 4]

Experiments and Results

We measure the broadband spectra of magnetic response in a single layered ferromagnetic nano-scale wire in order to investigate the size effect on the ferromagnetic resonance. We found that the resonance frequency difference between 300-nm- and 5- μm -wide wires was varied by about 5 GHz due to the shape anisotropy. Furthermore, we experimentally detected the magnetization precession induced by the thermal fluctuation via the rectification of a radio-frequency (rf) current by incorporating an additional direct current (dc) by using Wheatstone bridge circuit. Our investigation renders that the shape anisotropy is of great importance to control the resonance frequency and to provide thermal stability of the microwave devices.

We investigate electrical broadband spectroscopy for magnetic response including the noise in a single layered $\text{Ni}_{81}\text{Fe}_{19}$ (Permalloy: Py) wire. The soft-ferromagnetic Py nano-scale wires are fabricated onto a polished MgO (100) substrate by means of high-resolution electron beam lithography with a standard lift-off technique. The thickness t , width W and length L of the Py wires prepared in this study are summarized in Table I. The coordinate systems are defined as shown in Fig. 1(a). Here, we assume that the wire system is a single-domain magnetic particle. The longitudinal axis and short axis of the wire are parallel to the x - and y -axes in the plane, respectively. The K_{\perp} and K_{\parallel} are the hard and easy axis anisotropy constants in the out-of-plane and in-plane directions, respectively. The wires are placed between the center strip-line of the coplanar waveguide (CPW) comprising Au conductive strip with thickness of 100 nm. The ground-signal-ground (GSG) typed microwave probe is connected to the system. The real part of S_{11} is measured by a vector network analyzer (VNA), and dc voltage difference induced by the rf current flowing through the wire is detected by the bias tee circuit which can separate the dc and rf components of the current. The optical micrograph image is shown in Fig. 1(b). In addition, the broadband spectroscopy under the application of the dc current is measured by Wheatstone bridge circuit as shown in Fig. 1(b). An external magnetic field H_{ext} is applied in the substrate

plane along the angle ϕ_H from the longitudinal axis of the Py wire. All experimental measurements are performed at room temperature.

Table 1. Summary of sample structure

Sample	Length (μm)	Width (nm)	Thickness (nm)
#1	20	300	50
#2	20	650	50
#3	20	2200	50
#4	100	5000	30
#5			

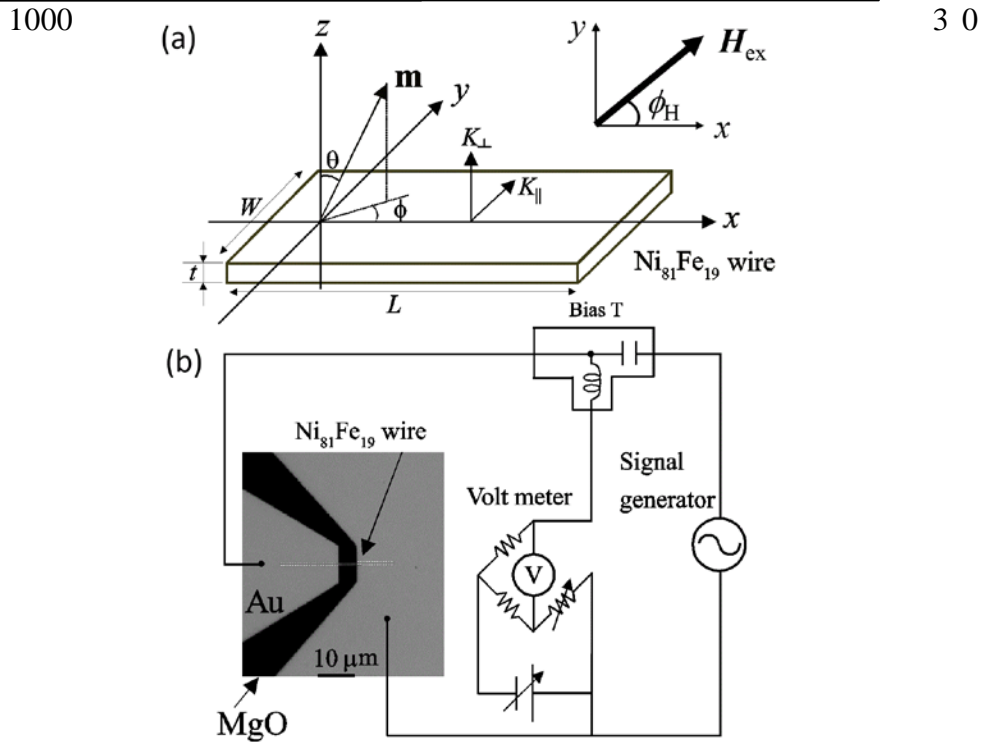


Fig. 1(a) Schematic of system coordinate and notation definition. m is the unit vector of the magnetic moment. (b) Schematic diagram of the broadband magnetic response measurement circuit using Wheatstone bridge.

The magnetic field was applied at angle $\phi_H = 45^\circ$ to the longitudinal axis of the wire #2 in plane. Figures 2(a) and 2(b) show the magnetic field dependence of real part of S11 and rectifying spectra in the wire #2, respectively. For clarity, the measured spectra are vertically shifted. As shown in the S11 spectra, we can see a stationary peak positions at 9 GHz and a shift towards the higher frequency with increasing the magnetic field. The former stationary peak corresponds to the natural FMR mode in the absence of the magnetic field in this case, because we calibrate the S11 spectrum of the wire in the magnetic field of 0 G. The later shift represents the ferromagnetic resonance.

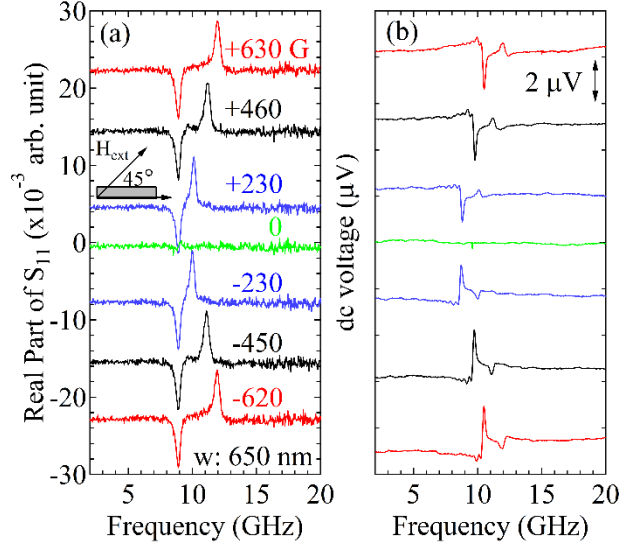


Fig. 2(a) Real Part of S11 as a function of frequency in various magnetic fields. (b) Field dependence of rectifying spectra.

The resonance frequencies determined by the measurements of S11 and rectifying effect are the almost same as shown in Figs. 2(a) and 2(b). The response signal from the intrinsic ferromagnetic resonance in the S11 is overlapped the extrinsic signal which gives the stationary peak. On the other hand, the rectifying effect can reveal the only intrinsic response signal as shown in Fig. 2(b). The results suggest that the rectifying effect is more suitable to detect the spin dynamics in the nano-scale magnets.

The magnetic field dependence of the resonance frequency of each wire is shown in Fig. 3(a). The resonance frequency increases with increasing magnetic field, as expected by the following extended Kittel equation given by [5, 6]

$$\omega_0 = \gamma\mu_0 \sqrt{(H_{\text{ext}} + H_K^{\parallel} + H_K^{\perp})(H_{\text{ext}} + H_K^{\parallel})}, \quad (1)$$

where γ is the gyromagnetic ratio and μ_0 is the magnetic permeability. Generally assuming that the present system is treated as the single-domain magnetic particle, the easy and hard anisotropic fields are given by $H_K^{\parallel} = \frac{2K_{\parallel}}{\mu_0 M_S}$ and $H_K^{\perp} = \frac{2K_{\perp}}{\mu_0 M_S}$. When a static magnetic field is applied at the angle ϕ_H from the longitudinal axis of the wire in the plane, the resonance frequency is modified as the following: [5, 6]

$$\omega_0 = \gamma\mu_0 \sqrt{H_{K\text{eff}}^{\perp} H_{K\text{eff}}^{\parallel}}, \quad (2)$$

where

$$H_{K\text{eff}}^{\parallel} = H_{\text{ext}} \cos(\phi_H - \phi) + M_S (N_y - N_x) \cos 2\phi \quad (3)$$

and

$$H_{K\text{eff}}^{\perp} = H_{\text{ext}} \cos(\phi_H - \phi) + M_S \{N_z - (N_x \cos^2 \phi + N_y \sin^2 \phi)\}. \quad (4)$$

Here, M_S is the saturation magnetization, N_{α} ($\alpha = x, y, z$) the demagnetizing factors in the Cartesian coordinate system (x, y, z) , and ϕ the angle between the longitudinal axis of the wire and the effective magnetic moment vector (see Fig. 1(a)). The Equation (2) enables us to determine the demagnetizing factors and to control the resonance frequency by shape of the sample. The demagnetizing factors can be analytically calculated by Aharoni's theory. [7] Using the calculated demagnetizing factors summarized in Table II, $M_S = 1.08 \text{ T}$ for the Py and $\phi = 22^\circ$, we plot the fitting curves given by Eq. (2) as a function of magnetic field as shown in Fig. 3(a). The fitting curves are in fairly good agreement with the experimental data. Concurrently with the fitting results, this fact indicates that the effective magnetization in the wire is not aligned in the parallel direction of the applied magnetic field because of the strong magnetic shape anisotropy. In the absence of the magnetic field, the anisotropy field of the width direction $H_{\text{eff}}^{\parallel}$ cannot be neglected. These results indicate that the shape anisotropy enables us to control the resonance frequency and to provide the design guideline for the microwave devices.

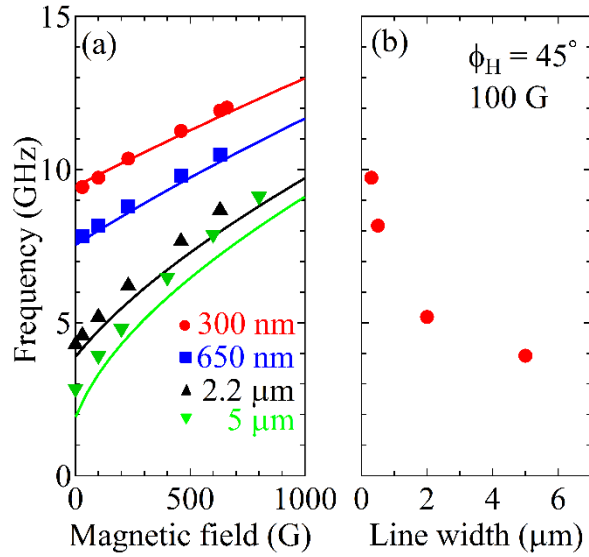


Fig. 3(a) Magnetic field dependence of Ferromagnetic resonance. (b) Resonance frequency as a function of line width in the magnetic field of 100 G.

We investigate the excitation of magnetization precession due to the application of the dc current. Figure 4(a) shows the dc current dependence of the rectifying spectra peak height in the magnetic field of 100 Oe at $\phi_H = 45^\circ$. The dc current dependence of the spectra is shown in the inset of Fig. 4(b). As shown in the inset, the dc current excited the resonance peak. The full width at half maximum (FWHM) is plotted as a function of dc current as shown in Fig. 4(b). We found that the spectrum amplitude (peak height at the FMR state) is proportional to the dc current and the FWHM increases with the increment of the dc current. This dc current dependence of the FWHM correlates well with the parabolic fitting curve as shown in Fig. 4(b). These results indicate that the Joule heating due to the dc current [8, 9] induces the thermal excitation of magnetization precession and produces the rectifying spectra due to the excitation of the higher dipole-spin wave mode.

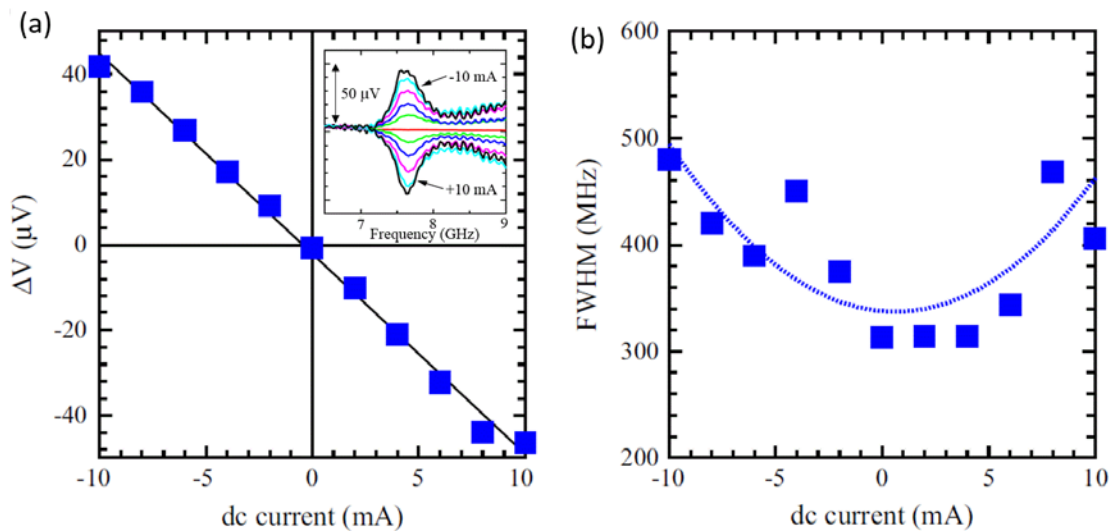


Fig. 4 (a) Peak strength and (b) Full width at half maximum (FWHM) of rectifying spectra excited by dc + rf currents as a function of dc current. The applied field of 100 G was fixed at $\phi_H=45^\circ$ in the plane. The inset of Fig. 4(a) shows the dc current dependence of the rectifying spectra.

Conclusion

Thus, the present experimental results reveal that our electrical Wheatstone bridge measurement technique is useful for the high sensitive detection of the small magnetization precession in a nano-scale magnetic wire under the application of the dc current. This measurement technique and investigation open the door to the fundamental spin dynamics of nano-scale magnets with very easy operation and design guideline of the rf-devices using the nano-scale magnets.

References

- [1] B. Hillebrands and K. E. Ounadjela, *Spin Dynamics in Confined Magnetic Structures* (Springer, Berlin, 2003), Vols. 1 - 3.
- [2] W. F. Brown, Jr. *Phys. Rev.* **130**, 1677 (1963).
- [3] N. Smith and P. Arnett, *Appl. Phys. Lett.* **78**, 1448 (2001).
- [4] V. Safonov and N. Bertram, *Phys. Rev. B* **65**, 172417 (2002).
- [5] A. Yamaguchi, K. Motoi, A. Hirohata, H. Miyajima, Y. Miyashita, and Y. Sanada, *Phys. Rev. B* **78**, 104401 (2008).
- [6] A. Yamaguchi, K. Motoi, M. Miyajima and Y. Utsumi, *J. Magn. Magn. Matter.* **364**, 34 (2014).
- [7] A. Aharoni, Demagnetizing factors for rectangular ferromagnetic prisms, *J. Appl. Phys.* **83**, 3432 (1998).
- [8] A. Yamaguchi, S. Nasu, H. Tanigawa, T. Ono, K. Miyake, K. Mibu and T. Shinjo, Effect of Joule heating in current-driven domain wall motion. *Applied Physics Letters* **86**, 012511-1-3 (2005); A. Yamaguchi, A. Hirohata, T. Ono and H. Miyajima, Temperature estimation in a ferromagnetic Fe-Ni nanowire involving a current-driven domain wall motion, *Journal of Physics Condensed Matter* **24**, 024201-1-9 (2012).
- [9] H. Fangohr, D. S. Chernyshenko, M. Franchin, T. Fischbacher and G. Meier, Joule heating in nanowires, *Physical Review B* **84**, 054437-1-12 (2011).

Dihedral Corner Reflector Array for floating image manufactured by Synchrotron radiation

T.Yamane^a, S.Maekawa^{a,b}, I.Okada^a, Y.Utsumi^a, A.Yamaguchi^a

^aLaboratory of Advanced Science and Technology for Industry, University of Hyogo,
3-1-2 Koto, Kamigori, Hyogo 678-1205, Japan

^bParity Innovations, 3-5 Hikaridai, Seika, Soraku, Kyoto, Japan
E-mail: t.yamane@lasti.u-hyogo.ac.jp, Phone/Fax: +81-791-58-0232

ABSTRACT

We have made a new imaging optics called the Dihedral Corner Reflector Array (DCRA) which is designed to make the floating image by using synchrotron radiation. DCRA consists of numerous micro-mirrors placed perpendicular to the surface of substrate. The micro-mirror is implemented by the side of minute square pillar. The primordial is based on two reflections by a pair of adjacent mutually perpendicular mirrors, *i.e.*, a dihedral corner reflector. Although the principal of operation is based on reflection by mirrors, the device is also transmissive and deflects light. Primordial of DCRA is not so complicated. However, it is too difficult to fabricate the DCRA by usual machining because of high aspect ratio micromachining. Therefore, in this manuscript, we fabricated the device by deep X-ray lithography due to synchrotron radiation. The characteristics of the fabricated DCRA are evaluated by the optical transmission and reflection measurements.

1. INTRODUCTION

We have made a new imaging optics called the Dihedral Corner Reflector Array (DCRA) which is designed to make the floating image by using synchrotron radiation. DCRA as shown in Figure.1 (a), it consists of numerous pair of perpendicular micro-mirrors *i.e.*, a dihedral corner reflector (DCR) placed perpendicular to the surface of substrate [1]. DCR on the substrate can converge all the light from a light source onto the reflection-symmetric point of the source.(Fig 1(b)) As a result, floating image issue the same light when observing the light source, the array of numerous dihedral corner reflectors, namely DCRA, can realize the floating image. The DCR is implemented by the side of minute square pillar. Therefore it is impossible to polish them in pre- or post-processes. And, the micro-fabrication of high precision is required for the fabrication of DCRA. The fabrication process using the SR enables us to fabricate the DCRA structure within the limit of accuracy of about 10 nm. [2] Therefore, in this manuscript, we fabricated the device by deep X-ray lithography due to synchrotron radiation. The characteristics of the fabricated DCRA are evaluated by the DCRA transmittance.

2. EXPERIMENT

In this manuscript, we fabricated the pillar patterned DCRA made of Poly-methyl methacrylate (PMMA) by using synchrotron radiation. The pillar pattern DCRA utilizing the light from the light source passes through the interior of the PMMA, and totally reflected by the difference in refractive index between air. Figure 2 shows schematic of dimensions of our DCRA device. And Table 1 shows dimension of DCRA. Here, we postulate that the transmittance of DCRA is the percentage of incident light through the reflection-symmetric point. The transmittance is given by

$$\text{Transmittance} = I \times R^2 \times T, \quad (1)$$

where I is the ideal transmittance, R is reflectance of micro-mirror, and T is the losses, which is defined as the attenuation of intensity of the incident light after passing through the DCRA.

Reflectance of micro-mirrors is the most important factor in imaging by DCRA. In this study, we evaluate the characteristics of the fabricated DCRA by measuring the dimension, perpendicularity of the reflector, fractional and reflection. The reflection ratio are measured by measurement system as shown in Fig.3. In order to evaluate the angle ϕ dependence of the single reflection of the DCRA at 700 nm in wavelength, we fixed the DCRA at the angle $\theta = 25^\circ$. As shown in Fig. 4, two reflection peaks are observed. The peak with the larger amplitude (at about $\phi = 0^\circ$) corresponds to the refractive incident light. The other is the single reflection of the light by the DCRA. If the ideal DCRA was fabricated, we would obtain the single reflection peak at $\phi = 50^\circ$ in this experimental setup. And reflection of our devise is 15%. However, we found the single reflection was extended in the ϕ range between 40° and 70° because the reflected light was spread by the

distortion due to the taper. The actual fraction transmitted is estimated to be 5.4% by substituting the measured value into Equation (1). Figures 5(a) and 5(b) show a typical optical microscope image of top view and cross section of the micro-pillars in the fabricated DCRA, respectively. The measured average dimensions of the DCRA are summarized in Table 2. The measured dimensions except the perpendicularity are almost in good agreement with the design dimensions. The perpendicularity of the fabricated pillars have about 6 minute taper.

3. CONCLUSION

We proposed novel imaging optics with micro-dihedral corner reflector arrays (DCRA) which can form a reflection-symmetric image as a real image in the air. Although the performance of the DCRA was not good, the fabricated DCRA enables us to observe a floating image. Now, we couldn't measure the perpendicularity and reflectance of a single pillar. Our main work to improve imaging in the future is to increase transmittance and establish the quantitative measurement method of resolution and reflection ratio.

REFERENCE

- [1]. S. Maekawa. "Transmissive Optical Imaging Device with Micromirror Array" The International Society for Optical Engineering, Vol.6392, 63920E-1, (2006)
- [2] M.Ishikawa, "A proposal to create the impression of a miniature garden, and the development of a glasses-free small 3d display", Pioneer R&D 12(3), pp.47-58, 2003. In Japanese

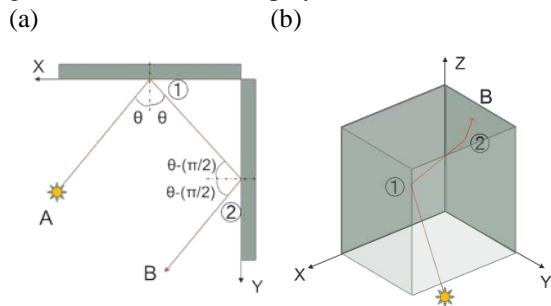


Figure 1. outlook of DCR

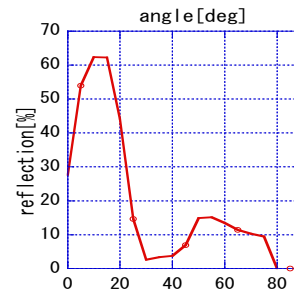


Figure.4. the single reflectance of the sidewalls of our device.
(y axis angle means φ)

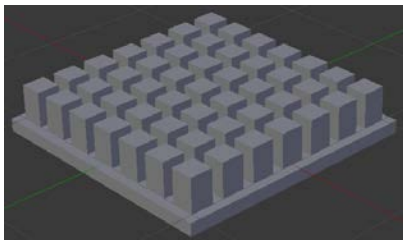


Figure 2. schematic of our DCRA device

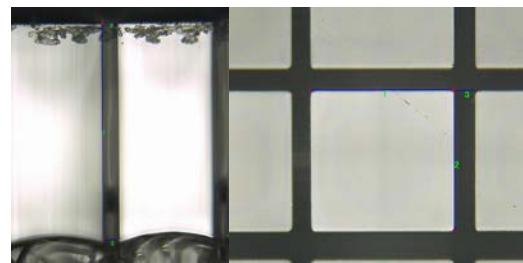


Figure.5. optical microscope image of pillars

Table.1.Dimension of DCRA

position	dimension
Pillar dimension[μm]	150
Pillar height [μm]	300
Pitch[μm]	25
Aperture ratio[%]	64.9
Perpendicularity[deg]	90
Roughness[nm]	10

Table.2. dimension of manufactured DCRA

Pillar dimension [μm]	150.92
Pillar height [μm]	326.78
Pitch [μm]	25.87
Perpendicularity[minute]	5.8

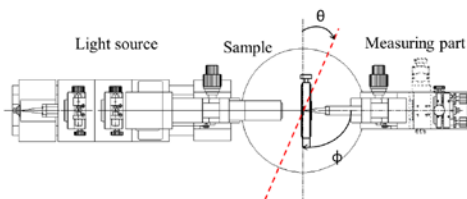


Figure 3. the reflectance of side walls of the transmitted light measuring instrument

Evaluation of localized friction for antisticking layer by atomic force microscopy

Makoto Okada¹, Yuichi Haruyama¹, and Shinji Matsui¹

¹Laboratory of Advanced Science and Technology for Industry, Univ. of Hyogo,
Ako, Hyogo, 678-1205, Japan
E-mail address: m.okada@lasti.u-hyogo.ac.jp

Nanoimprint lithography (NIL)¹⁾ is able to produce the nanostructures with high precision. The nanoimprint mold is usually coated with an antisticking layer (ASL) because NIL is a contact process and it is necessary to prevent the adhesion of resin. It is known that the ASL deteriorates with repeated nanoimprinting. Hence, we have to study the cause of ASL deterioration induced by repeated nanoimprinting. However, this is a difficult issue because NIL includes several factors such as localized movement, chemical reaction, and UV irradiation, etc. and these factors influence the ASL deterioration. One of the factors that ASL deteriorates during nanoimprinting is a localized friction between the ASL and nanoimprint resin, as shown in Fig. 1. Atomic force microscope (AFM) is a useful tool to observe the sub-nm- and nm-order morphology. In AFM observation, there are three types of mode, contact mode, dynamic force mode (also called tapping mode), and non-contact mode. We focused on the contact mode-AFM because a cantilever is in direct contact with a sample and is scanning on the sample during observation. This means that the localized friction between the cantilever tip and sample occurs during contact mode-AFM observation. Furthermore, we can measure the adhesion and frictional forces on the sample by AFM. In previous work, we reported the abrasion test of ASL formed using (3,3-trifluoropropyl)trimethoxysilane (FAS-3) by AFM²⁾. However, FAS-3 is rarely used as the nanoimprint ASL due to a worse release property and the number of rubbing was only about 600 times in the measurement. In this study, we used ASL formed using (tridecafluoro-1,1,2,2-tetrahydrooctyl)trimethoxysilane (FAS-13) which has a good release property, and carried out abrasion test by AFM with rubbing over 5000 times.

We used a sphere tip (NanoWorld AG) instead of a standard cantilever which has a sharp tip to avoid scratching. The sphere diameter was 0.8 μm . Figure 2 shows the illustration diagram of abrasion test by AFM using the sphere tip. The ASL was coated on SiO_2/Si substrate with mesa structure. The mesa structure was 1.6 $\mu\text{m} \times 1.6 \mu\text{m}$. The continuous contact-mode AFM was carried out on the mesa structure, and the adhesion and frictional forces were intermittently measured on the rubbed area. The rubbed area was 1 $\mu\text{m} \times 1 \mu\text{m}$. The contact force and scanning speed were 200 nm and 10 Hz, respectively. We defined a one scan as a one rubbing time. Figures 3(a) and 3(b) show the adhesion and frictional forces on the rubbed ASL as a function of number of rubbing times. The adhesion force before abrasion test was the highest in the measurement. We assumed that the ASL was contaminated before starting the test. Contrary to our expectations, the adhesion and frictional forces increased and decreased during the test. After abrasion test, we observed the ASL by dynamic force mode-AFM, as shown in Fig. 4. The ASL surface state was affected by rubbing of sphere tip. We assumed from these results that the contamination attached to the top of sphere tip and removed during rubbing and affected the adhesion and frictional force measurements.

Acknowledge

This work was partially supported by Kawanishi Memorial ShinMaywa Education Foundation.

References

- 1) S. Y. Chou, et al.: Appl. Phys. Lett., **67** (1995) 3114.
- 2) M. Okada, et al.: Abstr., MNC2013, 8P-11-79 .

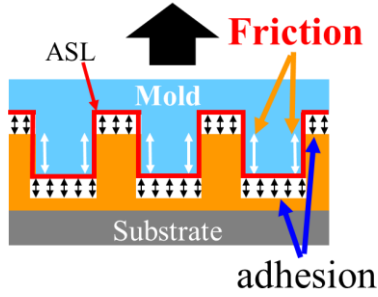


Figure 1 Illustration diagram of demolding process.

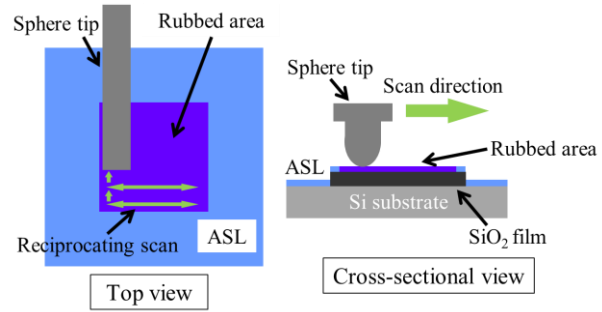


Figure 2 Illustration diagram of abrasion test by AFM.

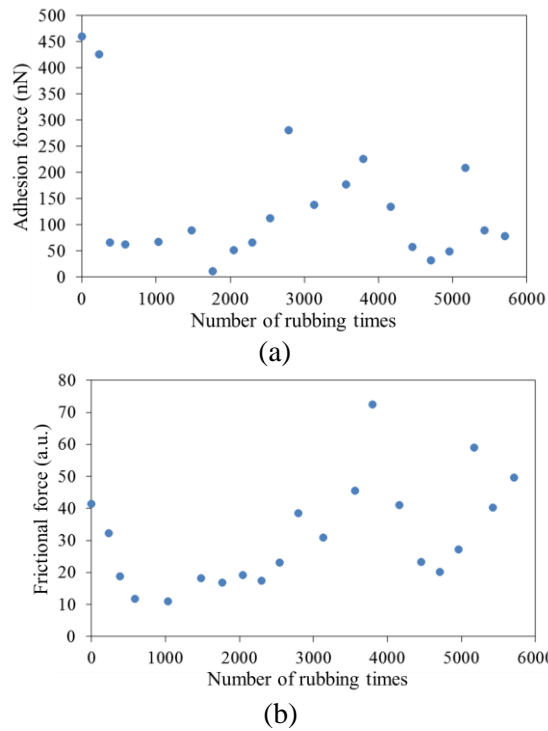


Figure 3 (a) Adhesion and (b) frictional forces on ASL during abrasion test by AFM.

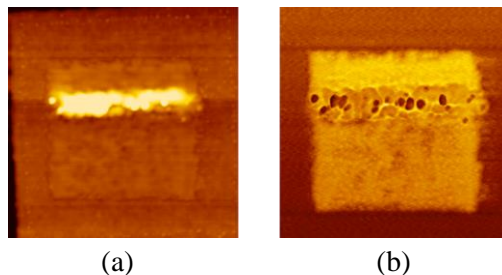


Figure 4 (a) Topographic and (b) phase images of FAS-13 after abrasion test by AFM.

List of Publications

List of publications

(1)Papers

1. T. Inoue, T. Mochizuki, S. Miyamoto, K. Masuda, S. Amano, and K. Kanda, "Investigation of Ru Focusing Mirror for 5- to 17-nm Soft X rays from Laser-Produced Plasma", Review of Laser Engineering, vol.41, no.1, pp.59-62 (2013). (in Japanese)
2. D. Li, M. Hangyo, Z. Yang, Y. Tsunawaki, Y. Wei, Y. Wang, S. Miyamoto, M. R. Asakawa, and K. Imasaki, "Theoretical analysis and simulation of growth rate and start current in Smith–Purcell free-electron lasers", Terahertz Science and Technology, ISSN 1941-7411, vol.6, no.3, pp.189 -205 (2013).
3. Shuji Miyamoto, "Development of Technology and Application of Laser Compton Scattering Gamma-Ray Beam", Review of Laser Engineering, vol.41, no.11, pp.917-921 (2013). (in Japanese)
4. Y.Shoji, "Landau Damping of Collective Betatron Oscillation in a Quasi-Isochronous Electron Storage Ring", Nucl. Instr. and Meth. in Phys. Res. A729, pp.1-2 (2013).
5. S.Amano, T.Inoue, T.Harada, "Plasma debris sputter resistant x-ray mirror", Applied Optics, Vol.52, pp.3845-3848 (2013).
6. S.Amano, T.Inoue, "Diamond-like carbon sputtering by laser produced Xe plasma", NIMB, Vol.314, pp.26-29, (2013).
7. T.Sekioka, S.Amano, T.Inoue, T.Mochizuki, "Characteristics of fast ions from laser produced plasma and their applicability to Shallow junction doping", NIMB, Vol.314, pp.162-165, (2013).
8. K. Kanda, M. Niibe, A. Wada, H. Ito, T. Suzuki, T. Ohana, N. Ohtake, and H. Saitoh, "Comprehensive Classification of Near-Edge X-Ray Absorption Fine Structure Spectra of Si-Containing Diamond-Like Carbon Thin Films", Jpn. J. Appl. 52 pp.095504, (2013).

9. K. Ozeki, D. Sekiba, T. Suzuki, K. Kanda, M. Niibe, K.K. Hirakuri, T. Masuzawa, "Influence of the source gas ratio on the hydrogen and deuterium content of a-C:H and a-C:D films: plasma-enhanced CVD with CH₄/H₂, CH₄/D₂, CD₄/H₂ and CD₄/D₂", *Applied Surface Science*, 265, pp.750, (2013).
10. A. Heya, N. Matsuo, M. Takahashi, K. Ito, and K. Kanda, "Crystallization of Si_{1-x}Ge_x Multilayer by soft X-ray Irradiation", *Applied Physics Express*, 6, pp.065501, (2013).
11. A. Heya, K. Kanda, K. Toko, T. Sadoh, S. Amano, N. Matsuo, S. Miyamoto, M. Miyao, T. Mochizuki, "Low-temperature crystallization of amorphous silicon and amorphous germanium by soft X-ray irradiation", *Thin Solid Films*, 534, 334-340, (2013).
12. K. Kanda, T. Hasegawa, M. Uemura, M. Niibe, Y. Haruyama, M. Motoyama, K. Amemiya, S. Fukushima and T. Ohta, "Construction of a Wide-range High-resolution Beamline BL05 in NewSUBARU for X-ray Spectroscopic Analysis on Industrial Materials", *J. Phys.: Conf. Ser.* 425, pp.065501, (2013).
13. H. Ito, S. Onitsuka, R. Gappa, H. Saitoh, R. Roacho, K. H. Pannell, T. Suzuki, M. Niibe, K. Kanda, "Fabrication of Amorphous Silicon Carbide Films from Decomposition of Tetramethylsilane using ECR plasma of Ar", *J. Phys.: Conf. Ser.* 441, pp.012039, (2013).
14. S. Honda, R. Tamura, Y. Noshio, A. Tsukagishi, M. Niibe, M. Terasawa, R. Hirase, H. Izumi, H. Yoshioka, K. Niwase, E. Taguchi, K-Y. Lee, M. Oura, "Transformation of multiwalled carbon nanotubes to amorphous carbon nanorods under ion irradiation", *Jpn. J. Appl. Phys.* 53 02BD06, (2014).
15. K. Kanda, K. Fukuda, K. Kidena, R. Imai, M. Niibe, S. Fujimoto, K. Yokota, M. Tagawa: "Hyperthermal atomic oxygen beam irradiation effect on the Ti-containing DLC film", *Diamond Related Materials*, pp.41 49-52, (2014).
16. R. Kawakami, M. Niibe, H. Takeuchi, M. Konishi, Y. Mori, T. Shirahama, T. Yamada, and K. Tominaga: "Surface damage of 6H-SiC originating from argon plasma irradiations", *Nucl.*

Instrum. Methods in Phys. Res., B pp.315 213-217, (2013).

17. Tsukagishi, S. Honda, R. Osugi, H. Okada, M. Niibe, M. Terasawa, R. Hirase, H. Izumi, H. Yoshioka, K. Niwase, E. Taguchi, K-Y. Lee, M. Oura, "Spectroscopic characterization of ion-irradiated multi-layer graphenes", Nucl. Instrum. Methods in Phys. Res., B 315 pp.64-67 (2013).
18. R. Kawakami, M. Niibe, Y. Nakano, T. Shirahama, T. Yamada, K. Aoki, M. Takabatake, K. Tominaga, and T. Mukai, "Damage characteristics of n-GaN thin film surfaces etched by N₂ Plasmas", Physica Status Solidi, C 10, pp.1553-1556, (2013).
19. R. Kawakami, M. Niibe, Y. Nakano, M. Konishi, Y. Mori, A. Takeichi, K. Tominaga, and T. Mukai, "Comparison between Damage Characteristics of p- and n-GaN Surfaces Etched by Capacitively Coupled Radio Frequency Argon Plasmas", Jpn. J. Appl. Phys. 52, pp.05EC05, (2013).
20. R. Kawakami, M. Niibe, Y. Nakano, M. Konishi, Y. Mori, H. Takeuchi, T. Shirahama, T. Yamada, and K. Tominaga: "Characteristics of TiO₂ Surfaces Etched by Capacitively Coupled Radio Frequency N₂ and He Plasmas", J. Phys.: Conf. Series, 441, pp.012038, (2013).
21. T. Kobayashi, D. Itami, R. Hashimoto, T. Takashina, H. Kanematsu, K. Mizuta and Y. Utsumi, "Optimizing Structure of LED Light Bulb for Heat Transfer", Journal of Physics Conference Series, 433, pp.012016, (2013).
22. T. Kobayashi, M. Doi, T. Fukuda, R. Hashimoto, H. Kanematsu and Y. Utsumi, "Study on evaluation methods Performance Simulation of Polymer Electrolyte Fuel Cell", Journal of Physics: Conference Series 433 (2013), pp.012021, (2013).
23. T. Kobayashi, K. Doi, H. Kanematsu, Y. Utsumi, R. Hashimoto, and T. Takashina "Remote Sensing of Radiation Dose Rate by a Robot for Outdoor Usage", Journal of Physics: Conference Series 433 (2013), pp.012030, (2013).
24. T. Kobayashi, S. Kamikawa, Y. Itou, H. Kanematsu and Y. Utsumi, "Effect of Deposition and

- Storage Conditions on the Gas Permeability of SiO_x Thin Films” *Applied Mechanics and Materials*, 378, pp.248-252, (2013).
25. 岸原充佳, 山島芸, 内海裕一, “ポスト壁導波路を用いたチップサイズ連続マイクロ波照射構造,” *電気学会論文誌, Sec.E, Vol.133, No.12*, pp.365-371, (2013).
 26. Takeo Watanabe, Yukiko Kikuchi, Toshiya Takahashi, Kazuhiro Katayama, Isamu Takagi, Norihiko Sugie, Hiroyuki Tanaka, Eishi Shiobara, Soichi Inoue, Tetsuo Harada, and Hiroo Kinoshita, “Development of Tool for Contamination Layer Thickness Measurement Using High Power Extreme Ultraviolet Light and In-Situ Ellipsometer,” *Jpn. J. Appl. Phys.* 52 pp.056701-1, 056701-5, (2013).
 27. Takeo Watanabe, Kazuya Emura, Daiji Shiono, Yuichi Haruyama, Yasuji Muramatsu, Katsumi Ohmori, Kazufumi Sato, Tetsuo Harada, and Hiroo Kinoshita, “EUV Resist Chemical Reaction Analysis using SR,” *J. Photopolym. Sci. Technol.* 26, pp.635-642, (2013).
 28. Isamu Takagi, Toshiya Takahashi, Norihiko Sugie, Kazuhiro Katayama, Yukiko Kikuchi, Eishi Shiobara, Hiroyuki Tanaka, Soichi Inoue, Takeo Watanabe, Tetsuo Harada, and Hiroo Kinoshita, “Comparison of Resist Family Outgassing Characterization between EUV and EB,” *J. Photopolym. Sci. Technol.* 26, pp.673-678, (2013).
 29. Tsuyoshi Amano, Susumu Iida, Ryoichi Hirano, Tsuneo Terasawa, Hidehiro Watanabe, Kenjiro Yamasoe, Mitsunori Toyoda, Akifumi Tokimasa, Tetsuo Harada, Takeo Watanabe, and Hiroo Kinoshita, “Observation of Residual-Type Thin Absorber Defect on Extreme Ultraviolet Lithography Mask Using an Extreme Ultraviolet Microscope,” *Appl. Phys. Express* 6 pp.046501-1, 046501-3, (2013).
 30. Y. Nagata T. Harada, T. Watanabe, K. Midorikawa, and H. Kinoshita, “Defect Sensing of EUV Mask using Coherent EUV Light,” (in Japanese), *Journal of the Institute of Electrical Engineers of Japan A*, 133, pp.509-518, (2013).
 31. T. Kudo, K. Kobayashi, S. Ono, N. Teranishi, T. Watanabe, H. Kinoshita, M. Okihara, and T. Hatsui, “Development of High-Speed Evaluation Method of Radiation hardness of

- Semiconductor Devices,” Silicon Technology Division of the Japan Society of Applied Physics 170, “The Effect of Radiation Irradiation to Semiconductor Devices”, pp.24-29, (2014).
32. M. Okada, E. Nishioka, M. Kondo, Y. Haruyama, T. Sasaki, H. Ono, N. Kawatsuki and S. Matsui, “Comparison Molecular Orientation of Photoinduced Liquid Crystalline Polymer induced by Thermal Nanoimprinting to that by Graphoepitaxy”, *Journal of Photopolymer Science and Technology*, 26, pp.65-68, (2013).
 33. M. Okada, E. Nishioka, M. Kondo, Y. Haruyama, T. Sasaki, H. Ono, N. Kawatsuki and S. Matsui, “Molecular Orientation of Photoinduced Liquid Crystalline Polymer with 3D Structure fabricated by Thermal Nanoimprinting”, *Journal of Photopolymer Science and Technology*, 26, pp.83-85, (2013).
 34. T. Oyama, M. Okada, S. Iyoshi, Y. Haruyama, H. Miyake, T. Mizuta and S. Matsui, “Surface Evaluation of Cationic UV-curable Resin with Fluorine Additive by X-ray Photoelectron Spectroscopy”, *Journal of Photopolymer Science and Technology*, 26, pp.129-132, (2013).
 35. H. Wakaba, M. Okada, S. Iyoshi, Y. Haruyama and S. Matsui, “Release Property Evaluation of Fluorinated Antisticking Layer by a Mixture of Release Agents”, *Journal of Photopolymer Science and Technology*, 26, pp.143-146, (2013).
 36. T. Watanabe, K. Emura, D. Shiono, Y. Haruyama, Y. Muramatsu, K. Ohmori, K. Sato, T. Harada and H. Kinoshita, “EUV Resist Chemical Reaction Analysis using SR”, *Journal of Photopolymer Science and Technology*, 26, pp.635-641, (2013).
 37. M. Okada, H. Miyake, S. Iyoshi, T. Yukawa, T. Katase, K. Tone, Y. Haruyama, S. Matsui “Double patterning in nanoimprint lithography”, *Microelectronic Engineering* 112, pp.139-142, (2013).
 38. M. Okada, Y. Haruyama, S. Matsui, E. Nishioka, R. Hosoda, M. Kondo, N. Kawatsuki, T. Sasaki and H. Ono, “Reorientation of photoreactive liquid crystalline polymer pattern fabricated by hybrid nanoimprinting”, *Journal Vacuum Science Technology B* 31, pp. 06FB04-1-06FB04-4, (2013).

39. N. Kawatsuki, Y. Inada, M. Kondo, Y. Haruyama, and S. Matsui, "Molecular Orientation at the Near-Surface of Photoaligned Films Determined by NEXAFS", *Macromolecules* 47, pp.2080–2087, (2014).

(2)Internatonal Meetings

1. Shuji Miyamoto (invited), "Laser Compton Scattering Gamma-ray Source and Nuclear Applications - Photo Nuclear Reaction and Transmutation-", International Conference on Laser Applications in Nuclear Engineering LANE 2013, Pacifico YOKOHAMA, Japan, April 23-25 (2013).
2. S.Miyamoto, S.Amano, S.Hashimoto, M.Terasawa, A. Koizumi, T. Mochizuki, H. Utsunomiya, T. Shima, T.Hayakawa, T.Shizuma, K.Imasaki, D.Li, Y.Izawa, F.Hori, Y.Asano and H.Ohkuma, "Gamma-ray Generation and Application by Laser Compton Scattering", The Eighth International Conference on Inertial Fusion Science and Applications (IFSA), P.Th_76, Nara Prefectural New Public Hall, Nara, Japan, Sept. 8-13 (2013).
3. Shuji Miyamoto (invited). "Gamma-ray Generation and Application by Laser Compton Scattering", "Interaction Meeting on X-ray Lithography and Microfabrication" , Raja Ramanna Center for Advanced Technology, Indore, India,December 5-6 (2013).
4. S.Miyamoto, S.Amano, S.Hashimoto, T.Mochizuki, K.Imasaki, D.Li, Y.Izawa (invited), "Laser Compton Gamma-ray Application for Nuclear Decommissioning", International Workshop on Laser Application to Nuclear Decommissioning and Decontamination (LANDD2013), The Wakasawan Energy Research Center, Tsuruga, Japan, December 12 (2013).
5. Shuji Miyamoto (invited), "Laser Compton Gamma-ray Beam Source at NewSUBARU", International Workshop on "Nuclear Physics and Gamma-ray sources for Nuclear Security and Nonproliferation (NPNSNP)", Ricotti, Tokai, Japan, January 28-30 (2014).
6. K. Kobayashi, Y.Kawamoto, W.El-Masry, M.Eto, H. Tokimura, T.Kaneko, Y.Obayashi, H.Mita,

- Kanda, S.Yoshida, H.Fukuda and Y.Oguri, "Evolution of Interstellar Organics to Meteoritic and Cometary Organics: Approaches by Laboratory Simulations", International Astrobiology Workshop 2013, Sagamihara, Nov.28-Dec.1,(2013).
7. K. Kobayashi, H. Mita, H. Yabuta, K. Nakagawa, Y. Kawamoto, K. Kanda, E. Imai, H.Hashimoto, S. Yokobori, A. Yamagishi, and Tanpopo WG, "pace Exposure of Amino Acids and Their Precursors in the Tanpopo Mission Using the International Space Station", 29th International Symposium on Space Technology and Science, Nagoya, Jun.2-9,(2013).
 8. R. Imai, A. Fujimoto, M. Okada, S. Matsui, T. Yokogawa, E. Miura, T. Yamasaki, T. Suzuki, K. Kanda, "Soft X-ray Irradiation Effect on the Surface and Material Properties of Highly Hydrogenated Diamond-like Carbon Thin Films", New Diamond and Nano Carbons Conference, Singapore, May. 19-23,(2013).
 9. K. Kanda, K. Fukuda, K. Kidena, R. Imai, M. Niibe, S. Fujimoto, K. Yokota, M. Tagawa, "Hyperthermal Atomic Oxygen Beam Irradiation Effect on the Ti-containing DLC Film", New Diamond and Nano Carbons Conference, Singapore, May. 19-23,(2013).
 10. M. Niibe, T. Kotaka, R. Kawakami, Y. Nakano, T. Mukai, "Damage Analysis of N₂ Plasma-etched n-GaNcrystal", 6th International Symposium on Advanced Plasma Science and its Applications for Nitrides and, Nanomaterials, Nagoya, Japan., Mar. 2-6,(2014).
 11. Masahito Niibe, Takuya Kotaka, Satoshi Jinguji, Shozo Inoue., "Evaluation of BN Thin Film Deposited on Cemented Carbide using Soft X-ray Absorption Spectroscopy", 15th International Conference on Total Reflection X-ray Fluorescence Analysis and Related Methods (TXRF 2013), Sep. Osaka, Japan. Sep.23-27, (2013).
 12. M. Niibe, K. Sano, R. Kawakami, Y. Nakano, "Recovery of disordered spectra of Ti-L NEXAFS in dry-etched TiO₂ thin film by UV irradiation", 15th International Conference on Total Reflection X-ray Fluorescence Analysis and Related Methods (TXRF 2013), Osaka, Japan. Sep. 23-27, (2013).
 13. Masahito Niibe, Keiji Sano, Takuya Kotaka, Retsuo Kawakami, Kikuo Tomonaga, Yoshitaka

- Nakano, "Etching Damage and Its Recovery by Soft X-ray Irradiation Observed in Soft X-ray Absorption Spectra of TiO₂ Thin Film", 38th International conference on Vacuum Ultraviolet and X-ray Physics, Hefei, China, Jul.12-19, (2013).
14. Masahito Niibe, Takuya Kotaka, Satoshi Jinguji, Shozo Inoue, "Characterization of BN Thin Film Deposited on Cemented Carbide Using Near Edge X-ray Absorption Fine Structure Spectroscopy", 38th International conference on Vacuum Ultraviolet and X-ray Physics, Hefei, China, Jul.12-19, (2013).
 15. R. Kawakami, M. Niibe, H. Takeuchi, T. Shirahama, M. Konishi, Y. Mori, T. Yamada. K. Tominaga, "Damage characteristics of 6H-SiC surface etched using capacitively-coupled helium plasmas driven by a radio frequency power", 12th International symposium on Sputtering and Plasma Processes, Kyoto, Japan, Jul.10-12, (2013).
 16. R. Kawakami, M. Niibe, Y. Nakano, M. Konishi, T. Shirahama, K. Tominaga and T. Mukai : "Damage Characteristics of n-GaN Thin Film Surfaces Etched by Ultraviolet Light-Assisted Helium Plasmas", The 4th International Symposium on Organic and Inorganic Electronic Materials and Related Nanotechnologies (EM-NANO2010), Kanazawa, Jun, (2013).
 17. Y.Nakano, M.Niibe, M.Lozac'h, L.Sang, M.Sumiya,"Electrical Investigation of p-i-n Junction Based on Thick i-InGaN Film", 4th International Symposium on Organic and Inorganic Electronic Materials and Related Nanotechnologies , Kanazawa, Jun. (2013).
 18. Y.Nakano, M.Niibe, M.Lozac'h, L.Sang, M.Sumiya,"Electrical Characterization of Thick InGaN Films with Various In Contents for Photovoltaic Applications", 4th International Symposium on Organic and Inorganic Electronic Materials and Related Nanotechnologies Kanazawa, Jun, (2013).
 19. R. Kawakami, M. Konishi, Y. Mori, T. Shirahama, T. Yamada, K. Tominaga, M. Niibe, Y. Nakano, T. Mukai, "Damage Characteristics of n-GaN Thin Film Surfaces Etched by N₂ Plasmas" , *The 40th International Symposium on Compound Semiconductors*, Kobe, May (2013).

20. R. Takahashi, T. Fukuoka, Y. Utsumi, "Microfluidic Devices with Three-dimensional Gold Nanostructure for Surface Enhanced Raman Scattering", IEEE International Conference on Nano/Micro Engineered and Molecular Systems (IEEE-NEMS), pp722-725, Suzhou, China, Apr. 7-10, (2013).
21. Hideki Kido, Ikuo Okada, Yuichi Utsumi, Hajime Mita, "Fabrication of PTFE micro fluidic chip for amino acid derivatization process", International Conference on Electronics Packaging (ICEP2013) , pp881-884, Osaka, Japan , Apr. 10-12, (2013).
22. M. Ishizawa, H. Nose, Y. Ukita, and Y. Utsumi, "Proposal of a Novel Internally-Triggered Automatic Flow Sequencing on Centrifugal Microfluidics", International Conference on Electronics Packaging (ICEP2013) , Osaka, Japan. pp.890-893, Apr. 10-12, (2013).
23. R. Takahashi, T. Fukuoka, Y. Utsumi, A. Yamaguchi, "Microfluidic Devices with SERS Active Three-dimensional Gold Nanostructure", International Conference on Electronics Packaging (ICEP2013) , pp.885-888, Osaka, Japan. Apr. 10-12, (2013).
24. R. Hara, R. Takahashi, T. Fukuoka, A. Yamaguchi, Y. Utsumi, "Three-dimensional Silver Nanostructure for Surface Enhanced Raman Scattering", International Conference on Electronics Packaging (ICEP2013) , pp.885-888, Osaka, Japan Apr. 10-12, (2013).
25. Yamaguchi, K. Motoi, H. Miyajima and Y. Utsumi, "Broadband noise spectroscopy of a nano-scale magnetic wire", 10th International Workshop on High Aspect Ratio Micro and Nano System Technology (HARMST2013), Apr.21-24, (2013).
26. M. Kishihara, H. Ikeuchi, H. Kido, Y. Utsumi, A. Yamaguchi, and I. Ohta, "Trial Fabrication of 180 GHz Waveguide by SR Direct Etching of PTFE", 10th International Workshop on High Aspect Ratio Micro and Nano System Technology (HARMST2013), pp.114-115, Apr. 21-24, (2013).
27. Yasuto Arisue, Yuya Matsui, Tsunemasa Saiki, Kazusuke Maenaka, Akinobu Yamaguchi and Yuichi Utsumi, "Powder Transport Direction Control Method by Using Drive Frequency of Surface Acoustic Wave", Proc. of 10th International Workshop on High Aspect Ratio Micro

- Structure Technology (HARMST2013), pp.143-144, Berlin, Germany , Apr. 21-24, (2013).
28. H. Kido, I. Okada, H. Mita, A. Yamaguchi, Y. Utsumi, “Fabrication of amino acid analysis chip using SR direct dry etching of PTFE”, 10th International Workshop on High Aspect Ratio Micro Structure Technology (HARMST2013), pp.58-59, Berlin, Germany, Apr.21-24, (2013).
 29. Y. Kang, R. Takahashi, T. Fukuoka, Y. Utsumi, Y. Haruyama, S. Matsui, “Fabrication of gold nanoparticles pattern using imprinted HSQ pattern for SERS measurement”, 10th International Workshop on High Aspect Ratio Micro Structure Technology (HARMST2013), pp.260-261, Berlin, Germany, Apr. 21-24, (2013).
 30. R. Takahashi, T. Fukuoka, Y. Utsumi, A. Yamaguchi, “Optimization of Surface Enhanced Raman Scattering Active Three- Dimensional Gold Nanostructure”, 10th International Workshop on High Aspect Ratio Micro Structure Technology (HARMST2013), pp.152-153, , Berlin, Germany, Apr.21-24, (2013).
 31. T. Yamane, S. Maekawa, I. Okada, Y. Utsumi, A. Yamaguchi, “Micro-Mirror Array Device for Floating image manufactured by Synchrotron radiation”, 10th International Workshop on High Aspect Ratio Micro Structure Technology (HARMST2013), pp.227-228, Berlin, Germany, Apr.21-24, (2013).
 32. R. Hara, R. Takahashi, T. Fukuoka, A. Yamaguchi, Y. Utsumi, “Fabrication of SARS Active Three-dimensional Silver Nanostructure”, 10th International Workshop on High Aspect Ratio Micro and Nano System Technology, pp.146-147, Berlin, Germany, Apr. 21-24, (2013).
 33. T. Kunisada, H. Nose, M. Ishizawa, K. Kuroda, I. Okada, A. Yamaguchi and Y. Utsumi, “Blood separation chip for automated biological analysis”, 10th International Workshop on High Aspect Ratio Micro and Nano System Technology, pp.194-195, Berlin, Germany, Apr.21-24, (2013).
 34. T. Yamamoto, Y. Yoritama, T. Uchiyama, Y. Utsumi, A. Yamaguchi, “Fabrication and characterization of three-dimensional type micro magneto-impedance sensor”, 10th International Workshop on High Aspect Ratio Micro and Nano System Technology, pp.225-226,

Berlin, Germany, Apr.21-24, (2013).

35. A.Yamaguchi and H. Miyajima, "Detection and stochastic analysis of magnetization fluctuation in a nano-scale magnetic wire", 8th International Symposium on Metallic Multilayers (MML2013), Kyoto, May 19-24, (2013).
36. T Yamamoto, Y. Yoritama, T. Uchiyama, Y. Utsumi, A. Yamaguchi, "Estimation of magnetic impedance of a thin Fe₁₉Ni₈₁ wire using built up micro-scale pickup coil", 8th International Symposium on Metallic Multilayers (MML2013), pp.288-289, Kyoto, May 19-24, (2013).
37. T. Kobayashi, S. Kamikawa, Y. Itou, H. Kanematsu and Y. Utsumi, International Conference on Applied Mechanics, Materials, and Manufacturing (AMMM), Hong Kong, August 17-18, (2013).
38. R. Takahashi, R. Hara, T. Fukuoka, Y. Utsumi, A. Yamaguchi, "Microfluidic Devices with SERS Active Self-assembled Gold Nanostructures", RSC Tokyo International Conference, A222, Makuhari, Chiba, Sep.5-6, (2013).
39. T. Kobayashi, T. Yokoyama, Y. Utsumi, H. Kanematsu and T. Masuda, "Measuring the Ductility of Organic Semiconductor Materials", 19th International Vacuum Congress (IVC-19), Paris, France, Sep. 9-13, (2013).
40. T. Saiki, Y. Arisue, Y. Matsui, K. Kasai, A. Yamaguchi, M. Takeo, K. Maenakab, Y. Utsumi, "Design of Surface Acoustic Wave Actuator using Bragg Reflection for Powder Transport", Proc. of 39th International Conference on Micro and Nano Engineering (MNE2013), pp.172-173, London, UK, Sep.6-19, (2013).
41. M. Takeo, S. Nii, D. Kato, S. Negoro, S. Yusa, T. Saiki, Y. Takizawa, Y. Utsumi, "Development of a Portable Fluidic and Detection System for ELISA in a 3-Dimensional Microreactor", Proc. of 39th International Conference on Micro and Nano Engineering (MNE2013), pp.178-179, London, UK, Sep.6-19. (2013).
42. T. Kobayashi, I. Hashimoto, R. Hashimoto, T. Takashina, H. Kanematsu and Y. Utsumi,

- “Comparison of Heat Transfer Performance among Solid, Hollow and Sodium Encapsulated Engine Valves”, The Irago Conference 2013, Tahara, Aichi, Japan, Oct. 24-25, (2013).
43. T. Kobayashi, Y. Sakate, R. Hashimoto, T. Takashina, H. Kanematsu, and Y. Utsumi, “Research on Optimization of Cooling Structure of LED Element (The 2nd Report)”, The Irago Conference 2013, Tahara, Aichi, Japan. Oct. 24-25,(2013).
 44. T. Kobayashi, J. Okamoto, Y. Utsumi, H. Kanematsu and T. Masuda, “Measuring the Deformation characteristics of The Films for Flexible Organic Light Emission Diode”, The Irago Conference 2013, Tahara, Aichi, Japan. Oct. 24-25, (2013).
 45. T. Kobayashi, S. Ishikawa, R. Hashimoto, T. Takashina, H. Kanematsu, K. Mizuta and Y. Utsumi, “ Optimizing Structure of LED Light Bulb for Heat Transfer (Part 2)”, The Irago Conference 2013, Tahara, Aichi, Japan. Oct. 24-25, (2013).
 46. T. Kobayashi, M. Kameyama, Y. Yabunaka, R. Hashimoto, T. Takashina, H. Kanematsu and Y. Utsumi, “Creation of a Taguchi Method Education System using Simulation of Golf Ball Trajectory”, The Irago Conference 2013, Tahara, Aichi, Japan. Oct. 24-25, (2013).
 47. T. Kobayashi, T. Yokoyama, Y. Utsumi, H. Kanematsu, T. Masuda and M. Yamamoto, “Improvement of ductility of Organic Semiconductor Materials for Flexible Organic Light Emitting Diode” 8th International Symposium on Advanced Science and Technology in Experimental Mechanics (8th ISEM '13-Sendai), Sendai, Japan, Nov. 3-6, (2013).
 48. T. Kobayashi, H. Ikeda, Y. Utsumi, H. Kanematsu, T. Masuda and M. Yamamoto, “Measurement of Reduced Elastic Modulus of Organic Semiconductor Materials for Flexible Organic Light Emitting Diode”, 8th International Symposium on Advanced Science and Technology in Experimental Mechanics, Sendai, Japan, Nov. 3-6, (2013).
 49. Y. Arisue, T. Saiki, A. Ymaguchi, and Y. Utsumi, “Study on Reflected Surface Acoustic Wave Actuator for Powders using a Grating Reflector”, Proc. of 2013 International Microprocesses and Nanotechnology Conference (MNC2013), 8P-11-88, Sapporo, Japan, Nov.5-8, (2013).

50. M. Ishizawa, T. Kunisada, K. Kuroda, C. Kataoka, A. Yamaguchi and Y. Utsumi, "Centrifugal Microfluidic Chip for Blood Separation", Proc. of 2013 International Microprocesses and Nanotechnology Conference (MNC2013), 7P-7-107, Sapporo, Japan, Nov. 5-8, (2013).
51. R. Takahashi, T. Fukuoka, Y. Utsumi, A. Yamaguchi, "Optimization of SERS Active Three-Dimensional Gold Nanostructure with High Sensitivity", Proc. of 2013 International Microprocesses and Nanotechnology Conference (MNC2013), 7D-6-2, Sapporo, Japan, Nov. 5-8, (2013).
52. T. Kobayashi, M. Fukushima, H. Kanematsu, Y. Utsumi and Y. Shimamoto, "Design and Prototyping of a Fuel Cell Controlling Equipment for Small Hybrid driving Airship System", International Conference on Control Engineering (ICCE 2014), Singapore, Feb. 9-10, (2014).
53. M. Ishizawa, Y. Arisue, I. Okada, A. Yamaguchi, and Y. Utsumi, "Novel Pressure-Controlling Valve of Centrifugal Microfluidics", PITTCON2014, pp.560-21P, Chicago, USA, Mar.2-6, (2014).
54. Yasuto Arisue, Masaki Ishizawa, Akinobu Yamaguchi, Yuichi Utsumi, "Proposal of a Lab-on-a-CD for immunoassay using nonmechanical pump and valves", PITTCON2014, pp.820-9P, Chicago, USA, Mar.2-6, (2014).
55. T. Yamane, S. Maekawa, T. Fukuoka, I. Okada, Y. Utsumi, A. Yamaguchi, "Micro-Mirror Array Device for Floating image manufactured by Synchrotron radiation", PITTCON2014, pp.1120-11P, Chicago, USA, Mar.2-6, (2014).
56. Takao Fukuoka, Ryo Takahashi, Yuichi Utsumi, Akinobu Yamaguchi, "SERS Active Three Dimensional Gold Nanostructure", PITTCON2014, pp.2380-1, Chicago, USA, Mar.2-6, (2014).
57. Takao Fukuoka, Ryo Takahashi, Yuichi Utsumi, Akinobu Yamaguchi, "Optofluidic Device with SERS Active Three Dimensional Gold Nanostructure", PITTCON2014, pp.1430-3P, Chicago, USA, Mar.2-6, (2014).
58. Takeo Watanabe, "UVL Activities in Japan", 2013 International Workshop on EUV

Lithography, Maui, Hawaii, USA, Jun. 10 – 14, (2013).

59. Takeo Watanabe, Tetsuo Harada, and Hiroo Kinoshita, “Recent Activities of the Actinic Mask Inspection using the EUV Microscope at Center for EUVL”, 2013 International Workshop on EUV Lithography, Maui, Hawaii, USA, Jun. 10 – 14, (2013).
60. Takeo Watanabe, Tetsuo Harada, and Hiroo Kinoshita, “Recent Activities of the EUV Resist Research and Development at Center for EUVL”, 2013 International Workshop on EUV Lithography, Maui, Hawaii, USA, Jun. 10 – 14, (2013).
61. Takeo Watanabe, Kazuya Emura, Daiji Shiono, Yuichi Haruyama, Yasuji Muramatsu, Katsumi Ohmori, Kazufumi Sato, Tetsuo Harada, and Hiroo Kinoshita, “EUV Resist Chemical Reaction Analysis using SR”, The 30th International Conference of Photopolymer Science and Technology, Chiba, Japan, Jun. 25 – 28, (2013).
62. Isamu Takagi, Toshiya Takahashi, Kazuhiro Katayama, Norihiko Sugie, Yukiko Kikuchi, Eishi Shiobara, Hiroyuki Tanaka, Soichi Inoue, Takeo Watanabe, Tetsuo Harada, and Hiroo Kinoshita, “Comparison of Resist Family Outgassing Characterization”, The 30th International Conference of Photopolymer Science and Technology, Chiba, Japan, Jun. 25 – 28, (2013).
63. Takeo Watanabe, “Development of the EUV Resist at Center for EUVL”, The 3rd Sino-Japan Symposium on Information and Electronic Materials, Shanghai, China, Sep. 9, (2013).
64. Takeo Watanabe, “Development of the EUV Resist at Center for EUVL”, The 3rd Sino-Japan Symposium on Information and Electronic Materials, Beijing, China, Sep. 12, (2013).
65. Takeo Watanabe, Kazuya Emura, Daiju Shiono, Yuichi Haruyama, Yasuji Muramatsu, Katsumi Ohmori, Kazufumi Sato, Tetsuo Harada, and Hiroo Kinoshita, “Chemical Reaction Analysis by SR Absorption Spectroscopy to Increase the Acid Generation Efficiency of EUV CA Resist”,
66. 2013 International Symposium on Extreme Ultraviolet Lithography, Toyama, Japan, Oct. 6 – 10, (2013).
67. Kazuhiro Katayama, Toshiya Takahashi, Norihiko Sugie, Isamu Takagi, Yukiko Kikuchi, Eishi

- Shiobara, Hiroyuki Tanaka, Soichi Inoue, Takeo Watanabe, Tetsuo Harada, and Hiroo Kinoshita, “Resist outgassing characterization of PAG-blended and PAG-bound systems”, 2013 International Symposium on Extreme Ultraviolet Lithography, Toyama, Japan, Oct. 6 – 10, (2013).
68. Yukiko Kikuchi, Toshiya Takahashi, Norihiko Sugie, Isamu Takagi, Kazuhiro Katayama, Eishi Shiobara, Hiroyuki Tanaka, Soichi Inoue, Takeo Watanabe, Tetsuo Harada, and Hiroo Kinoshita, “Study of the relation between Resist components and outgassing contamination species”, 2013 International Symposium on Extreme Ultraviolet Lithography, Toyama, Japan, Oct. 6 – 10, (2013).
69. Yusuke Tanaka, Tetsuo Harada, Takeo Watanabe, Yuichi Usui, and Hiroo Kinoshita, “ Development of Micro Coherent EUV Scatterometry Microscope for EUV Mask Defect Characterization”, 2013 International Symposium on Extreme Ultraviolet Lithography, Toyama, Japan, Oct. 6 – 10, (2013).
70. Y. Tanaka, T. Harada, T. Watanabe, Y. Usui, and H. Kinoshita, “Observation Result of Phase Defects using Micro Coherent EUV Scatterometry Microscope”, 25th Microprocesses and Nanotechnology Conference, Sapporo, Hokkaido, Japan, Nov. 5 – 8, (2013).
71. Norihiko Sugie, Toshiya Takahashi, Kazuhiro Katayama, Isamu Takagi, Yukiko Kikuchi, Hiroyuki Tanaka, Eishi Shiobara, Soichi Inoue, Takeo Watanabe, Tetsuo Harada, and Hiroo Kinoshita, “Resist outgassing characterization based on the resist compositions and process”, SPIE Advanced Lithography 2013, San Jose, California, USA, Feb. 23 – 27, (2013).
72. S. Matsubara, H. Kudo, T. Watanabe, K. Emura, and H. Kinoshita “Novel EUV Resist Materials based on Noria (Water-wheel Like Cyclic Oligomer) Derivatives with Pendant Ethoxy and Adamantyl Ester Groups”, 25th Microprocesses and Nanotechnology Conference, Sapporo, Hokkaido, Japan, Nov. 5 -8, (2013).
73. K. Emura, T. Watanabe, M. Yamaguchi, H. Tanino, T. Fukui, D. Shiono, Y. Haruyama, Y. Muramatsu, K. Ohmori, K. Sato, T. Harada, and H. Kinoshita, “Chemical Reaction Analysis of PHS CA Resist System for EUVL using Soft X-ray Absorption Spectroscopy”, 25th

Microprocesses and Nanotechnology Conference, Sapporo, Hokkaido, Japan, Nov. 5-8, (2013).

74. Tsuneo Terasawa, Tsuyoshi Amano, Takeshi Yamane, Hidehiro Watanabe, Mitsunori Toyoda, Tohoku, Tetsuo Harada, Takeo Watanabe, and Hiroo Kinoshita, "At wavelength observation of phase defect embedded in EUV mask using microscope "technique", SPIE Advanced Lithography 2014, San Jose, California, USA, Feb. 23-27, (2014).
75. Tsuyoshi Amano, Tsuneo Terasawa, Hidehiro Watanabe, Mitsunori Toyoda, Tetsuo Harada, Takeo Watanabe, and Hiroo Kinoshita, "Observation of phase defect on extreme ultraviolet mask using an extreme ultraviolet microscope", SPIE Advanced Lithography 2014, San Jose, California, USA, Feb. 23-27, (2014).
76. Yukiko Kikuchi, Kazuhiro Katayama, Isamu Takagi, Norihiko Sugie, Toshiya Takahashi, Hiroyuki Tanaka, Eishi Shiobara, and Soichi Inoue, Takeo Watanabe, Tetsuo Harada, and Hiroo Kinoshita, "Correlation study on resist outgassing by EUV irradiation tool and E-beam irradiation tool", SPIE Advanced Lithography 2014, San Jose, California, USA, Feb. 23-27, (2014).
77. Tetsuo Harada, Yusuke Tanaka, Tsuyoshi Amano, Youichi Usui, Takeo Watanabe, and Hiroo Kinoshita, "At wavelength observation of phase defects using focused lensless microscope", SPIE Advanced Lithography 2014, San Jose, California, USA, Feb. 23-27, (2014).
78. S. Ono, T. Hatsui, M. Omodani, T. Kudo, K. Kobayashi, N. Teranishi, T. Watanabe, T. Imamura, T. Ohmoto, and A. Iwata, "Noise Analysis of a Silicon-on-Insulator (SOI) Pixel Sensor with 500 μm Thick High Resistivity Silicon for X-Ray Free-Electron Laser Experiments", IEEE NSS/MIS, NP01-11, Seoul, South Korea, November, (2013).
79. M. Okada, Y. Haruyama, S. Matsui, "Abrasion Test for Antisticking Layer by Scanning Probe Microscopy", 57th International Conference on electron, ion, photon beam technology and fabrication, (EIPBN 2013), Nashville, USA, May.29, (2013).
80. T. Oyama, M. Okada, S. Iyoshi, Y. Haruyama, S. Matsui, H. Miyake, T. Mizuta, "Evaluation of fluorine additive segregation in UV nanoimprint resin by X-ray photoelectron spectroscopy",

57th International Conference on electron, ion, photon beam technology and fabrication, (EIPBN 2013), Nashville, USA, May.29, (2013).

81. H. Wakaba, M. Okada, S. Iyoshi, Y. Haruyama, S. Matsui, “Selective Patterning of Fluorinated Self-assembled Monolayer by UV Nanoimprinting for Directed Self-Assembly”, 57th International Conference on electron, ion, photon beam technology and fabrication, (EIPBN 2013), Nashville, USA, May.29, (2013).
82. M. Okada, E. Nishioka, M. Kondo, Y. Haruyama, T. Sasaki, N. Kawatsuki, S. Matsui, H. Ono, “Reorientation Evaluation of Photoinduced Liquid Crystalline Polymer Pattern Fabricated by Hybrid Nanoimprinting with Linearly Polarized Ultra Violet Irradiation”, 57th International Conference on electron, ion, photon beam technology and fabrication, (EIPBN 2013), Nashville, USA, May.29, (2013).
83. S. Iyoshi, M. Okada, Y. Haruyama, S. Matsui, K. Kobayashi, S. Kaneko, M. Nakagawa, H. Hiroshima, “Effects of Fluorosurfactants on Antisticking Layer Resistance in Repeated UV Nanoimprint”, 57th International Conference on electron, ion, photon beam technology and fabrication, (EIPBN 2013), Nashville, USA, May.30,.(2013).
84. M. Okada, E. Nishioka, M. Kondo, Y. Haruyama, T. Sasaki, H. Ono, N. Kawatsuki and S. Matsui, “Comparison Molecular Orientation of Photoinduced Liquid Crystalline Polymer induced by Grapho epitaxy to that by Thermal Nanoimprinting”, 30th International Conference of Photopolymer Science and Technology (ICPST-30), Chiba, Japan, Jun.27, (2013)
85. M. Okada, E. Nishioka, M. Kondo, Y. Haruyama, T. Sasaki, H. Ono, N. Kawatsuki and S. Matsui, “Molecular Orientation of 3D-photoinduced Liquid Crystalline Polymer Structure fabricated by Thermal Nanoimprinting”, 30th International Conference of Photopolymer Science and Technology (ICPST-30), Chiba, Japan, Jun.27, (2013).
86. T. Oyama, M. Okada, S. Iyoshi, Y. Haruyama, H. Miyake, T. Mizuta and S. Matsui, “Surface Evaluation of Cationic UV-curable Resin with Fluorine Additive by XPS”, 30th International Conference of Photopolymer Science and Technology (ICPST-30), Chiba, Japan, Jun.27, (2013).

87. H. Wakaba, M. Okada, S. Iyoshi, Y. Haruyama and S. Matsui, "Release Property Evaluation of Fluorinated Antisticking Layer by a Mixture of Release Agents", 30th International Conference of Photopolymer Science and Technology (ICPST-30), Chiba, Japan, Jun.27, (2013).
88. T. Watanabe, K. Emura, D. Shiono, Y. Haruyama, Y. Muramatsu, K. Ohmori, K. Sato, T. Harada and H. Kinoshita, "EUV Resist Chemical Reaction Analysis using SR", 30th International Conference of Photopolymer Science and Technology (ICPST-30), Chiba, Japan, Jun.27, (2013).
89. N. Kawatsuki, Y. Inada, K. Goto, M. Kondo, Y. Haruyama, and S. Matsui, "NEXAFS Study on Photoalignment of Liquid Crystalline Polymeric Films", 17th International Symposium on Advanced Display Materials and Devices (ADMD2013), Shanghai, China, Jun.28, (2013)
90. Y. Haruyama, M. Okada, E. Nishioka, M. Kondo, N. Kawatsuki, and S. Matsui, "NEXAFS studies of photoreactive liquid crystalline polymer", 8th International conference on Vacuum Ultraviolet and X-ray Physics (VUVX-38), Hefei, China, Jul.15, (2013).
91. M. Okada, R. Hosoda, M. Kondo, Y. Haruyama, T. Sasaki, H. Ono, N. Kawatsuki, and S. Matsui, "Enhanced molecular orientation of photoreactive liquid crystalline polymer induced by thermal nanoimprinting compared to graphoepitaxy", 39th International Conference on Micro and Nano Engineering (MNE2013), London, United Kingdom, Sep.19, (2013)
92. M. Okada, R. Hosoda, M. Kondo, Y. Haruyama, T. Sasaki, H. Ono, N. Kawatsuki, and S. Matsui, "Molecular Orientation of Photoreactive Liquid Crystalline Polymer Induced by Nanoimprint-graphoepitaxy", 12th International Conference on Nanoimprint and Nanoprint Technology (NNT2013), Barcelona, Spain, Oct.22, (2013).
93. K. Emura, T. Watanabe, M. Yamaguchi, H. Tanino, T. Fukui, D. Shiono, Y. Haruyama, Y. Muramatsu, K. Ohmori, K. Sato, T. Harada and H. Kinoshita, "Chemical Reaction Analysis of PHS CA Resist System for EUVL using Soft X-ray Absorption Spectroscopy", 26th International Microprocesses and Nanotechnology Conference (MNC 2013), Sapporo, Japan, Nov.17, (2013).

94. S. Iyoshi, M. Okada, K. Kobayashi, S. Kaneko, T. Katase, K. Tone, Y. Haruyama, M. Nakagawa, H. Hiroshima and S. Matsui, "Study of the Resistance of Antisticking Layer on Repeated UV Nanoimprint", 26th International Microprocesses and Nanotechnology Conference (MNC 2013), Sapporo, Japan, Nov.17, (2013).
95. N. Sugano, M. Okada, Y. Haruyama and S. Matsui, "HSQ Replica Mold with Release Property fabricated by Room Temperature Nanoimprinting", 26th International Microprocesses and Nanotechnology Conference (MNC 2013), Sapporo, Japan, Nov.17, (2013).
96. T. Oyama, M. Okada, S. Iyoshi, Y. Haruyama, H. Miyake, T. Mizuta and S. Matsui, "XPS Analyses of Ultrathin UV Nanoimprint Resin added with Fluorine Additive", 26th International Microprocesses and Nanotechnology Conference (MNC 2013), Sapporo, Japan, Nov.17, (2013).
97. M. Okada, Y. Haruyama and S. Matsui, "Evaluation of Abrasion Resistance for Antisticking Layer by Scanning Probe Microscopy", 26th International Microprocesses and Nanotechnology Conference (MNC 2013), Sapporo, Japan, Nov.8, (2013).
98. M. Okada, R. Hosoda, M. Kondo, Y. Haruyama, T. Sasaki, H. Ono, N. Kawatsuki and S. Matsui, "Material Dependency of Molecular Orientation in Liquid Crystalline Polymer induced by Nanoimprint-graphoepitaxy", 26th International Microprocesses and Nanotechnology Conference (MNC 2013), Sapporo, Japan, Nov.8, (2013).

Academic Degrees

Academic Degrees

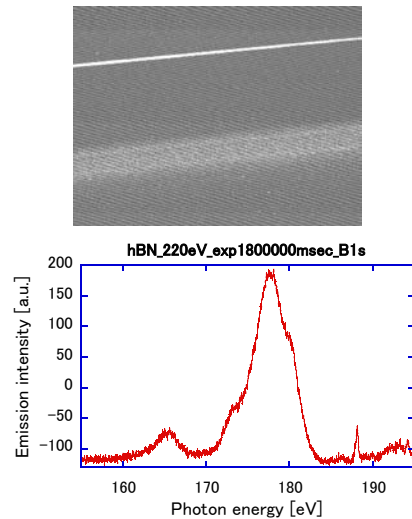
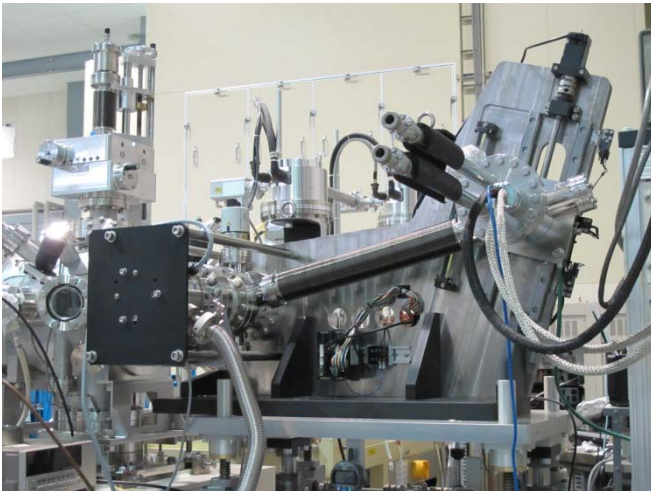
Degree	Name	Master's Thesis
Master of Engineering	Yasuto ARISUE (University of Hyogo)	<i>Study of High Accurate Chemical Unit Operation for Immunoassay using Lab-on-a-CD</i>
Master of Engineering	Masaki ISHIZAWA (University of Hyogo)	<i>Improvement of Sensitivity of Immunoassay Reaction for Diagnostics using Lab-on-a-CD</i>
Master of Science	Hideki KIDO (University of Hyogo)	<i>Investigation on derivatization procedure using a Lab-on-a-chip made of PTFE microstructure</i>
Master of Science	Ryo TAKAHASHI (University of Hyogo)	<i>Study on nanoplasmonic structure for Surface Enhanced Raman Scattering detection in a microfluidic device</i>
Master Of Engineering	Daichi TSUJIKAWA (University of Hyogo)	<i>Development of the EUV Light Scattering Measurement Method</i>

Degree	Name	Doctor's Thesis
Doctor of Engineering	Tsuyoshi AMANO (Dai Nippon Printing Co., Ltd.)	<i>Studies of EUVL Mask Pattern Defect Inspection and Structure Analysis of Phase Defects</i>
Doctor of Science	Yuji KANG (University of Hyogo)	<i>Room-Temperature Nanoimprinting using Hydrogen Silsesquioxane and Its Applications</i>
Doctor of Engineering	Katsuhiko MURAKAMI (Nikon Co., Ltd.)	<i>Development of Soft X-ray Projection Optics using Multilayer Mirrors and Application Usage for EUV Exposure Tool</i>

Cover photograph

Soft X-ray Emission Spectrometer at BL-09A

High performance flat-field type spectrometer was constructed for soft X-ray emission spectroscopy (SXES) at the long undulator beamline BL-09A. The spectrometer was designed for high detection efficiency and high energy resolution in the energy range of 50 – 600 eV. The energy resolution was estimated to be greater than 1000 ($E/\Delta E$). A distortion of the linear profile of the focus image on the CCD detector was successfully removed by using a spherical VLS grating. The spectrometer will be used for evaluations of lithium-ion battery, various compound semiconductors, and various light-element-containing materials.



LASTI Annual Report 2013 Vol.15(2013)

2014.8 Published by

Laboratory of Advanced Science and Technology for Industry, University of Hyogo
3-1-2 Kouto, Kamigori-cho, Ako-gun, Hyogo, 678-1205 JAPAN
TEL: +81-791-58-0249 / FAX: +81-791-58-0242

Editorial board

Editor in Chief	Shinji Matsui
Editors	Kazuhiro Kanda
	Yoshihiko Shoji
	Masahito Niibe
	Yuichi Utsumi
	Takeo Watanabe